MULTIWALLED CARBON NANOTUBE FILMS: FABRICATION TECHNIQUES AND APPLICATIONS

By

John Lucien Rigueur

Dissertation

Submitted to the Faculty of the

Graduate School of Vanderbilt University

in partial fulfillment of the requirements

for the degree of

DOCTOR OF PHILOSOPHY

In

Interdisciplinary Materials Science

May, 2012

Nashville, TN

Approved:

Professor Arnold Burger

Professor David Ernst

Professor Stephanie Getty

Professor Timothy Hanusa

Professor Charles Lukehart

Professor Norman Tolk

ABSTRACT

The first part of the dissertation focuses on randomly oriented freestanding films of multi-walled carbon nanotubes (MWCNTs), also known as buckypapers, which have been fabricated by a two-step process using electrophoretic deposition (EPD). These multi-walled carbon nanotubes films were cast onto stainless steel electrodes from aqueous suspensions by EPD. Using a facile mechanical cleavage technique, the films were liberated from their underlying electrodes to yield the buckypapers. We investigated the films' thickness, morphology, and surface topology using, respectively, profilometry, scanning electron microscopy, and atomic force microscopy. Mechanical characterization of the buckypapers revealed the average tensile strength and Young's modulus to be 14.5 MPa and 3.3 GPa, respectively.

The second part of this dissertation focuses on vertically aligned multi-walled carbon nanotubes. The purpose of our investigation was to optimize the growth of catalyst assisted chemical vapor deposition (CVD) grown carbon nanotubes for use as a photon absorbers in mid- to far-infrared applications. Improvement of the height and density of the carbon nanotubes will effectively increase the films absorptivity, bringing this material closer to an ideal absorber. NASA is currently exploring the use of this technology towards improving the stray light suppression of space flight instruments for future earth and space science missions. Detrimental to these scientific instruments is the stray light that scatters on interior telescope and instrument surfaces, thereby reducing the

performance of observational instruments. In order to control this undesired effect, low-reflectance surface treatments are implemented in structural instrument designs. Z306 black paint is traditionally used to absorb stray photons, but advanced absorbers that employ films of multi-walled carbon nanotubes have been shown to provide an order of magnitude improvement over current surface treatments in the UV-visible-near infrared wavelengths. To this end, we varied the thickness of the iron catalyst layer and deposition conditions; varied hydrogen exposure times of substrates to optimize the MWCNT length and film density for efficient absorption of longer wavelength photons. Scanning electron microscopy is used to characterize film density and MWCNT height, and hemispherical reflectance measurements are used to quantify performance of the absorptive films.

Dedicated

to

My grandmothers Pearl Christina Pacheco and Yvonne Cruishank, whom I lost during this PhD. Journey, my mother Joan R Eastmond, and my aunt Janet Eastmond, for their encouragement, support and belief in me to pursue my graduate studies.

AKNOWLEDGEMENTS

First and foremost I give thanks to GOD. Science to me is the pursuit of conveying the message of GOD and with faith many aspirations are possible, we must believe. I am an avid believer that we are given trials in life in order to transcend beyond our innate being. From our experiences which may seem as exams at times we arise anew like the mythological bird the phoenix. Where some see chance or luck, I have come to view it as divine intervention unfolding due to a faith the size of a mustard seed. Finding such a small seed within ourselves requires devotion. For when faith intervenes, we must practice humility and give thanks because every interaction we have is a greater piece to the puzzle of our lives, our finite time here. And by these interactions we are brought closer to a curious power within in us all. It is a marvelous wonder and thus one can refer to this dissertation as “The Curious Case of John Lucien Rigueur.”

For this reason I am grateful to the following individuals for aiding in my dissertation. My advisor Professor Arnold Burger who has provided the necessary support both professionally and personally allowing me to complete a task not for me but for my Grandmother Pearl Pacheco whom I was fortunate to visit in our home land of Trinidad and Tobago before she passed, I had never experienced loss until this event. She birthed the curiosity in me, gave me an unfounded confidence in my abilities, defined perseverance and has always told her friends that I was going to the stars. Now something that I have worked on

will be going to the stars. My NASA advisors Stephanie Getty PhD. and John Hagopian, in September of 2010 my life took an unusual turn and it seems as though chance or divine intervention favored me. I attended the NASA Graduate Student Symposium arriving a day late to present my research conducted at Vanderbilt University. I arrived with no intent on having meetings with anyone one at NASA and met Mrs. Mablelene Burrell who emphasized that I get a meeting with scientist at NASA. Following our conversation she got a meeting with the educational office where I was informed of those doing exciting research at NASA. It is in this meeting that I heard and wrote the name John Hagopian. Following this meeting I was assigned to meet with Chuck Powers in the Materials Directorate on my last day at the symposium. The outcome of this meeting was a phone conference with Stephanie Getty from which my time at NASA began in January 2011. I ask is this chance or divine intervention? Stephanie I am truly indebted to you for your guidance, support and willing to work with me to make me a more organized scientists. John H., I am also indebted to you and I am thankful for your guidance and support, in addition to securing additional support, though we still have to play that chess game.

I am also grateful to the members of my PhD committee Professors Timothy Hanusa my committee chair who has been with me through graduate school matriculation. Professor David Ernst, for your hard work and continual words of encouragement and honesty; Professor Norman Tolk whose hard questions and patience has pushed me to improve my scientific abilities; and Professor Charles Lukehart whom was there in a great time of need, I thank you

for being direct an honest with me I respond to this because it was how I was raised. In addition I will like to thank NASA staff members Gregory Hidrobo, Manuel Quijada, Chuck Powers, Michael Viens, Mark McClendon, Lynne Branch-Foster, Lucy McFadden and Mablelene Burrell; the VINSE staff Anthony Melo, Ben Schmidt, René Colehour and Sarah Satterwhite, the Fisk-Vanderbilt Bridge staff Alyce Dobyns, Maggie Zilbut and Consti Coca.

In graduate school we have mentors, acquire new friends and research associates which form our support group. I will like to thank my past group members, Sameer Mahajan, Dustin Kavich, Sueseela Somarajan, Melissa Harrison, Weidong Hei, Alex Krejci and Saad Hasan. Mentors are an important part of life as such, Glenford Codrington, Walter Searcy III, Dr. Eugene W. Collins, Dr. Lenard Feldman, Dr. Steve Morgan, Dr. Keivan Stassun, Dr. Princilla Evans-Morris Dr. Bruce Vaughn and Dr. Don Brunson; you were all placed in my life for a reason, thank you. My friends and support group, Jonathan Reynolds, Bryan Kent Wallace, Tam'ra Kay Francis, Dawit Johwar, Anthony Price, Bruce LeMont McMillan, Desmond Campbell, Thompson LeBlanc, Anh Hoang, Peter Ciesielskie, Joy Garnett, Ebonee Walker, Charleson Bell, Shann Yu, Nichole Renee Phillips, Hasting Hill and Jedidah Isler; for putting up with my highs and lows.

Last but not least I would like to acknowledge Fisk University, my life was changed forever considering I came without any financial support, only a dream to be a mentor and example for my three younger brothers Jeffrey Rigueur, Josue Rigueur and Jermain Rigueur and my son Jadon C Saunders-Rigueur.

Finally my gratitude to my sister Giselle Anthony your discussions brought me strength and reaffirmed my perseverance.

The research discussed in this dissertation was made possible with financial support from the National Science Foundation Integrative Graduate Education and Research Traineeship (IGERT) Fellowship for research in the Nanosciences and from the NASA Harriet G. Jenkins Pre-doctoral Fellowship Program.

I conclude with quotes from *Albert Einstein* which I live and treat the world around me by:

"Problems are best solved at a different level of consciousness from which they are created."

"The intuitive mind is a sacred gift and the rational mind is a faithful servant. We have created a society that honors the servant and has forgotten the gift."

TABLE OF CONTENTS

Page

LIST OF TABLES

LIST OF FIGURES

Figure Page

CHAPTER 1

INTRODUCTION

Carbon, one of the most abundant elements found on earth has unique properties due to its sp^n – hybridized bonds which lead to the many carbon allotropes, ranging from zero to three dimensions on the nanoscale. These allotropes of carbon (Figure 1.1), the zero- dimensional (0D) carbon buckyballs, one-dimensional (1D) carbon nanotubes, two-dimensional (2D) graphene and three-dimensional (3D) diamond, make it a highly investigated material for a wide range of nanotechnology applications [1]. On the nanoscale, materials behave differently from their bulk counterparts, due to the effects of quantum confinement; Table 1 shows the effects dimensionality has on the unique properties of the allotropes of carbon. From the perspective of materials science, these materials possess intriguing chemical, physical and electronic properties that have attracted the global community of scientists to investigate applications in advanced technological devices. Of the allotropes of carbon, carbon nanotubes (CNTs) have led the charge since their discovery in 1991 by Iijima [2].

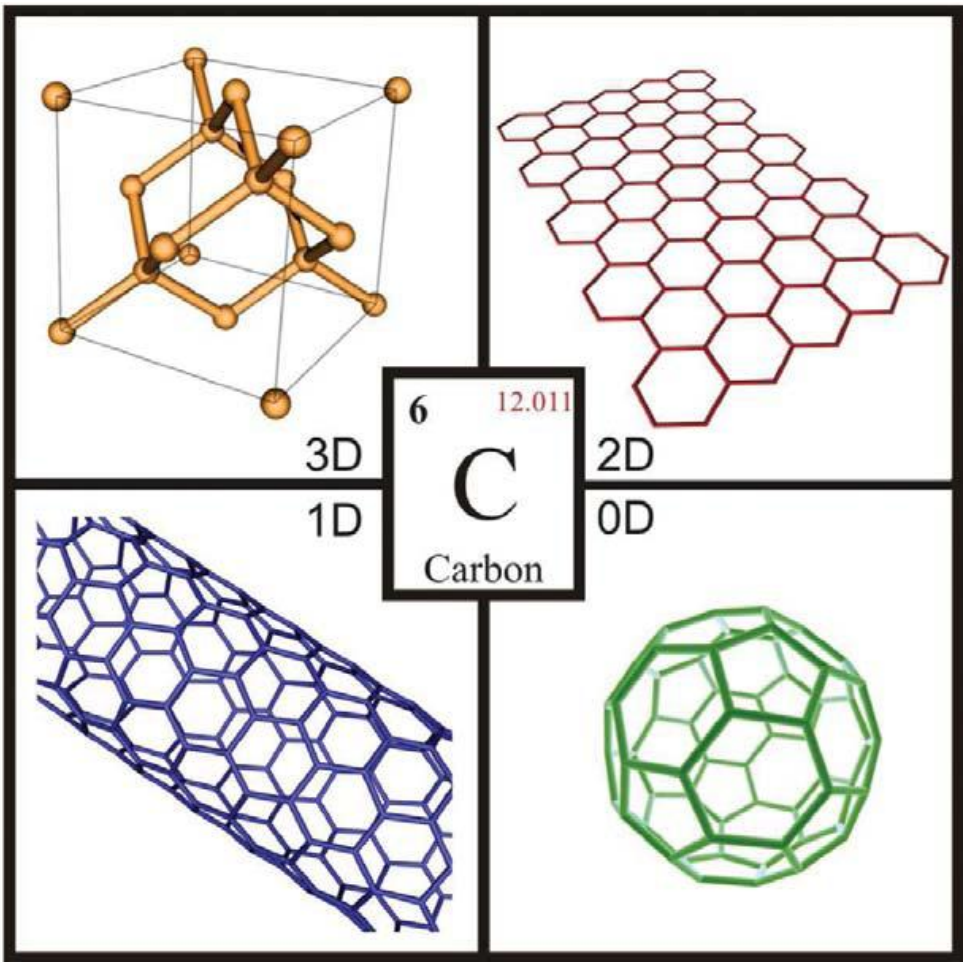

Figure 1.1.[1] Schematic diagram showing the different allotropes of carbon: the zero- dimensional (0D) carbon buckyballs, one-dimensional (1D) carbon nanotubes, two-dimensional (2D) graphene and three-dimensional (3D) diamond.

Table 1.1. Electronic properties of carbon-based materials [1]

	Electron Mobility ($cm^2 V^{-1}s^{-1}$)	Bandgap (eV)	Thermal Conductivity ($W cm^{-1} K^{-1}$)
Diamond	**2200**	**5.45**	**22**
Carbon Nanotubes	**1×10^5**	**(0 to 1)**	**30**
Graphene	**1×10^4 to 2×10^5**	**(0 to 0.5)**	**40**

Carbon nanotubes (CNTs) were discovered using the arc discharge production method. CNTs can be described as single or multiple sheets of graphene with a hexagonal ring structure, rolled into a cylindrical shape as shown in Figure 1.2. As produced, they are usually linear, exhibiting long-range order parallel to the axis of the nanotube. Nanotubes are composed of sp^2 bonded carbon, which is a factor for its unique mechanical, thermal, electronic and optical properties. There are several types of carbon nanotubes (CNTs) widespread in the scientific research; single-walled (SW), doubled-walled (DW) and multi-walled (MW), as shown in Figure 1.2 respectively.

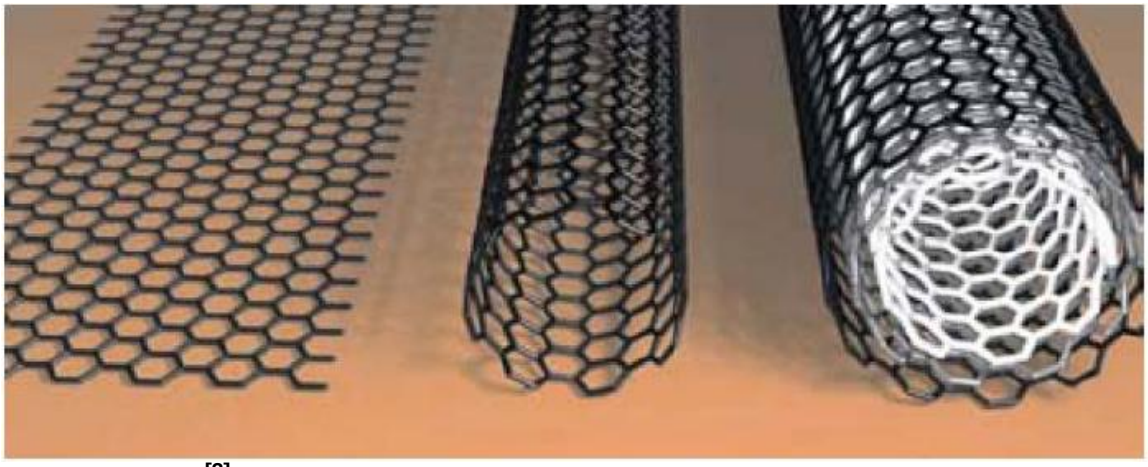

Figure 1.2.[3] Formation of single and multi-walled carbon nanotubes from graphene. The graphene sheet on the left is rolled to form a single walled nanotube (middle) and multi-walled carbon nanotube (right).

1.1. Structure of Nanotubes

Carbon nanotubes, due to their small diameter (~10 Å) and large length to diameter (aspect ratio) (>10^3), provide an important system for studying one-dimensional physics, theoretically and experimentally [4]. To understand the structure of CNTs, we investigate a sheet of 2D graphene rolled to form a 1D SWCNT and identify mathematically the alternate forms of chirality since the traditional view of a tube is a rolled up sheet of graphene. The chiral vector C_h, which spans the circumference of a CNT, is used to identify how a graphene sheet can be rolled up into cylindrical form. The chiral vector C_h is defined as;

$$C_h = n\vec{a}_1 + m\vec{a}_2 \qquad 1.1$$

where a_1 and a_2 are the unit vectors of graphite and *n* and *m* are arbitrary integers. As depicted in Figure 1.3, a (*n, m*) nanotube is formed by rolling the graphene sheet into a cylinder in order for atoms *O* and *A*, or *B* and *B'* to be connected by the chiral vector. The diameter of a single tube (tubule) can be expressed as;

$$d_t = \frac{C_h}{\pi} = \frac{\sqrt{3a_{C-C}(m^2 + mn + n)^{1/2}}}{\pi} \qquad 1.2$$

where $a_{C\text{-}C}$ is the nearest neighbor distance (1.42Å in graphite), C_h is the length of the chiral vector and the chiral angle equation is given by,

$$\theta = \tan^{-1}\left[\frac{\sqrt{3}m}{m+2n}\right] \text{ [4]} \qquad 1.3$$

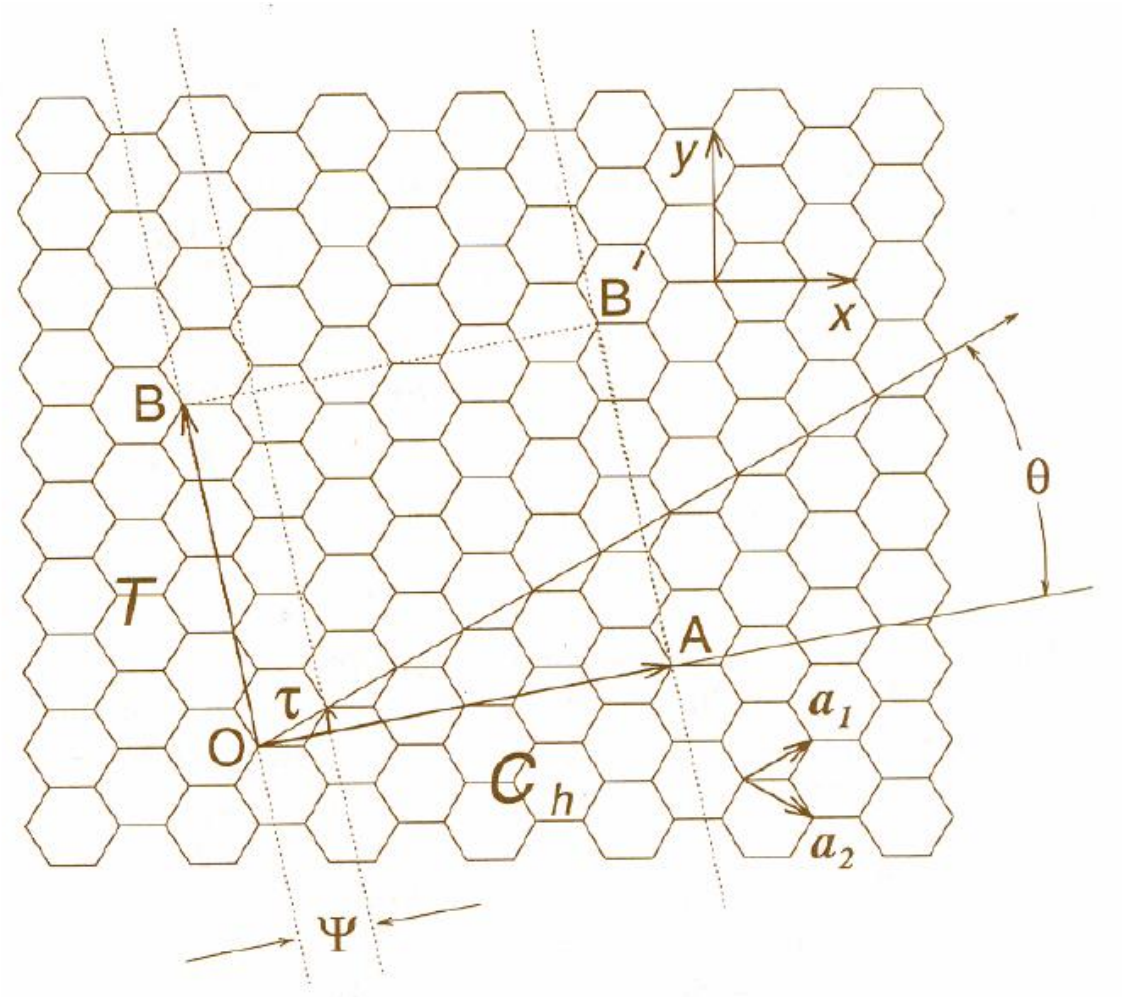

Figure 1.3.[4] Chiral vector schematic defined on the honeycomb lattice of graphene, a_1 and a_2 are unit vectors, θ is the chiral angle with respect to the zigzag axis.

The chiral vector determines the rolling direction of the graphene sheet where each carbon atom is located at the vertex of the hexagon lattice structure for which lattice point integers (*n, m*) are superimposed with an origin defined as (*0, 0*), resulting in chiral nanotubes[2, 4]. As a result of the chiral vector, where each integer pair (*n, m*) defines a singular approach of rolling the graphene sheet we form three rolling orientations (chiral, zigzag and armchair); see Figure 1.4 of a carbon nanotube[5]. The chiral angle θ and lattice vector representations of the

nanotube in the zigzag direction is θ = 0, where it has lattice vector values of (*n, 0*) and of the armchair θ= 30^o, while its lattice vector values are (*n, n*). Both the (*n, 0*) and (*n, n*) nanotubes have especially high symmetry and exhibit a mirror symmetry plane normal to the tubule axis.

The lattice constant and intertube spacing are a necessity to generate SWCNTs and MWCNTs, where these parameters vary in tube diameter or radial direction. Most experimental measurements and theoretical calculations agree that the C-C bond length $d_{CC} = 1.42\text{Å}$ and $a = |a_1| = |a_2| = 2.46\text{Å}$ and intertube spacing $d_{tt} = 3.4\text{Å}$ [6]. Since both right and left-handed chirality is possible for chiral tubules, it is expected that chiral tubules are optically active to either right or left circularly polarized light propagating along the tubule axis.

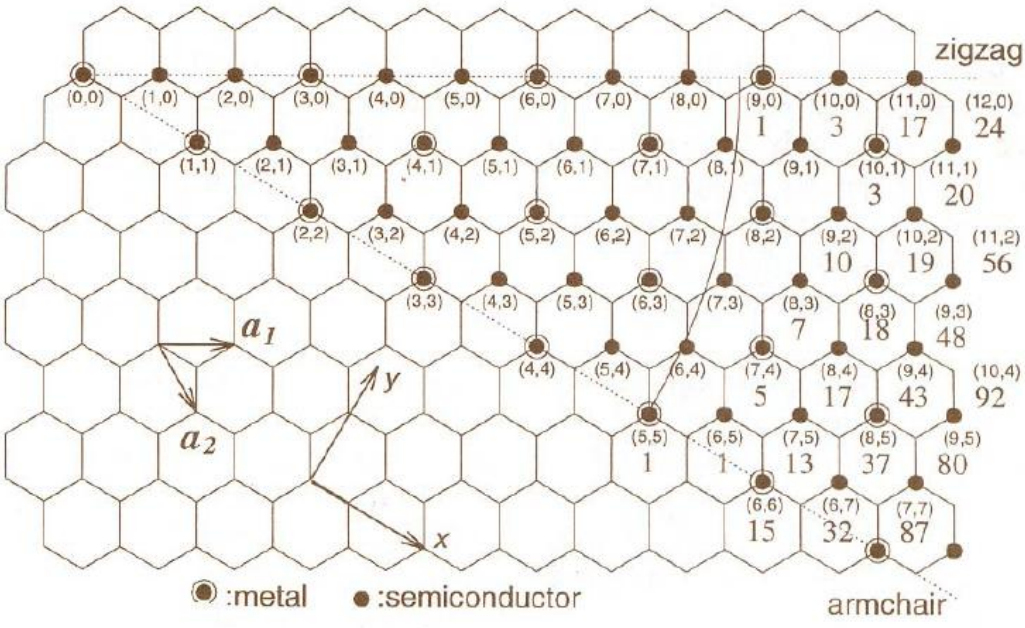

Figure 1.4.[4] Graphene sheet with unitary vectors specified by (*n,m*) integers for formation of nanotubes. Solid dots represent semiconducting tubes, encircled dots represent metallic tubes.

The fundamental translation vector given by $\vec{\mathrm{T}}(n,m)$ is located along the tube axis and is perpendicular to $\vec{C}_h$. The length of the Brillouin zone is $\frac{2\pi}{|T|}$, where $|\mathrm{T}| = a$ for an armchair nanotube and $|\mathrm{T}| = \sqrt{3}a$ for zigzag nanotubes. In general, for any (*n,m*) nanotube,

$$\mathrm{T} = \frac{\sqrt{3}}{d_R}\left|\vec{C}\right| = \frac{\sqrt{3}d_t\pi}{d_R} \qquad 1.4$$

where d_R is the greatest common divisor of (*2n+m*) and (*2m+n*).

1.2. Electronic Structure of Nanotubes

The bonding of carbon nanotubes consists of sp^2 (sp_Xp_Y) hybridized bonds which is similar to that in graphene. Figure 1.5.a shows the unit cell and basis vectors for graphene in real space, where these bonds are planar in characteristic and occur when the 2s and $2p_{XY}$-shells of each carbon atom are combined with the 2s- and $2p_{XY}$-shells of its neighboring atoms, forming bonds that have both s and p character. The bonds formed are the strong covalent or σ bonds and the weak π bond based on interaction of the p_Z orbital, allowing each carbon atom to have three σ bonds and one π bond. These sp^2 bonding characteristics may be used to approximate the bonds in cylindrical carbon nanotubes. Since perfect nanotubes encompass a uniform diameter, observation has shown defects in bonding that allow sp^3 bonding to occur. This bonding mechanism may produce defects, such as pentagons and heptagons, in the perfect hexagonal structure. Through the gradual narrowing and widening of

nanotubes these defects may be observed[7]. The tubular structure of a nanotube then can be described with a sp^2 – sp^3 bonding characteristic, to account for the defects.

In order to understand the electronic properties a zone folding tight binding method is used to map the band structure of graphene to construct the Brillouin zone (BZ) of a SWCNT. This method takes into account only confinement effects and neglects the contribution of curvature[8]. Figure 1.5.b shows the hexagonal BZ of graphene, in reciprocal space whose sides are $1/3a_{C-C}$ from the center. The BZ contains one electron per atom thus graphite is zero-gap semiconductor or semimetal (π-π* overlapping). The Fermi surface is reduced to six points at the hexagonal BZ corners where the 2D graphene electronic structure near the Fermi energy is given by occupied π (valence) band and an empty π* (conduction) band. These bands have a linear dispersion in $E(k)$ near the K point.

Based on Wallace's model [9] the energy dispersion $E(k)$ of the π and π* bands are calculated based on the nearest-neighbor tight binding model. Thus

$$E(k_X, k_Y) = \pm\gamma_0\left[1 + 4\cos\left(\frac{\sqrt{3}k_X a}{2}\right)\cos\left(\frac{k_Y a}{2}\right) + 4\cos 2\left(\frac{k_Y a}{2}\right)\right]^{1/2} \qquad 1.5$$

where γ_0 is the overlap integral between nearest-neighbor carbon atoms and the ± refer to the π* and π bands, respectively. Figure 1.6.a and b shows the 2D and 3D energy bands for graphene based on calculations from equation 1.5. We observed at the K points the vanishing of the energy gap where the Fermi energy, E_F, is $E_F = 0$; consequently these K points are important for electric

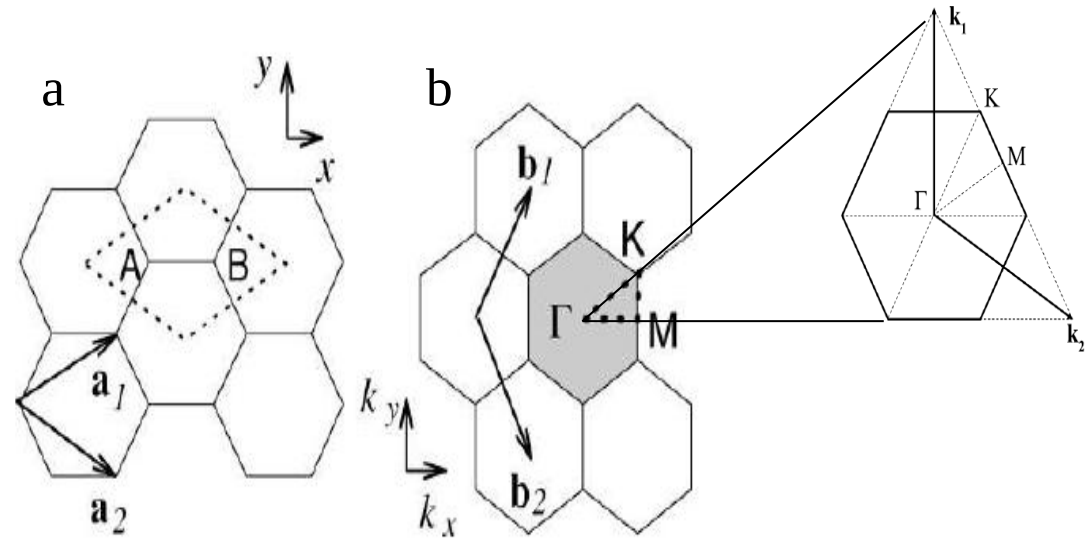

Figure 1.5.[8] (a)The unit cell of graphene in real space where carbon atoms are located at sites A and B. (b) The Brillouin zone in reciprocal space of graphene or 2D graphite layer, shaded hexagon and rhombus showing the high symmetry points Γ, K amd M. a_i and b_i (i = 1,2) are the basis and reciprocal lattice vectors respectively.

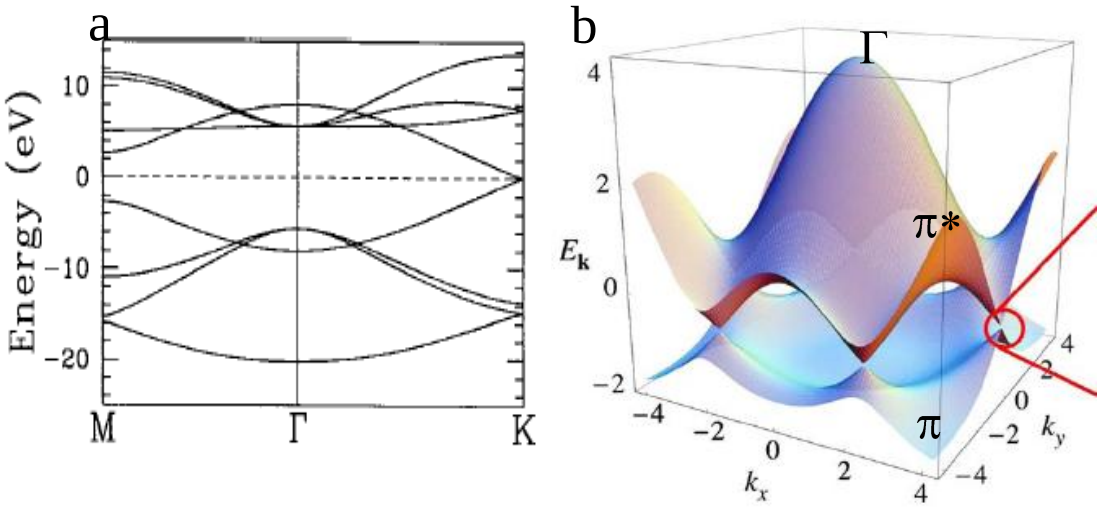

Figure 1.6.[8] (a)Tight binding electronic structure of graphene showing the Γ, M and K high symmetry points. (b) 3D model of (a) with the inclusion of the π and π* states, the K point is also displayed.

transport. Two consequences arise when deriving a nanotube from graphene;

- *i.* The size of the first BZ in the tubule axis direction is determined by the translational period *t*, where $k_{II} = 2\pi / t$ and the wave vector is continuous.
- *ii*. The wave vector is quantized in the direction related to the circumference ($k_\perp$) due to the periodic boundary conditions;

$$\left|k\right\|Ch\right| = 2\pi m \qquad 1.6$$

$$k_\perp = \frac{2\pi}{C} m = \frac{2}{d_t} m \qquad 1.7$$

where *m* is an integer. Therefore in terms of the 2D BZ of graphene, the allowed k states for nanotubes lie along parallel lines separated by a distance given by equation 1.7 which has a dependence on diameter and chirality. Figure 1.7 shows the allowed k states for armchair (*n,n*) tubes, where these quantized wave vectors lie on K points. This results in metallic behavior for nanotubes with this outcome. For zig zag (*n,0*) chiral tubes, the quantized wave vectors lie off centered to the Fermi points allowing energy gaps which give zig zag nanotubes semiconducting or metallic behavior.

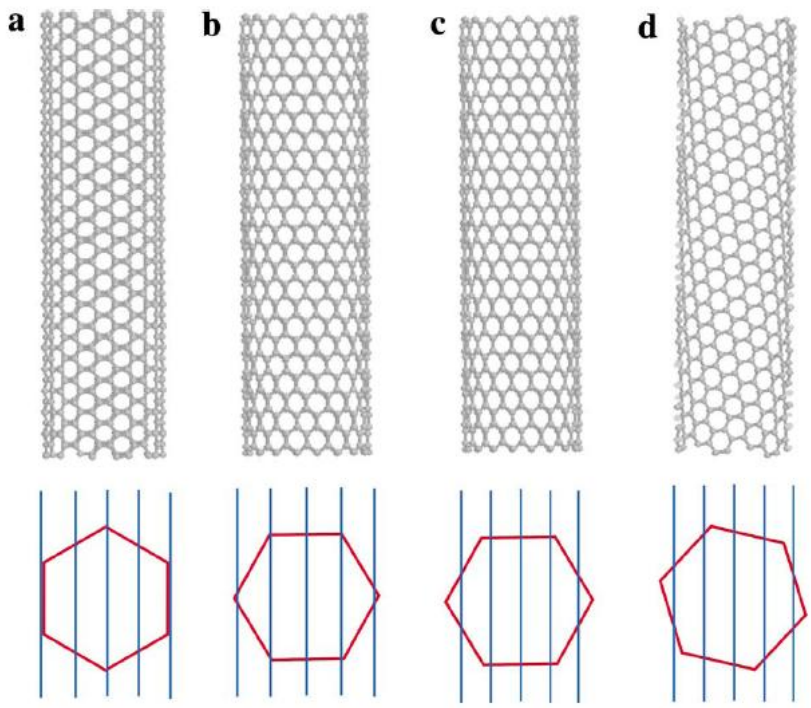

Figure 1.7.[10] Reciprocal space of an armchair nanotube with the parallel lines along the tube axis (a) which results in metallic nanotubes. Reciprocal space of a zig zag nanotube with the parallel lines along tube axis (b and c) which results in semiconducting nanotubes.

1.3. Multi-Walled Carbon Nanotubes

MWCNTs consist of multiple concentric layers of graphite, with the identical interlayer distance of ~0.34 Å. They were discovered first by Iijima [2] in 1991 via the arc discharge method. As grown by the CVD method, MWCNTs are perpendicular to the substrate surface. Mizuno *et al.* [11] demonstrated that the absorptive properties (blackbody behavior) are dependent on the vertical alignment (forest-like structures) normal to substrate.

1.4. Buckypapers

Buckypapers (BPs) are a macroscopic or ensemble form of nanotubes formed into films (composed of SW, DW or MW) that are randomly oriented onto the substrate. Since BPs are formed from the random orientation of nanotubes, the electrical and mechanical properties are a bulk composite effect of the numerous nanotube interactions; such as nanotube-nanotube junctions. The BP orientation plays a role into the macro-properties and hence applications. For instance, when randomly oriented in porous networks parallel to the substrate, it can be used as a composite material, in filtration, for thermal dispersion and electrostatic coatings [12-18]. When grown into "forest" structures, it can be utilized for field emission and photon absorption. Wang *et al.* [19] showed that highly oriented tubes parallel to the substrate can increase the Young's modulus and tensile strength.

1.5. Synthesis Techniques of Nanotubes

Conventionally, CNTs are synthesized by several techniques: (1) chemical vapor deposition (CVD), a gas phase thermal decomposition process; (2) arc discharge, a high current electric arc that goes through high purity graphite electrodes in the presence of catalytic particles in a He atmosphere to form carbon nanotubes and soot on the cathode; and (3) laser ablation, which uses a Nd-YAG high power laser for the vaporization of pure graphite targets or graphite powders in an Ar atmosphere and a furnace temperature of 1200 ^{o}C. Though all

these techniques produce nanotubes, CVD has emerged as the most practical process for the fabrication of CNTs due to the ability to tune experimental parameters. The advantages of the CVD method are the following;

- Provides a means of growing on the bulk scale as well as on substrate surface
- A more versatile technique; SWCNT, DWCNT, and MWCNT can be synthesized by tuning the parameters [20-22] (carbon feedstock gas, temperature, catalyst, etc.)
- Cost effective.

1.6. Mechanism of CVD Growth and Growth Termination

The CVD method uses several metal catalysts, such as iron (Fe), cobalt (Co), and nickel (Ni) in addition to carbon-containing compounds such as methane and ethylene. Both SW- and MWCNTs can be grown via this method dependent on catalyst parameters and feedstock gas. The initial stage typically consists of depositing the catalyst layer onto a substrate. The substrate and catalyst are then heated to a designated temperature. During this heating, the catalyst layer forms “clusters” which vary in size. This size variation accounts for the size distribution observed in nanotubes grown. At the specified temperature (in our case 750 ^{o}C), the catalyst forms a liquid nanoparticle “island” supersaturated with hydrocarbon molecules. The size of the “island” depends on the substrate roughness and reaction parameters (gas flow rate, temperature gradient, etc.) [23-27].

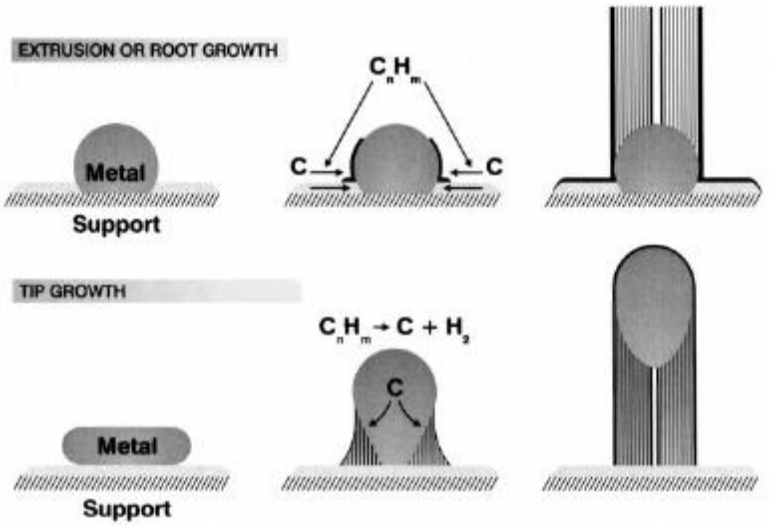

Figure 1.8. [25] Schematic of root or extrusion growth and tip growth mechanisms.

Figure 1.8 is a schematic of the growth models, root and tip, for the CVD method. As depicted in the root growth model, the catalyst particle has a critical radius of curvature, resulting from the extremely small diameter of the catalyst particle, allowing the formation of graphite crystallites with a basal plane formation oriented tangential to the curved surface [23]. The large strain on the basal plane forces them to form the crystalline nanotube structure. In the tip growth model, the formation of the catalyst particle and nucleation of carbon atoms occur as explained above. However in this mechanism, the weak catalyst particle-crystalline nanotube interaction causes the particle to lift-off with the continual growth of the nanotube structures. Growth ceases when the particle surface is covered with carbon and/or when the feedstock is terminated [23].

In Chapter 3, our substrate preparation consisted of depositing the catalyst onto an alumina (Al_2O_3) layer to improve adhesion to the substrate [28].

Kim *et al.* [27] showed that Ostwald ripening and subsurface diffusion led to the loss of catalytic activity which leads to growth termination, as depicted in Figure 1.9. Ostwald ripening is a thermodynamically spontaneous process where larger particles are more energetically favored than smaller particles as a result of surface molecules being less energetically stable than the interior particles. The expression for Ostwald ripening is

$$\langle R \rangle^3 - \langle R \rangle_o^3 = \frac{8\gamma c_\infty \nu^2 D}{9 R_g T} t \qquad 1.4$$

where $\langle R \rangle$ is the average radius of all the particles, γ is the particle surface tension or surface energy, c_∞ is the solubility of the particle material, ν the molar volume of the particle material, D the diffusion coefficient of particle material, R_g is the ideal gas constant and T the absolute temperature. The particle size distribution was described by Ostwald ripening up to 5 minutes of thermal annealing; beyond this point the total number density of particles decreased giving rise to subsurface diffusion of the catalyst into the Al_2O_3 layer. This metal cluster formation within the alumina layer is a result of the surface metal atom's mobility in addition to the long term stability of clusters of metal atoms with bulk-like coordination in the alumina pores [27, 29].

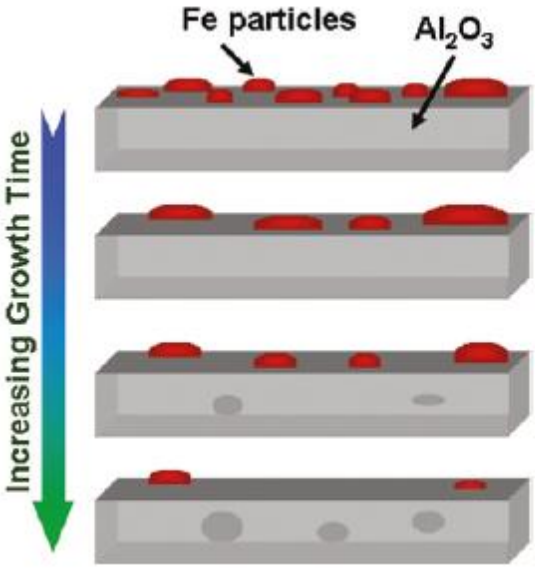

Figure 1.9. [27] Schematic demonstrating the effects of Ostwald ripening and subsurface diffusion of iron particles on an alumina surface.

1.7. Dissertation Organization

This dissertation is organized as follows. Chapter 1 gives an introductory review of the underlying material, carbon, and looks at the 1D allotrope for research purposes. Chapter 2 focuses on the electrophoretic deposition (EPD) of aqueous suspensions of MWCNTs which are deposited onto stainless steel substrates. Further we demonstrate the development of a new and unique procedure to attain free-standing BPs. Chapter 3 focuses on the previous work utilizing vertically aligned MWCNTs as photon absorbers and concentrates on the optimization of CVD grown vertically aligned MWCNTs for direct technology applications for photon absorption in NASA's space and earth-based telescopes. Chapter 4 focuses on methods to improve the absorptive abilities of our films and analysis of our reflectance data using the Kramers-Kronig analysis. Chapter 5

summarizes the content of this dissertation and discusses possible future directions of this work.

Works Cited

1. Guisinger, N.P. and M.S. Arnold, *Beyond Silicon: Carbon-Based Nanotechnology.* MRS Bulletin, 2010. **35**(4): p. 273-279.
2. Iijima, S., *Helical microtubules of graphitic carbon.* Nature, 1991. **354**(6348): p. 56-58.
3. Graham, A., et al., *How do carbon nanotubes fit into the semiconductor roadmap?* Applied Physics A: Materials Science & Processing, 2005. **80**(6): p. 1141-1151.
4. Dreselhaus, M.S., G. Dresselhaus, and P.C. Eklund, *Science of Fullerenes and Carbon Nanotubes.* 1996.
5. Terrones, M., *Science and technology of the twenty-first century: synthesis, properties, and applications of carbon nanotubes.* Annual Review of Materials Research, 2003. **33**(1): p. 419-501.
6. Meyyappan, M., *Carbon nanotubes: science and applications*. 2005: CRC.
7. Kiang, C.H., et al., *Size effects in carbon nanotubes.* Physical Review Letters, 1998. **81**(9): p. 1869-1872.
8. Dresselhaus, M., G. Dresselhaus, and A. Jorio, *Unusual properties and structure of carbon nanotubes.* Annu. Rev. Mater. Res., 2004. **34**: p. 247-278.
9. Wallace, P., *The band theory of graphite.* Physical Review, 1947. **71**(9): p. 622.
10. Dai, H., *Carbon nanotubes: opportunities and challenges.* Surface Science, 2002. **500**(1-3): p. 218-241.
11. Mizuno, K., et al., *A black body absorber from vertically aligned single-walled carbon nanotubes.* Proceedings of the National Academy of Sciences, 2009. **106**(15): p. 6044.
12. Ci, L., et al., *Ultrathick freestanding aligned carbon nanotube films.* Advanced Materials, 2007. **19**(20): p. 3300-3303.
13. Ruoff, R.S. and D.C. Lorents, *Mechanical and thermal properties of carbon nanotubes.* Carbon, 1995. **33**(7): p. 925-930.
14. Datsyuk, V., et al., *Chemical oxidation of multiwalled carbon nanotubes.* Carbon, 2008. **46**(6): p. 833-840.
15. Jason, J.G., et al., *Assembly of well-aligned multiwalled carbon nanotubes in confined polyacrylonitrile environments: electrospun composite nanofiber sheets.* Journal of the American Chemical Society, 2004. **126**(48): p. 15754-15761.
16. Ago, H., et al., *Composites of carbon nanotubes and conjugated polymers for photovoltaic devices.* Advanced Materials, 1999. **11**(15): p. 1281-1285.
17. Safadi, B., R. Andrews, and E. Grulke, *Multiwalled carbon nanotube polymer composites: synthesis and characterization of thin films.* Journal of Applied Polymer Science, 2002. **84**(14): p. 2660-2669.
18. Moisala, A., et al., *Thermal and electrical conductivity of single-and multi-walled carbon nanotube-epoxy composites.* Composites Science and Technology, 2006. **66**(10): p. 1285-1288.
19. Wang, D., et al., *Highly oriented carbon nanotube papers made of aligned carbon nanotubes.* Nanotechnology, 2008. **19**: p. 075609.
20. Nessim, G.D., et al., *Tuning of vertically-aligned carbon nanotube diameter and areal density through catalyst pre-treatment.* Nano Letters, 2008. **8**(11): p. 3587-3593.
21. Grujicic, M., G. Cao, and B. Gersten, *Optimization of the chemical vapor deposition process for carbon nanotubes fabrication.* Applied surface science, 2002. **191**(1-4): p. 223-239.
22. Nessim, G.D., et al., *Precursor gas chemistry determines the crystallinity of carbon nanotubes synthesized at low temperature.* Carbon, 2010. **49**(3): p. 804-810.

23. Kunadian, I., et al., *Growth kinetics of MWCNTs synthesized by a continuous-feed CVD method.* Carbon, 2009. **47**(2): p. 384-395.
24. Yun, Y.H., et al., *Growth mechanism of long aligned multiwall carbon nanotube arrays by water-assisted chemical vapor deposition.* The Journal of Physical Chemistry B, 2006. **110**(47): p. 23920-23925.
25. Sinnott, S., et al., *Model of carbon nanotube growth through chemical vapor deposition.* Chemical Physics Letters, 1999. **315**(1-2): p. 25-30.
26. Nessim, G.D., et al., *The critical role of the underlayer material and thickness in growing vertically aligned carbon nanotubes and nanofibers on metallic substrates by chemical vapor deposition.* Advanced Functional Materials, 2010. **20**(8): p. 1306-1312.
27. Kim, S.M., et al., *Evolution in catalyst morphology leads to carbon nanotube growth termination.* The Journal of Physical Chemistry Letters, 2010. **1**(6): p. 918-922.
28. Hagopian, J.G., et al. *Multiwalled carbon nanotubes for stray light suppression in space flight instruments*. in *Proceedings of SPIE*. 2010: SPIE.
29. Colaianni, M., P. Chen, and J. Yates Jr, *Spectroscopic studies of the thermal modification of the Fe/Al2O3 interface.* Surface science, 1990. **238**(1-3): p. 13-24.

CHAPTER 2

FABRICATION AND CHARACTERIZATION OF BUCKYPAPERS

2.1. Introduction

Since the discovery of carbon nanotubes (CNTs), growth in scientific interest associated with the fabrication of CNT assemblies has been motivated by the desire to incorporate CNTs into devices that exploit their attractive electrical, mechanical, and thermal properties. Macroscopic CNT assemblies, such as yarns, films, and arrays, can be fabricated by an assortment of methods [1-5]. Free-standing CNT films with paper-like morphology, known as buckypapers (BPs), have been demonstrated for applications such as catalysis, filtration, and energy storage [4, 6-10]. BPs have been fabricated using single-walled CNTs [11-15], double-walled CNTs [16, 17] and multi-walled CNTs (MWCNTs) [1, 18-20]. The properties of BPs – electrical conductivity, tensile strength, and specific surface area, to name a few – depend on the composition of the CNTs, e.g., length or single-walled vs. multi-walled, their alignment in the BPs, and whether any polymer binders or fillers are included. For example, the domino pushing technique produces BPs by sequentially compressing vertically aligned arrays of CNTs into highly aligned CNT mats, much like a succession of toppling dominos [1]. The high degree of alignment confers higher electrical conductivity upon the resulting BPs, but consequently, lowers the surface area available for charge storage in applications like supercapcitors, when compared to BPs with randomly

aligned CNTs [1]. One challenge inherent to such a technique is the difficulty accessing thin, sub-50 μm buckypapers, as multiple domino pushing steps are required. Other CNT film fabrication techniques have other disadvantages, such as high impurity content, limited control over lateral dimension, and coupling of the films to the substrate on which they are assembled. Thus, we sought a facile technique to produce BPs, with substantial control over the lateral dimensions and thickness of the film.

We predicted that casting CNTs from a suspension phase, as a form of bottom-up assembly, could provide the desired degree of control over the film dimensions. Of the various techniques to cast films of colloidal materials, electrophoretic deposition (EPD) uniquely facilitates long-range homogeneity of film thickness and morphology, low surface roughness in the films, size scalability, and rapid film deposition [21-24]. EPD combines the processes of electrophoresis and deposition; suspended charged particles are accelerated by the application of an electric field, which drives them to the field-emanating surfaces, where they collect and form a dense deposit. EPD has been used to deposit CNTs onto a variety of substrates and in a variety of architectures [3, 5, 25, 26]; however, the production of free-standing BPs from electrophoretically deposited films has yet to be demonstrated. Motivated by recent work on free-standing multilayered nanoparticle films [27] and on CNT-nanocrystal heterostructures [5], both produced by using EPD, we explored how to produce BPs by liberating electrophoretically deposited CNT films.

This chapter describes a method to fabricate BPs whose thickness and lateral dimensions are tunable with the use of EPD. From an aqueous suspension, MWCNTs were electrophoretically deposited on steel substrates in random alignments, with most of the MWCNTs' length parallel to the substrates. This distribution of materials yielded films that comprised porous networks of the MWCNTs. The deposited films then were mechanically cleaved from their substrates to yield free-standing BPs. A study of the mass and thickness of the films as a function of the number of depositions demonstrated the capacity of this fabrication process to produce films of consistent density. The deposition parameters reported in this paper yielded MWCNT films with thickness in the range of 1–7 μm. Finally, this chapter reports preliminary mechanical testing of the BPs, from which values for the tensile strength and Young's modulus, 14.5 MPa and 3.3 GPa, respectively, were calculated.

The work described in this chapter has been published in the following journal article by Rigueur *et al.* (2010, Carbon 48, pp. 4090-4099) [28].

2.2. Surfactant Characterization

MWCNTs, produced by catalytic carbon vapor deposition and dispersed in water with a proprietary surfactant (Aquacyl AQ0101, 1 wt%, Nanocyl Inc, Belgium, specified average length 1.5 μm, carbon purity > 95%), were employed for our experiments.

Thermogravimetric Analysis

Thermogravimetric analysis (TGA) was performed on the surfactant using an Instrument Specialist TGA-1000 with the data collected in the temperature range of 25^{o} C to 800^{o} C with a heating rate of 10^{o} C/min under a dry nitrogen atmosphere. Figure 2.1 shows the relative mass ratio verses temperature graph of drop casts of as received MWCNTs and centrifuged MWCNTs dispersions. Samples were dried in two alternate temperature regimes; regime 1 at room temperature and regime 2 in a furnace at 120 ^{o}C for ten minutes. TGA curves for the EPD and freestanding films were also obtained. These samples were dried in regime 2, hence their curves are identical to that of the heat dried centrifuged sample.

As shown in the figure (Figure 2.1), the relative mass ratio of the four samples is equivalent at 100 % (represented in scale as 1.0). During the temperature ramp, in the range of 50 ^{o}C to 200 ^{o}C, we observe for the air-dried samples (black and green lines) a 15% – 17% reduction in mass. This is attributed to the evaporation of water and decomposition of other organic material that may be present in our samples. For the heat dried samples (red and blue lines), this phenomena is observed to be no more than a 10% reduction in mass. This suggests that heat drying the samples reduces the excess water.

As the temperature is continually increased, we observe further mass loss of the samples occurring in the temperature range of ~310 ^{o}C to 650 ^{o}C. This region represents the main mass loss, which corresponds to surfactant

degradation and is prevalent for all samples. The TGA curves in this temperature region coincide with those found for anionic surfactants [1]. The air-dried samples show a mass loss of ~ 57% while the heat dried samples show a mass loss of ~ 65%. Beyond 650 ^{o}C, the residual mass is measured to be in the 22% to 25 % range. This suggests the conclusion of surfactant degradation with only MWNTs remaining. It also suggests that the film's mass is composed of mainly surfactant.

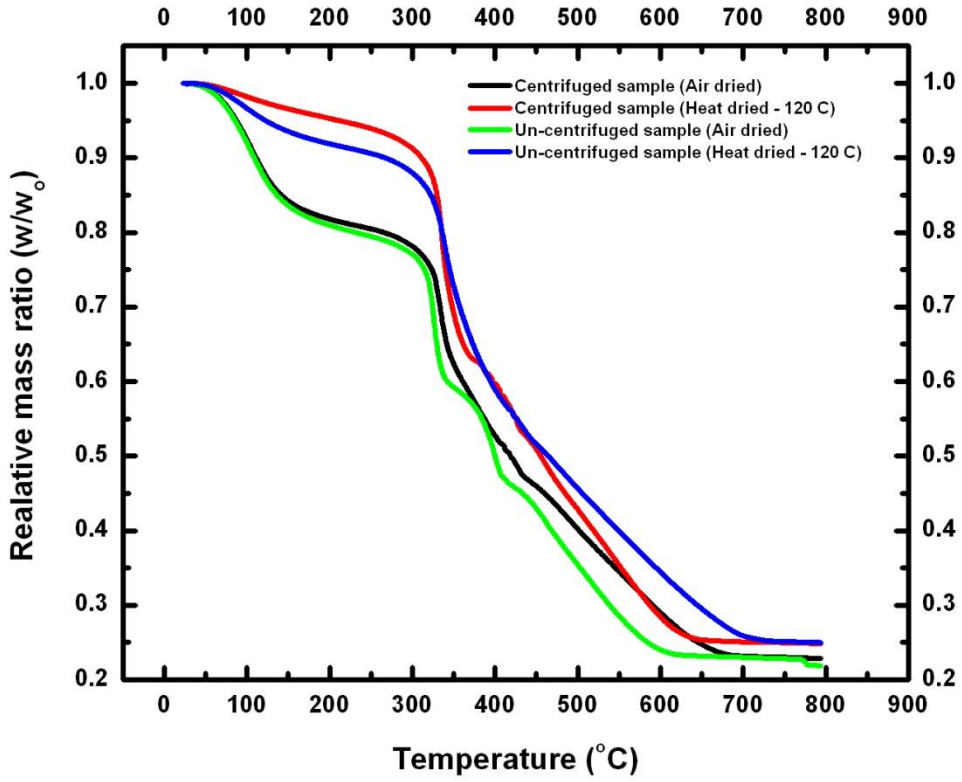

Figure 2.1. TGA curves for as received un-centrifuged MWCNT and centrifuged MWCNT dispersions. Samples were drop-cast and allowed to dry in regular conditions (air) and heat dried at 120^{o}C in a furnace.

Energy Dispersive Spectroscopy

Energy dispersive spectroscopy (EDS) was used to determine the elemental composition of the proprietary surfactant, called X from Nanocyl Inc., used in the MWNT suspension. Characterization was performed on the drop cast area of MWNT solution used for deposition as shown in the scanning electron microscopy (SEM) image of Figure 2.2. Figure 2.3 shows the EDS spectra of the drop cast film, which shows a strong carbon (C) peak affirming the presence of the MWNTs. The sodium (Na) peak present in the spectra suggests that the anionic surfactant used to suspend the MWNTs has Na^+ as a co-ion. The presence of the oxygen (O) peak suggests oxygen-containing molecules consisting of the surfactant.

Figure 2.4 shows the EDS spectra of a freestanding buckypaper. First observation shows the C and O peaks are present though there is the absence of the Na peak. We hypothesize that the absence of the peak comes from the repulsion of the Na^+ ions from the positive electrode or being attracted to the negative electrode during EPD. Further investigation of the negative electrode may strengthen this claim. An EDS of the negative electrode before and after a deposition should clarify the issue.

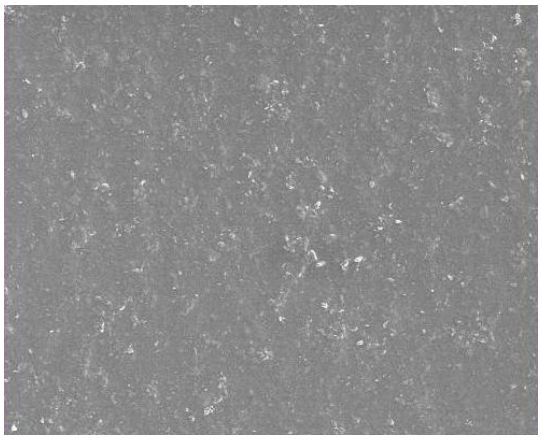

Figure 2.2. SEM image of un-centrifuged drop cast of MWCNT. Area shown in image was used for EDS analysis.

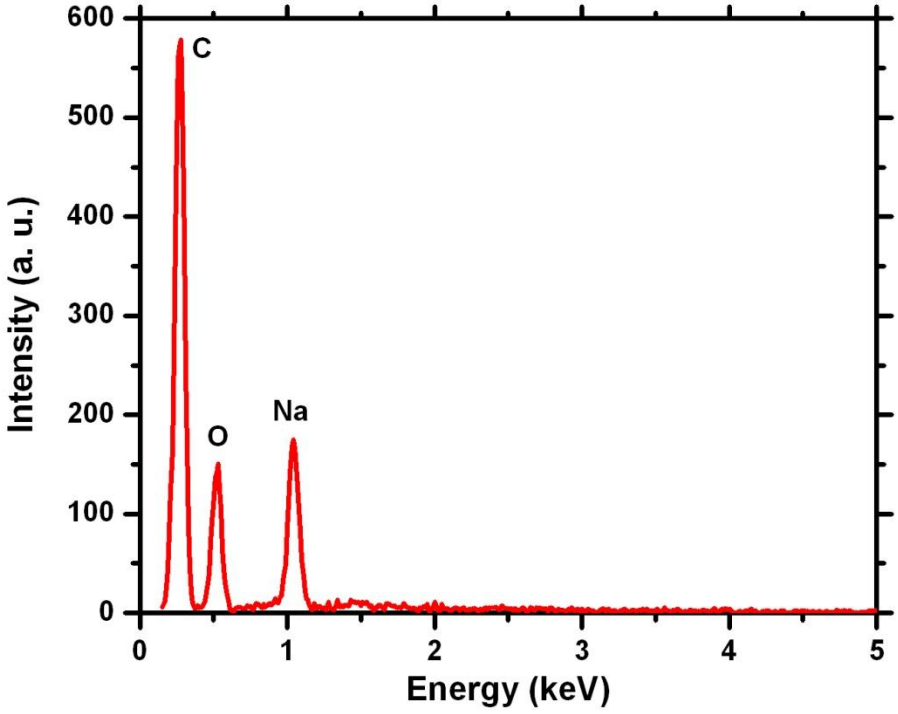

Figure 2.3. EDS spectra of un-centrifuged drop cast of MWNTs on stainless steel substrate. The C peak affirms the presence of MWNTs; the Na peak affirms the elemental composition of the proprietary surfactant and the O peak originates from the surfactant.

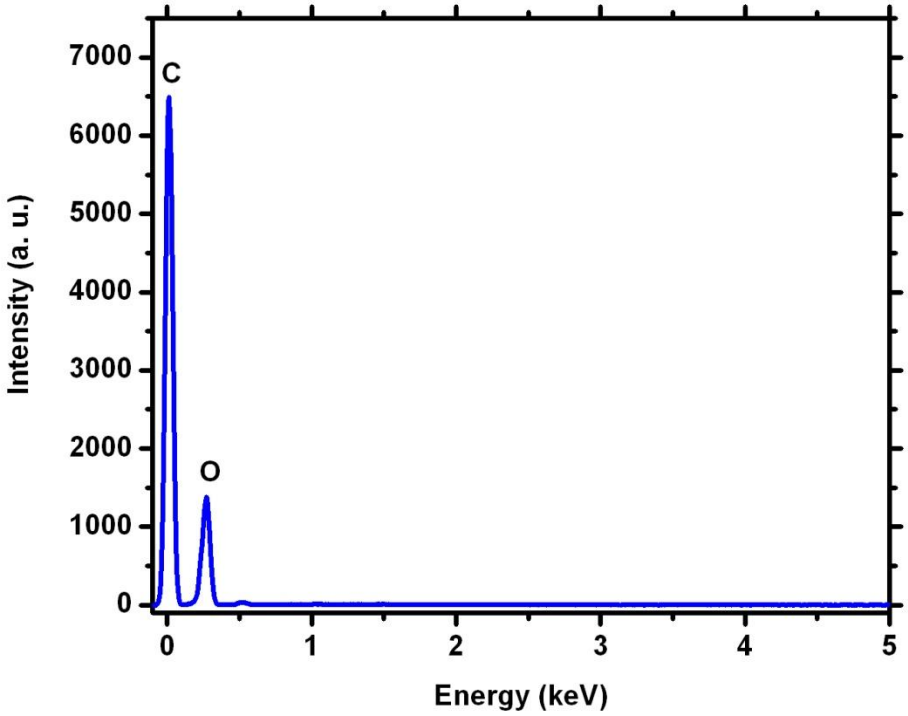

Figure 2.4. EDS spectra of free-standing buckypaper. The C peak affirms the presence of MWNTs and the O peak originates from the surfactant.

Nuclear magnetic resonance (NMR) spectroscopy was performed on the aqueous dispersion of MWNTs. 25 mg of MWNT solution was dispersed in 0.6 ml of deuterated water (D_2O). The ^{13}C NMR measurement of electromagnetic radiation occurred in the frequency region of 600 MHz, with a chemical shift range of 200 ppm and the number of scans (ns) approximately 28,000. The peak at 130.36 ppm represents the aromatic carbon in the MWNTs, the peak at 62.02 ppm identifies a hydroxyl group. The peaks in the 22 – 65 ppm range represent organics with (CH_2) and (CH_3) groups. The peak at 165.12 ppm represents that of a carboxylic acid. NMR spectroscopy on non-surfactant

functionalized MWNTs is necessary to obtain a comparison with that of the surfactant functionalized MWNTs.

2.3. Experimental

As received MWCNT suspensions were centrifuged for 1.5 hours at 3500 rpm (Horizon Premier, Drucker Co.) to remove MWCNT aggregates and excess agglomerated surfactant. The supernatant MWCNT suspension extracted from the centrifugation tubes was employed for EPD. For EPD, 316 stainless steel sheets (McMaster Carr, USA), with a thickness of 1 mm, were cut into electrodes with dimensions of 5 cm x 2.5 cm. These electrodes were ultrasonicated in acetone, rinsed in deionized (DI) water, and dried with a nitrogen stream prior to EPD. We used a standard EPD setup (Figure 2.5) consisting of vertically aligned electrodes in a parallel plate configuration with a separation of ~1 cm. Electrode pairs were dipped in the aqueous MWCNT suspension for 10 minutes. A BK Precision 1787B power supply applied a constant dc voltage of 2.8 V. At the conclusion of the EPD run, the electrodes were extracted from suspension to dry and were maintained at 2.8 V for an additional 5 minutes. This step enabled further densification of the CNT deposit [21, 27, 29, 30], which enhances the homogeneity of the dried film compared to purely evaporative processes. With the electric field assisting with the drying process, the film homogeneity is uniform, allowing the MWCNTs to be tightly packed. The aforementioned step constitutes a single (1X) deposition.

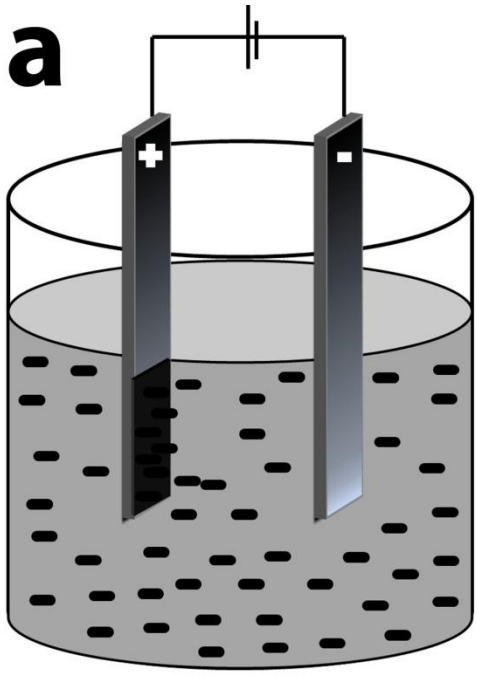

Figure 2.5. EPD scheme for the deposition of films of MWCNTs. The MWCNTs are surface functionalized with a negatively charged proprietary surfactant and deposited onto the positive electrode. The BK Precision power supply applies a voltage (2.8V) across the stainless steel electrodes. The Keithley records the current during EPD. Electrode spacing between electrodes was 1cm.

We used a multiple deposition scheme for our experiments, for which 1X and 3X represented the number of times MWCNTs were deposited onto electrodes. For this scheme, different suspensions, identical in preparation and concentration of MWCNTs, were employed for each single deposition. For example, to create a 2X film, two beakers containing identical, centrifuged suspensions of MWCNTs were used. The first beaker was used for the first (1X) deposition; thereafter, the electrode was extracted and dried with the applied voltage across electrodes. Upon completion of this drying procedure, the electrode was then inserted into the second beaker, which was used for the second (2X) deposition. This process kept the concentration of the suspension constant for the start of each single

deposition. Identical electrical, temporal, and spatial parameters for EPD were employed for each deposition step.

To facilitate removal of the film after air-drying it, the anode was submerged in DI water for 3-12 hours. A mechanical cleavage technique was utilized to liberate the film from the stainless steel substrate. The technique involved the use of a razor blade to assist in the removal of MWCNT films from the stainless steel substrate while still submerged in DI water. We inserted the razor between the film and stainless steel substrate, which caused minimal fraying at the films edges, moving the razor in a direction parallel to the substrate's surface. This process left our films liberated and wholly intact. Films were then extracted from the DI water, placed onto a Teflon sheet, and air-dried. Once dried, films were removed from the Teflon sheet by peeling them off, yielding a freestanding BP.

Transmission electron microscopy (TEM) images of MWCNTs were obtained using a Phillips CM 20 microscope operating at 200 kV accelerating voltage. Zeta potential values of the MWCNTs in suspension were obtained from electrophoretic mobility measurements using a Malvern Zetasizer NanoZS instrument. The surface morphology and topology of deposited films and buckypapers were characterized by scanning electron microscopy (SEM) (Raith eLine, 10kV) and by atomic force microscopy (AFM) (Digital Instruments Nanoscope III) operating in tapping mode. A Dektak 150 Surface Profiler (Veeco Instruments) was used to measure the thickness of deposited films on the steel substrate. The thicknesses of the freestanding BPs were measured by examining the BP edges using SEM. Mechanical measurements of ~ 5 mm wide

by ~ 30 mm long strips of the BPs were performed with a Q800 Dynamic Mechanical Analyzer (DMA) (TA Instruments). The samples were clamped at each end and were loaded at 0.25 N/min along the long axis. Force-strain data were collected. The final point in the force-strain plots corresponded to the fracture, prior to the force dropping to zero.

2.4. Discussion

In this study, we demonstrated how EPD could be incorporated in a technique to assemble MWCNTs into BPs with tunable lateral dimension and thickness. The MWCNTs had an average outer diameter of approximately 25 nm (Figure 2.6a). SEM images in figures 2.6b and 2.6c show films electrophoretically deposited onto stainless steel electrodes from as-received and from centrifuged MWCNT suspensions, respectively. The as-received suspensions contained individually dispersed MWCNTs as well as aggregates of MWCNTs held together by excess surfactant (seen as large white masses in Fig. 2.6b). By centrifuging the as-received suspension, we were able to remove a large quantity of these aggregates from the bulk suspension. The centrifuged suspensions, containing predominantly individual MWCNTs, were used for the multi-step deposition experiments and subsequent liberation process to yield BPs.

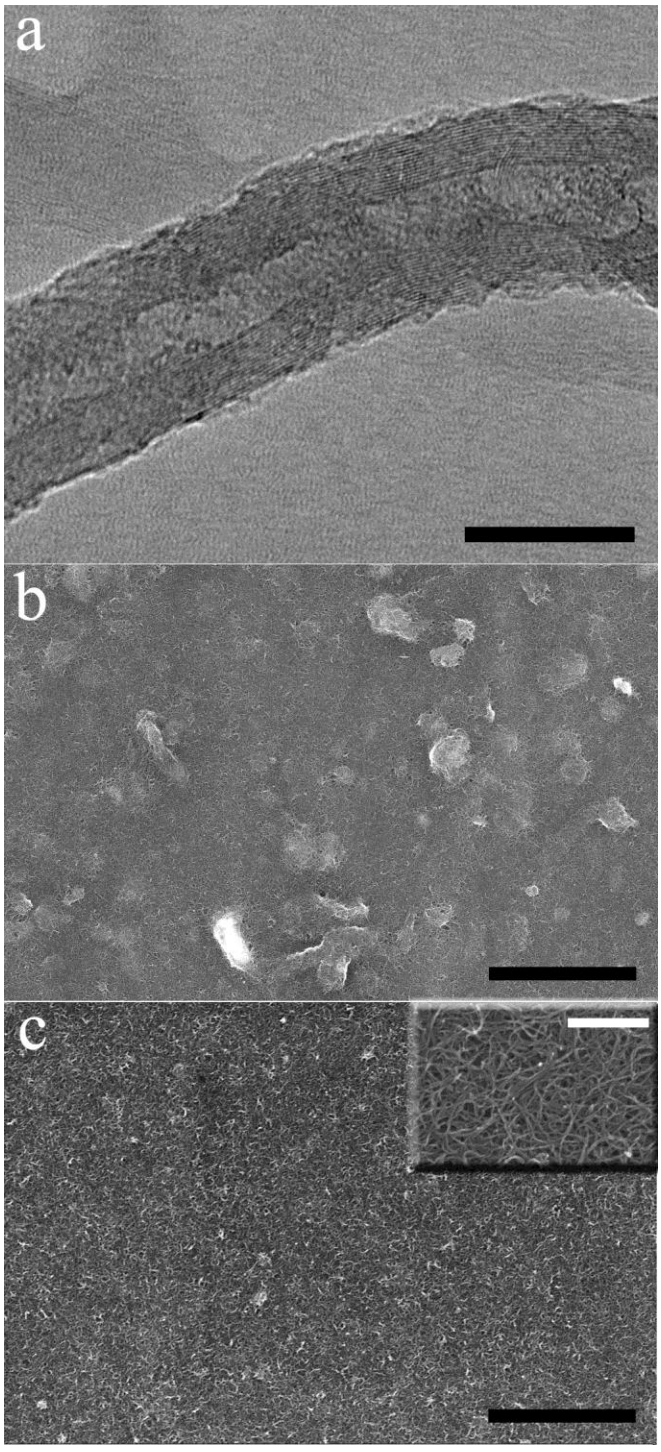

Figure 2.6. (a) TEM of MWNT used in deposition, inner diameter of ~7 nm and outer diameter of ~25nm; scale bar 20 nm. SEM of MWCNT deposited onto stainless steel substrates: (b) as received, scale bar 5 μm and (c) centrifuged MWNTs, scale bar 5 μm. Inset of higher magnification SEM, scale bar 500 nm.

To understand the EPD steps, we investigated the behavior of the colloidal MWCNTs. Measurement of the electrophoretic mobility (μ) of the water-dispersed MWCNTs provided information about the distribution of charges on the surface of the colloids. The electrophoretic mobility $\mu = \frac{v}{|\vec{E}|}$ is defined as the velocity (*v*) of a particle divided by the applied electric field ($|\vec{E}|$), and can be related to the colloid's zeta potential (ζ) by the expression $\left(\mu = \frac{v}{|\vec{E}|} = \frac{\kappa \varepsilon_0 \zeta}{\eta} \right)$, where η is the solvent viscosity, κ is the dielectric constant of the solvent presuming the low particle concentration limit, and ε_0 is the permittivity of free space [31]. The sign of the mobility corresponds to the colloids' charge in the suspension. The electrophoretic mobility distribution of the MWCNTs in water, shown in Figure 2.7, exhibits a single peak at -4.7 ($10^{-4}cm^2V^{-1}s^{-1}$). This result shows that the proprietary surfactant generates a negative charge on the nanotubes when they are suspended in water. From this result, we anticipated that MWCNTs would deposit on the positive electrode during EPD, which was indeed the outcome of EPD.

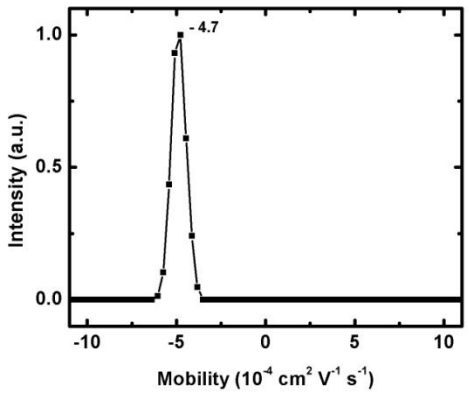

Figure 2.7. Distribution of electrophoretic mobility for the centrifuged MWCNTs in an aqueous dispersion.

The deposition kinetics of EPD are described by the Hamaker equation $m(t) = \int_{t_1}^{t_2} \mu AEcdt$, according to which the deposited mass *m* depends linearly on the electrophoretic mobility μ, surface area of deposition electrode *A*, electric field strength *E*, and particle mass concentration in suspension *c,* integrated over time *t*. Over the course of an EPD run, solids are depleted from the suspension as they enter the growing deposit. Unless material is replenished during the run, the particle concentration decreases with time. In the work of Sarkar and Nicholson[32], it was shown that maintaining a constant concentration of solids during EPD yields a greater mass of deposit than allowing the solids concentration to decrease during EPD, assuming that a constant voltage is applied during EPD. Therefore, to increase the quantity of MWCNTs deposited into films, we performed the 2X and 3X EPD runs in 10-minute increments using a fresh suspension for each increment, rather than doing 20 and 30 minute runs,

respectively, from the same starting suspension. With this protocol, we better approximated the constant-concentration condition, compared to a 30 minute single solution process. This protocol was comparable to the constant voltage-constant concentration condition of Sarkar and Nicholson.

For the constant voltage-constant concentration condition, Sarkar and Nicholson also demonstrated that the quantity of deposited material is nonlinear with respect to the deposition time[32] or, in our case, the number of depositions. The Hamaker equation has a contribution from the electric field strength E, and the buildup of negatively charged particles and ions at the positive-electrode surface can decrease the effective field in the suspension for a given applied voltage. Thus, in our experiments, which used constant voltage, we expected to see a nonlinear trend in the quantity of deposited material with respect to the number of depositions.

Figure 2.8a shows the mass of the deposited films as a function of the number of depositions. The result here is in agreement with the prediction based on the Sarkar and Nicholson work. Figure 2.8b shows the thickness of the deposited MWCNT films as a function of the number of depositions. These thickness measurements were obtained by contact stylus profilometry of the MWCNT films prior to their liberation from the stainless steel substrates. The similar trends in the mass plot and in the thickness plot suggest that the film density does not change drastically over the course of 1X to 3X depositions. We calculated the average density to be 1.23 ± 0.04 g/cm^3.

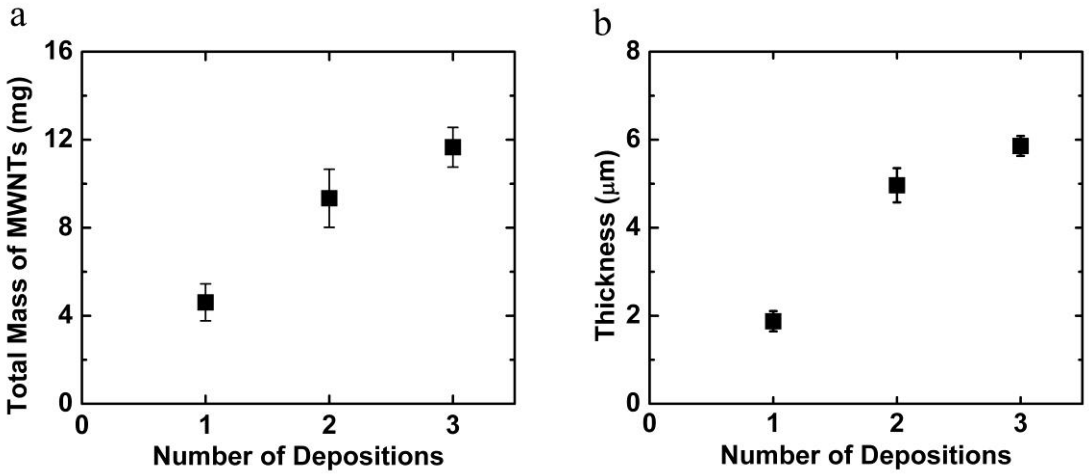

Figure 2.8. Plots of (a) total mass and (b) thickness of MWCNTs films on stainless steel electrodes as functions of the number of depositions.

We discuss next the currents measured during the 1X, 2X, and 3X depositions. As the thickness of the already-deposited film increased, the current measured during EPD decreased (Figure 2.9). Although individual CNTs are highly conductive along their axial direction, the random orientation of MWCNTs in our films and the presence of surfactant coating of the MWCNTs mean that the deposited film contributes to an increase in the resistance at the deposition surface compared to that of the bare stainless steel. However, because the MWCNT films are porous, the resistance is not increased in proportion to the thickness, and therefore the current does not decrease in proportion to the thickness of the already-deposited film.

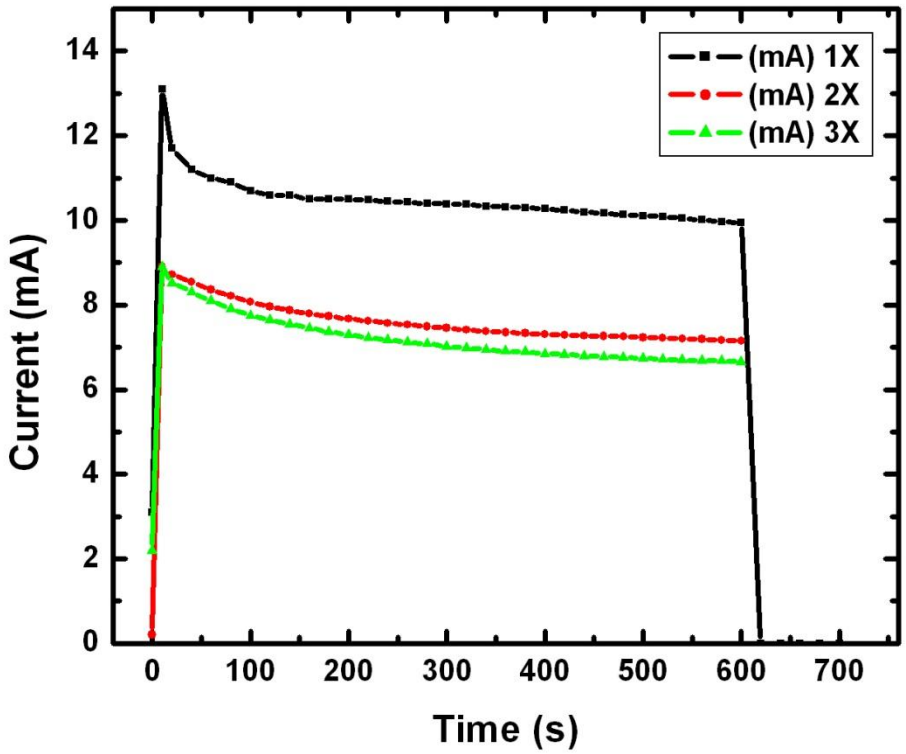

Figure 2.9. Current vs. time for the multi-deposition scheme. The initial spike in the current was due to the insertion of the electrodes into the solution of MWCNTs. The extraction of the electrodes occurred after 600 s. The additional film layers acted as resistive layers and as capacitive dielectric layers, which affected the measured current.

Once we demonstrated the capabilities to perform multiple electrophoretic depositions, the next objective was to liberate these surfactant-coated MWCNTs film from the stainless steel substrate. Figure 2.10a shows the MWCNTs deposited via EPD on the stainless steel, prior to film liberation. These samples were then submerged into DI water for 3-12 hours where the films porous nature allowed water to permeate through. Self-liberation of films from the substrate occurred via warping and use of a razor blade facilitated the lift-off of intact films.

The substrates are not damaged by the mechanical cleavage technique and are reused for other depositions. Figure 2.10e and 2.10f show the SEM images of a partially liberated film from the stainless steel substrate. We observe that once the MWCNT film has been liberated from the stainless steel, there are no remnants of the deposition.

Figure 2.10b displays a dried free-standing BP once it has been liberated and dried. Aside from minimal fraying at the film edges, our lift-off technique facilitated the removal of a wholly intact film. These MWCNT films exhibited paper-like flexibility, (Figure 2.10c). Figure 2.10d illustrates the scalability of our novel EPD lift-off process; larger or smaller freestanding BPs can be fabricated by simply changing the size of the electrodes.

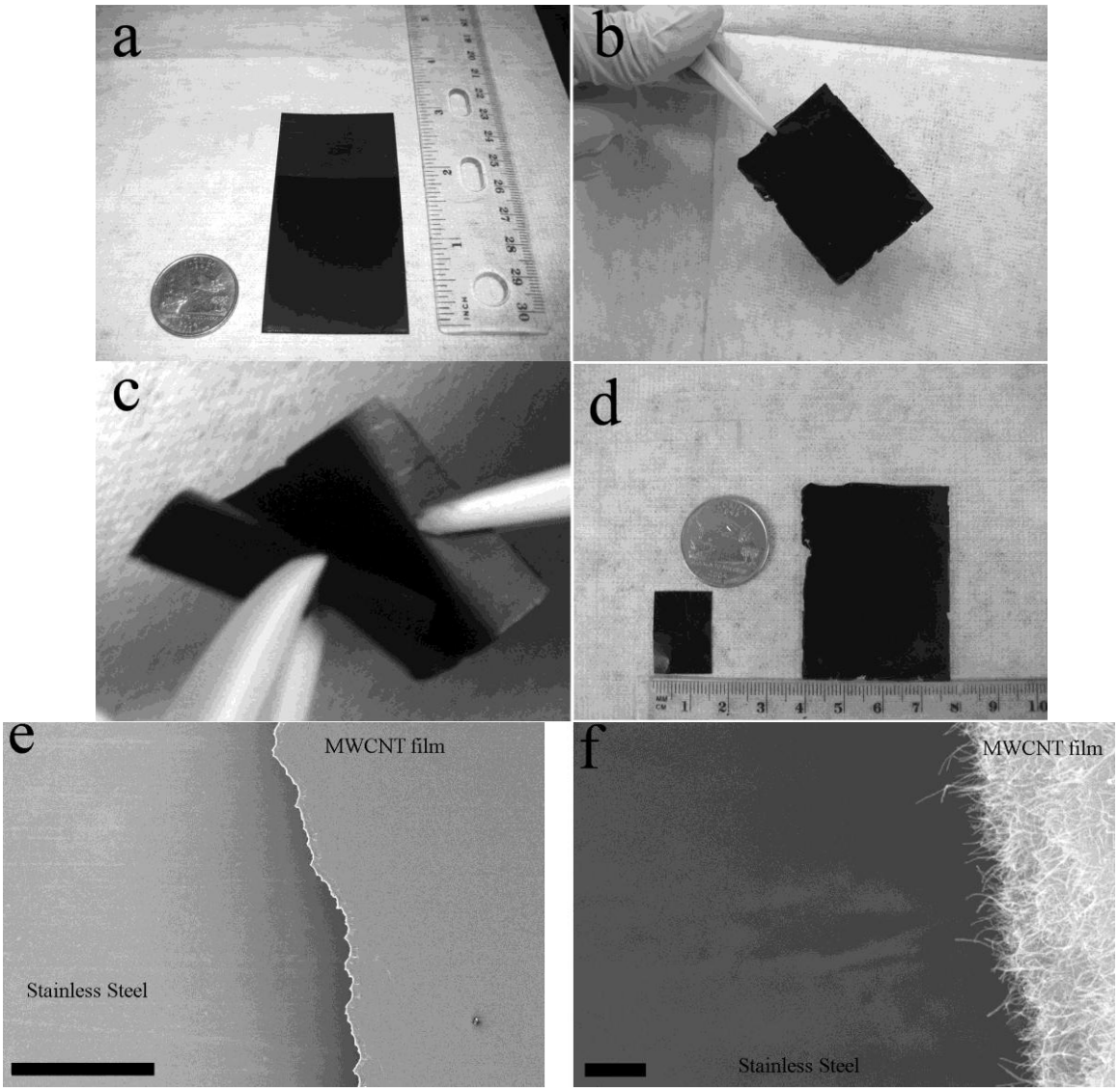

Figure 2.10. (a) MWCNTs deposited on a stainless steel electrode prior to liberation; (b) image of the freestanding buckypaper fabricated from the mechanical cleavage technique. Film dimensions are 3.5 cm x 4.0 cm; (c) demonstration of films flexibility; and (d) demonstration of the film's size scalability, which depends on the electrodes dimensions. (e) - (f)SEM images of a partially liberated MWCNT film from the stainless steel substrate showing complete film liberation; scale bar (e) 300 μm and (f) 500 nm.

From high-magnification SEM imaging (Figure 2.6c inset), we see that the electrophoretically deposited MWCNTs lie in random orientations on the electrode, forming a porous network. Examination of the 1X and 3X films' surfaces via AFM, as seen in Figures 2.11a and 2.11b, revealed that MWCNTs in both samples have regions that project outward from the surface. These protruding sections contribute to the films' overall surface roughness. Using the AFM Nanoscope software, we measured the root-mean-square (rms) roughness of the 1X and 3X samples: 14.4 ± 0.1 nm and 14.5 ± 0.1 nm, respectively. From these data, we noted that the repeated depositions to increase the films' thickness apparently did not alter the films' surface topology. This finding reiterated the utility of EPD to deposit MWCNT films over a large range of lateral dimensions and thicknesses en route to producing free-standing BPs.

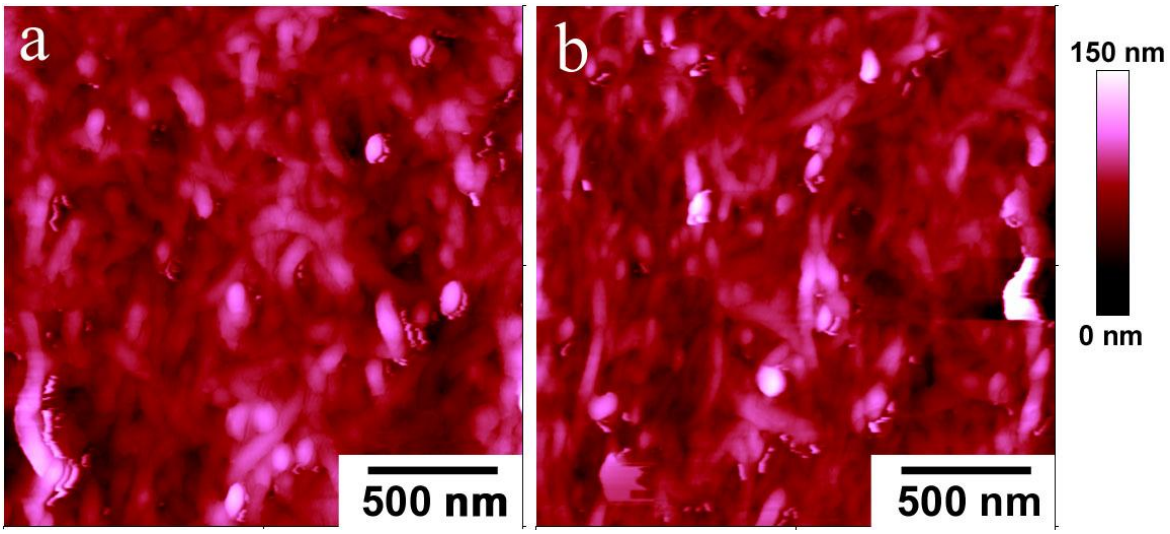

Figure 2.11. AFM images of (a) 1X and (b) 3X film deposited on stainless steel. RMS roughness of films is 14.4 and 14.5 nm, respectively.

Once the films were liberated from the stainless steel substrate, we characterized the mechanical properties of our BPs by static load testing, using a DMA Q800. Samples for the DMA were prepared by cutting the BPs into 5 mm x 30 mm strips. The applied load was parallel to the long axis of the film. From the acquired force vs. % strain data, we calculated and plotted the stress vs. % strain graphs for our BPs. To calculate the stress for a given sample, the cross-sectional areas of the BP strips were determined by using SEM to measure the strips' thicknesses. Figure 2.12a and 2.12b shows the SEM of 1X and 3X samples with thicknesses of 3.8 ± 0.2 μm and 6.9 ± 0.5 μm, respectively. We note that these thickness values are greater than the respective values reported from stylus profilometry. The use of SEM to visualize imperfectly defined edges could have led to overestimating the thickness of the films compared to the thickness measured by profilometry. However, by overestimating the thickness of the films, we ensure that we do not overstate the strength and modulus of the films, since these values are calculated with cross-sectional area (of which thickness is a factor) in the denominator.

Figure 2.12c and 2.12d show representative force-strain and stress-strain plots for our thinnest and thickest BPs as measured by SEM. The stress (σ) values were obtained by dividing the force (F) values by the cross-sectional area of the samples, defined as $A = w \times t$, where w is the width of the sample and t is its thickness. Both plots exhibited an initially flatter slope that steepens at higher loads. We attributed the initial flatter slope to the relaxation of wrinkles in the samples produced during the drying step. Other groups [33] studying BPs have

observed this similar relaxation behavior during tensile load to failure. In addition, once crack formation and propagation begins the process is irreversible if the load is removed. This suggests that BP films are not elastically inclined to return to their original state and will lack a plastic deformation region (strain hardening or necking). Therefore, we would expect not to see a drastic decrease in the forces at the fracture point because the ultimate tensile strength and the yield strength are the same as shown in figure 2.12d. The procedure used to obtain the tensile strength and Young's modulus of our BPs is as follows. The ultimate tensile strength, in MPa, occurred at the samples' fracture point, which was at the maximum strain value in Figure 8d. The Young's modulus was calculated using the following equation $E = \left(\frac{\sigma_2 - \sigma_1}{100(\%\varepsilon_2 - \%\varepsilon_1)} \right)$, where σ_1 and σ_2 are different values of stress on the steeper linear portion of the plot and $\%\varepsilon_1$ and $\%\varepsilon_2$ are their respective % strain values.

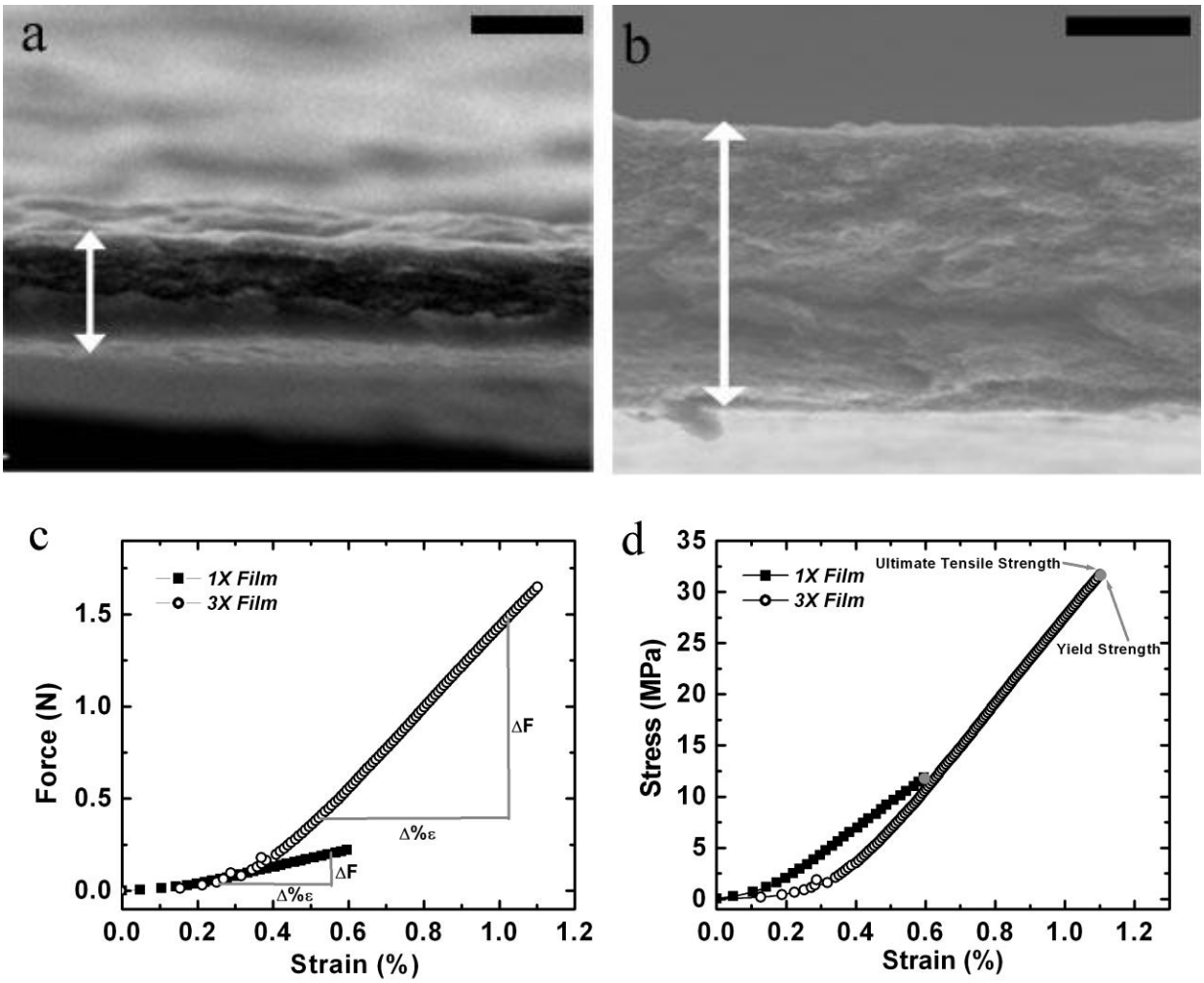

Figure 2.12. Cross section SEM images, of 1X (a) and 3X (b) buckypapers with thicknesses of 3.8 μm and 6.9 μm respectively: Scale bars are (a) 3 μm and (b) 2.5 μm. Graphs of (c) force - % strain, ΔF is the change in force value and Δ%ε is the change in strain value (d) stress - % strain of 1X and 3X buckypapers.

Table 2.1 shows the associated values for the 3X BPs that we produced. Our values compared quite favorably to the results from other BP fabrication techniques and for other types of carbon nanotube constituents, especially considering that the MWCNTs of our samples were covered with a surfactant that can attenuate the attractive interaction between pairs of nanotubes. The lower value of Young's modulus for sample 5 likely is a result of macro- and micro-wrinkles in the sample originating from the drying procedure. As the sample is loaded, these wrinkles can be relaxed with significantly less force than is needed to dislocate the MWCNTs, so they are surmised to have a downward effect on the slope of force-strain curve, thereby reducing the Young's modulus. The higher tensile strength for sample 3 compared to the other four samples cannot be explained readily from the observed MWCNT arrangement in the BPs. Because the samples for mechanical measurement were cut from the larger as-liberated BPs and selected at random, it is possible that a sample from the BP edge could exhibit different properties than those from within the center of the BP, since the EPD behavior at electrode edges and air-liquid interfaces is different from the EPD behavior at the center of the electrode due to fringe field effects and possible meniscus and evaporation effects. The manifestation of these effects in the mechanical properties of the BPs will be the subject of future investigation.

Table 2.1. Comparison of our BPs to other fabrication methods.

Samples	Tensile Strength (MPa)	Young's Modulus (GPa)
1	10.1	3.60
2	12.5	3.38
3	27.0	3.99
4	12.7	3.3
5	10.2	2.20
Average	**12.7**	**3.27**

Table 2.2 shows the comparison of the tensile strength and Young's modulus of BPs in this study with those prepared by other methods. Xu et al. [19] through a filtration method used a temperature based acid treatment to enhance the interaction of MWCNTs, as where we used an EPD procedure. Comparatively, our BPs exhibit greater tensile strength and Young's modulus values. The strongest BPs described by Xu et al had a tensile strength and Young's modulus of 7.5 MPa and 785 MPa respectively with an acid treatment temperature of 110 ^{o}C. These values were considerably less than those reported by Zhang et al. [33] who increased their BP strength by also performing acid treatments.

Table 2.2. Tensile strength and Young's modulus comparison of BPs.

Authors	Constituents / Film Type	Tensile Strength (MPa)	Young's Modulus (GPa)
Zhang et al. [2]	SWNTs film	10 16 71 74	0.8 1.4 2.9 5
Pham et al. [34]	SWNTs BP	6.49	2.29
Xu et al. [19]	MWCNTs BP	4.3 4.6 7.5 6.0 4.5	0.426 0.439 0.785 0.557 0.455
This study.[28]	**MWCNTs BPs**	**12.7**	**3.27**

Investigations of the fracture sites of the 1X (Figure 2.13a and 2.13b) and 3X (Figure 2.13c and 2.13d) BPs provided insight into the possible mechanisms for failure within the films. In Figure 2.13a a 1X BP films failure region is shown, in which individual MWCNTs were extended from a randomly oriented network. Some fraction of the nanotubes was oriented in the direction of applied load. We considered the BPs as a multi-layered fibrous composite, [35] for which a "fiber" in our material consists of the local network of randomly oriented MWCNTs. The implication here is that during the application of the load, individual MWCNT fibers began to unravel via tube-tube shearing from each other within the randomly oriented network, producing the observed failure of the bulk BPs. As the failure propagated across the sample, as depicted in Figure 2.13b, bridging [36] occurred. A MWCNT bridge forms when a single MWCNT is simultaneously connected to opposite sides of a fracture site within a film that has experienced

tensile loading. Figure 2.13c illustrated that several MWCNTs were bridging the two sides of a fissure at a point of deformation in the buckypaper.

From Figure 2.13c**,** we perceived another failure mechanism, slip, which we attributed to the multiple-deposition approach, which closely packs each of the deposited layers. For our BP system, this was observed in the closely packed multi-layered structure of the 3X BPs. This type of failure was noticeable along both fracture sites of the 3X samples. From observations of the 1X and 3X BPs, we concluded that the plastic deformation range increased as we fabricated thicker films in a laminar, layer-by-layer architecture, thereby increasing the overall strength of the buckypapers. Figure 2.13d shows the deformation that occurred both horizontally and vertically within our multi-layered films. As the MWCNT deposit dried onto the substrate with the voltage still applied, densification occurred, which left minimal space between the MWCNTs layers (for example, between the 1X and 2X layers or between the 2X and 3X layers). In a 3X deposition, for example, the solution-phase MWCNTs that arrived at the electrode's surface to deposit and to adhere onto the previously cast MWCNTs did not substantially intertwine with the network of underlying MWCNTs. This formed nearly isolated, bulk layers of carbon nanotubes that comprised the overall cast film. The interfaces between these 1X, 2X, and 3X layers gave rise to the observed slip plane interfaces (Figure 2.13c).

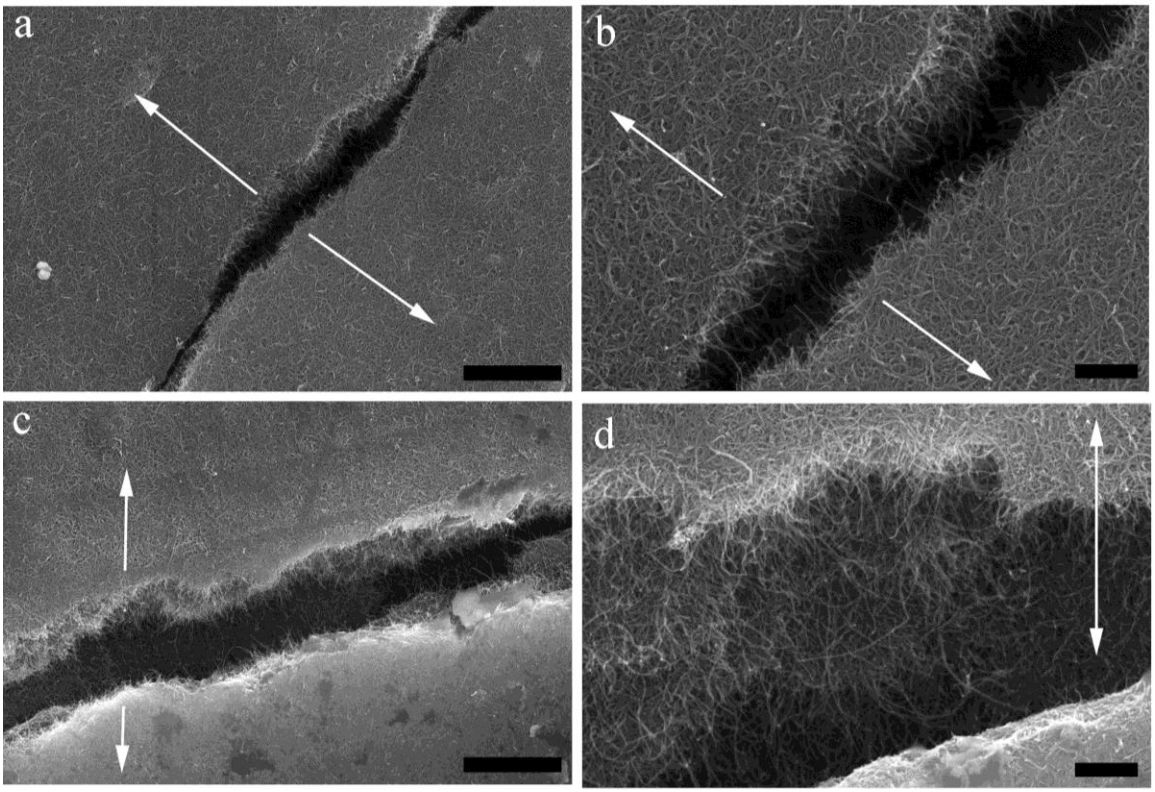

Figure 2.13. SEM images of samples subjected to load to failure testing, arrows indicate direction of applied load. (a) 1X buckypaper; scale bar 2 μm (b) unraveling (tube-tube shearing) of randomly oriented MWCNT network; scale bar 500 nm (c) 3X buckypaper; scale bar 2 μm and (d) 3X failure region similar to 9(b) for layer by layer deposition; scale bar 500 nm.

Failure of these randomly distributed networks occurred when the MWCNTs became unraveled via nanotube-nanotube shearing. The SEM images in Figure 2.13 suggested that with each deposited layer, stress propagation occurred in the vertical and horizontal directions, leading to the unraveling phenomena of the nanotubes, as they were seen protruding from the bulk of the films (Figs. 2.13b and 2.13d). In a multi-deposited buckypaper, the appearance of parallel but staggered fracture sites suggested that stress did not propagate as readily across the deposition interfaces. Instead, failure transpired when a

critical number of nanotube-nanotube failure events were realized in each layered MWCNT network. The result was that multiple depositions engendered greater film strength by suppressing the accumulation of failures in one region of the film due to the random orientation between each deposited interface.

2.5. Conclusion

In this study, we have described and demonstrated a technique for the rapid production of buckypapers by first performing EPD of MWCNTs onto stainless steel electrodes and then liberating the film of MWCNTs using mechanical cleavage. We have shown the capability to vary the thicknesses of these films by using a multi-deposition scheme. Conceivably, the film thicknesses could be tuned outside of the 1 μm to 7 μm range we have shown by varying the duration of each deposition step and by varying the total number of deposition steps. Preliminary measurement of the mechanical properties of our BPs showed them to have an average tensile strength and Young's modulus of 14.5 MPa and 3.3 GPa, respectively. These values compare quite favorably to values reported for buckypapers prepared from other carbon nanotube types and via other fabrication methods. Finally, the BPs prepared by our technique are flexible and contain nanotubes in a random porous network, which suggest possible use of these BPs in applications such as filtration and energy storage.

Works Cited

1. Wang, D., et al., *Highly oriented carbon nanotube papers made of aligned carbon nanotubes.* Nanotechnology, 2008. **19**: p. 075609.
2. Zhang, S., et al., *Solid-state spun fibers and yarns from 1-mm long carbon nanotube forests synthesized by water-assisted chemical vapor deposition.* Journal of Materials Science, 2008. **43**(13): p. 4356-4362.
3. Boccaccini, A.R., et al., *Electrophoretic deposition of carbon nanotubes.* Carbon, 2006. **44**(15): p. 3149-3160.
4. Du, C. and N. Pan, *Supercapacitors using carbon nanotubes films by electrophoretic deposition.* Journal of Power Sources, 2006. **160**(2): p. 1487-1494.
5. Mahajan, S., et al., *Carbon nanotubeâ€"nanocrystal heterostructures fabricated by electrophoretic deposition.* Nanotechnology, 2008. **19**: p. 195301.
6. Frackowiak, E., et al., *Supercapacitors based on conducting polymers/nanotubes composites.* Journal of Power Sources, 2006. **153**(2): p. 413-418.
7. Du, C., J. Yeh, and N. Pan, *Carbon nanotube thin films with ordered structures.* Journal of Materials Chemistry, 2005. **15**(5): p. 548-550.
8. Kim, J.H., et al., *Fabrication and electrochemical properties of carbon nanotube film electrodes.* Carbon, 2006. **44**(10): p. 1963-1968.
9. Futaba, D.N., et al., *Shape-engineerable and highly densely packed single-walled carbon nanotubes and their application as super-capacitor electrodes.* Nature Materials, 2006. **5**(12): p. 987-994.
10. Pushparaj, V.L., et al., *Flexible energy storage devices based on nanocomposite paper.* Proceedings of the National Academy of Sciences, 2007. **104**(34): p. 13574.
11. Sreekumar, T., et al., *Single-wall carbon nanotube films.* Chemistry of Materials, 2003. **15**(1): p. 175-178.
12. Berhan, L., et al., *Mechanical properties of nanotube sheets: Alterations in joint morphology and achievable moduli in manufacturable materials.* Journal of Applied Physics, 2004. **95**: p. 4335.
13. Skakalova, V., et al., *Effect of chemical treatment on electrical conductivity, infrared absorption, and Raman spectra of single-walled carbon nanotubes.* Journal of Physical Chemistry B, 2005. **109**(15): p. 7174-7181.
14. Dettlaff-Weglikowska, U., et al., *Effect of SOCl2 treatment on electrical and mechanical properties of single-wall carbon nanotube networks.* Journal of the American Chemical Society, 2005. **127**(14): p. 5125-5131.
15. Teague, L.C., et al., *Effects of ozonolysis and subsequent growth of quantum dots on the electrical properties of freestanding single-walled carbon nanotube films.* Chemical Physics Letters, 2007. **442**(4-6): p. 354-359.
16. Gong, T., et al., *Connection of macro-sized double-walled carbon nanotube strands by bandaging with double-walled carbon nanotube films.* Carbon, 2007. **45**(11): p. 2235-2240.
17. Wei, J., et al., *Ultrathin Singleâ€"Layered Membranes from Doubleâ€"Walled Carbon Nanotubes.* Advanced Materials, 2006. **18**(13): p. 1695-1700.
18. Ci, L., et al., *Ultrathick freestanding aligned carbon nanotube films.* Advanced Materials, 2007. **19**(20): p. 3300-3303.

19. Xu, G., et al., *The feasibility of producing MWCNT paper and strong MWCNT film from VACNT array.* Applied Physics A: Materials Science & Processing, 2008. **92**(3): p. 531-539.
20. Cooper, S.M., et al., *Gas permeability of a buckypaper membrane.* Nano Letters, 2003. **3**(2): p. 189-192.
21. Islam, M.A. and I.P. Herman, *Electrodeposition of patterned CdSe nanocrystal films using thermally charged nanocrystals.* Applied Physics Letters, 2002. **80**(20): p. 3823-3825.
22. Mahajan, S., et al., *Structural properties of electrophoretically deposited europium oxide nanocrystalline thin films.* Journal of Materials Science, 2006. **41**(24): p. 8160-8165.
23. Wong, E.M. and P.C. Searson, *ZnO quantum particle thin films fabricated by electrophoretic deposition.* Applied Physics Letters, 1999. **74**: p. 2939.
24. Maenosono, S., T. Okubo, and Y. Yamaguchi, *Overview of nanoparticle array formation by wet coating.* Journal of Nanoparticle Research, 2003. **5**(1): p. 5-15.
25. Thomas, B., A. Boccaccini, and M. Shaffer, *Multiâ€Walled Carbon Nanotube Coatings Using Electrophoretic Deposition (EPD).* Journal of the American Ceramic Society, 2005. **88**(4): p. 980-982.
26. Cho, J., et al., *Characterisation of carbon nanotube films deposited by electrophoretic deposition.* Carbon, 2009. **47**(1): p. 58-67.
27. Hasan, S.A., D.W. Kavich, and J.H. Dickerson, *Sacrificial layer electrophoretic deposition of free-standing multilayered nanoparticle films.* Chemical Communications, 2009(25): p. 3723-3725.
28. Rigueur, J.L., et al., *Buckypaper fabrication by liberation of electrophoretically deposited carbon nanotubes.* Carbon. **48**(14): p. 4090-4099.
29. Hasan, S.A., et al., *Electrophoretic deposition of CdSe nanocrystal films onto dielectric polymer thin films.* Thin Solid Films, 2009. **517**(8): p. 2665-2669.
30. Islam, M.A., et al., *Addition, suppression, and inhibition in the electrophoretic deposition of nanocrystal mixture films for CdSe nanocrystals with gamma-Fe2O3 and Au nanocrystals.* Nano Letters, 2003. **3**(11): p. 1603-1606.
31. O'Brien, R.W. and L.R. White, *Electrophoretic mobility of a sperical colloidal particle.* J. Chem. Soc., Faraday Trans., 1978. **2**(74): p. 1607-1626.
32. Sarkar, P. and P.S. Nicholson, *Electrophoretic deposition (EPD): mechanisms, kinetics, and application to ceramics.* Journal of the American Ceramic Society, 1996. **79**(8): p. 1987-2002.
33. Pham, G.T., et al., *Mechanical and electrical properties of polycarbonate nanotube buckypaper composite sheets.* Nanotechnology, 2008. **19**(32): p. -.
34. Pham, G.T., et al., *Mechanical and electrical properties of polycarbonate nanotube buckypaper composite sheets.* Nanotechnology, 2008. **19**: p. 325705.
35. Curtin, W.A., *Dimensionality and size effects on the strength of fiber-reenforced composites.* Composites Science and Technology, 1999. **60**.
36. Malik, S., et al., *Failure mechanism of free standing sigle-walled carbon nanotube thin films under tensile load.* Phys. Chem., 2004. **6**: p. 3540-3544.

CHAPTER 3

OPTIMIZATION OF MULTI-WALLED CARBON NANOTUBE PHOTON ABSORBERS FOR MID-AND FAR-INFRARED STRAY LIGHT SUPPRESSION IN SPACE INSTRUMENTATION

Chapter Overview

In this chapter, I discuss the research conducted at the National Aeronautics and Space Administration (NASA) Goddard Space Flight Center (GSFC) for the optimized growth of catalyst assisted chemical vapor deposition (CVD) nanotubes for the improvement of absorption in vertically aligned (VA) films. Films of VA-nanotubes have been shown experimentally to be excellent absorbers close to that of unity, theoretically and experimentally [1, 2]. We hypothesized that by optimizing the growth process we would be able to increase film height and successively lower the density, allowing us to improve film absorption. We describe our findings on the effects of optimization and characterize our VA-nanotube films. We conclude by describing the effects of the optimization process on our films.

3.1. Introduction

A Blackbody Material

In physics, a blackbody, a concept first introduced by Kirchhoff [3], is a theoretical object that absorbs all incident light, due to the lack of transmittance and reflection. As such, it has an appearance at room temperature which is "super black." The definition of this "blackness" is described by the emissivity (e)

which is equivalent to unity, where we define e as the ratio of radiated energy by an object to that of a blackbody. In thermal equilibrium a blackbody emits blackbody radiation (electromagnetic radiation) according to Planck's Law of radiation given by

$$u(\omega) = \frac{\hbar}{\pi^2 c^3} \frac{\omega^3}{\exp(\hbar\omega/\tau) - 1} \qquad 3.1$$

where this equation gives the relative intensity of the radiation as a function of frequency.

Super black materials are tremendously important for optical coatings of instruments [4] and solar energy conversion [5, 6] due to their ability to reduce unwanted reflections and absorb stray light. Carbon is an excellent absorber with an e of 0.8 – 0.85 [1] and is used in various materials to improve absorption. Scientists have made advances in this area due to the importance of obtaining super black materials. Materials such as nickel-phosphorous (Ni-P) [7], micro-structured silicon (Black-Si) [8], silicon nano-tip (SiNTs) arrays [9] and nano-fractal gold (gold black) [10], have all been fabricated. Recently, nanotubes have been placed in the forefront as an inexpensive novel material which has the lowest reflectance over a larger wavelength spectrum (UV-VIS-IR) and angles of incidence when compared to other materials. The low reflectance is due primarily to the interaction of light at the air – nanotube interface, caused by the variation in the refractive index. Large jumps in the refractive index, translates into an increase in reflection, according to Fresnel's law given by;

$$R = \frac{(n - n_0)^2}{(n + n_0)^2} \qquad 3.2$$

where n_0 is the refractive index of air (n_0 = 1.0003), n refractive index of other material (in this case CNTs) and R the reflectance. Thus when the refractive index is close to air, reflection is inhibited simply because the momentum of the incident photon is not deterred. Currently there are two methods to reduce the air – medium interface issue;

I. fabricate materials with a graded refractive index, and/or

II. find a material with a refractive index close to air.

Surface modified Ni-P, with its micrometer-sized features is one such material with a graded refractive index approach. The micro-sized cavities aid in effectively trapping photons at normal incidence, yielding a low reflectance (R = 0.16-0.18%); however, this R becomes significantly greater at larger angles (R = 4-5%) and wavelengths (R =10% at 10 μm) [1]. SiNTs arrays have low reflectance in the visible though its infrared reflectance increases linearly with wavelength [9]. Theoretical calculations for nanotubes predicted refractive index values of 1.01 -1.10 [11], due to their vertical alignment, nanometer rough surface and array spacing. These intrinsic features permit a low reflectance (R = 0.03-0.045%) [2] and an index of refraction close to that of air. While graded refractive index materials have provided decent results, difficulty arises in the fabrication methods and the cost of production is rather expensive and hazardous. For this reason, CNTs are an excellent cost effective alternative and can be grown on numerous substrates, which aligns with the goals of NASA.

Literature Review

The 1D allotrope of carbon is related to the 2D allotrope by a rolled-up vector (as discussed in Chapter 1), therefore it has been standard practice to use the optical properties of graphene to describe the optical properties of nanotubes. The research of the scientific community is presented below in chronological order beginning with such an investigation en route to the development and understanding of VA nanotubes as absorbers.

Taft E. A. *et al*.[12] (1965): *Optical properties of Graphite*

- Derived the complex dielectric constant for graphite by the application of the Kramers - Kronig relation to reflectance data in the energy range to 26 electron volts (eV).
- In the 0 to 9 eV range, the intra- and inter-band optical transitions involve mainly the π bands which arose from the one electron per atom, atomic $2p_z$ orbitals extending above and below the carbon-layer planes.

De Heer W. *et al*.[13] (1995): *Aligned carbon nanotube films: Production and optical and electronic properties*

- Developed a method to produce thin films of aligned carbon nanotubes aligned either parallel (α-aligned) or perpendicular (β-aligned) to the surface.
- Dielectric functions of the films were determined by ellipsometry. For light polarized along the tubes ($\alpha_{\parallel}$) the surface resembles graphite. For light polarized along the perpendicularly ($\alpha_{\perp}$) the dielectric function from an effective medium point of view should be a mixture of the two dielectric

functions of graphite, (parallel (ε_{grII}) and perpendicular ($\varepsilon_{gr\perp}$) to the graphite sheets).

- Raman studies of aligned cross sections revealed that comparison of the α_{II} to $\alpha_{\perp}$ direction indicated stronger effective photon-phonon coupling in the parallel direction at 1582 cm^{-1}.

Garcia-Vidal F. *et al*.[11] (1997): *Effective medium theory of the optical properties of aligned carbon nanotubes*

- Theoretical study using effective medium theory to analyze the experimental findings of DeHeer *et al*. (above).
- Developed a Maxwell-Garnett approach to study the system and demonstrated that a full electromagnetic coupling between the nanotubes is necessary for explanation.

Lu W. *et al*.[14] (2000): *Optical properties of aligned carbon nanotube systems studied by the effective-medium approximation method*

- Comparison of Maxwell-Garnett theory 2D array model and Effective-Medium approximation (EMA-Bruggeman's theory) of an aligned nanotube system based on the nanotubes described in reference [4].
- Solutions for both MGT and EMA equations yielded an effective dielectric of $\varepsilon_{eff}^{s} = f\varepsilon_{\perp} + (1-f)$ for s-polarized light, where the volume fraction (f) can be estimated by $\mathrm{Im}\varepsilon_{eff}^{s} = f'\mathrm{Im}\varepsilon_{\perp}$ (where $f' = (1-\rho^{2})f$). For p-polarized light, ε_{eff} for EMA consisted of two E-field components and for MGT one E-field component.

- The EMA theory which is valid for densely and randomly distributed particle systems explained the experimental data of reference [4] better than MGT theory.

Marinopoulos A. *et al*.[15] (2003): *Optical and Loss Spectra of Carbon Nanotubes: Depolarization Effects and Intertube Interactions*

- Calculated absorption and loss spectra for 4 Å nanotubes in both random phase and the adiabatic local density approximations.
- Local field effects induced by an external field suppresses absorption peaks rendering tubes almost transparent below 5 eV, agreeing with experimental observations.
- Intertube interactions and distances can be evaluated due to the measurability spectroscopic quantity of the $\pi + \sigma$ plasmon peak.

Murakami Y. *et al*.[16] (2005): Polarization dependence of the optical absorption of single-walled carbon nanotubes

- Presented anisotropic optical absorption properties of SWCNTs for the energy range of 0.5 to 6 eV, as determined by polarized optical absorption measurements.
- Polarization dependence of absorption peaks due to maxima at 4.5 eV ($\mathrm{Im}\{\varepsilon_{\perp}\}$ and 5.25 eV ($\mathrm{Im}\{\varepsilon_{\parallel}^{-1}\}$ related to the optical properties of graphite.
- Noted the considerable scientific disagreement for the absorption peaks at 4.5 and 5.25 eV.

- Demonstrated that the chirality dependence of the absorption in SWCNTs can be traced back to combined effects of the joint density of states and the optical matrix element.

Yang Z. *et al*.[2] (2007): *Experimental observation of an extremely dark material made by a low-density nanotube array*

- Engineered low density vertically aligned multi-walled carbon nanotube arrays to index match the vacuum, achieving low reflection.
- Ultra low diffused reflectance of 1 x 10^{-7} measured with an integrated total reflectance of 0.045% at λ = 635 nm, making it the darkest known material.
- Calculated effective index of refraction (n_{eff}) and absorption coefficient (α_{eff}) as a function of nanotube spacing as shown in Figure 3.1. At an intertube spacing (a = 50 nm) and tube diameter (d = 10 nm), for p-polarization an $n_{eff}^{p} = 1.026$ and $\alpha_{eff}^{p} = 0.12\mu m^{-1}$, thus $R_p = 0.02\%$; for s-polarization $n_{eff}^{s} = 1.074$ and $\alpha_{eff}^{s} = 2.9\mu m^{-1}$, thus $R_s = 0.60\%$.

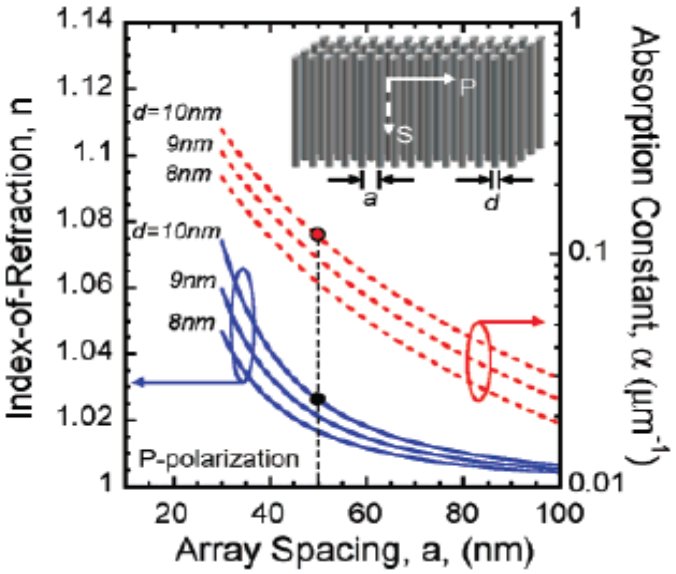

Figure 3.1.[2] Calculated effective index of refraction and the absorption constant plotted as a function of nanotube spacing. A schematic of the nanotube array and the s and p light polarizations is displayed in the inset.

Mizuno K. *et al*.[1] (2008): *A black body absorber from vertically aligned single-walled carbon nanotubes*

- Demonstrated that vertical alignment is key component to absorption of films.
- Produced SWCNT films with near constant and near-unity emissivity of 0.98-0.99 across the spectral range of 200 nm to 200 μm.

Lidorokis *et al*.[17] (2009): *Photonics with Multi-wall carbon nanotubes arrays*

- Theoretically modeled CNT-based photonic crystals (2D array model) using the finite-difference time-domain (FDTD) method, where they propose that second order Bragg scattering resonantly redirects incident light into the film so it is quickly absorbed.

- For small intertube spacing of 20 - 30 nm, obtained strong Bragg scattering and photonic band gaps in the deep UV range (25 – 35 eV). For intermediate spacing of 40 – 100 nm, the photonic bands anti-cross with the graphite plasmon bands resulting in a complex photonic structure leading to reduced Bragg scattering. For large spacing >150 nm, the Bragg gap move into the VIS and decreases due to absorption.

Lehman *et al*.[18] (2010): *Very black infrared detector from vertically aligned carbon nanotubes and electric-field poling of lithium tantalite*

- Demonstrated the practical application of water-assisted CVD grown MWCNTs as a coating on a lithium tantalite ($LiTaO_3$) pyroelectric detector. A 2 nm Fe catalyst layer on top of a 20 nm Al_2O_3 layer was used to seed tube growth.
- Observed difference in reflection of detector and witness (Si substrate) attributable to the detectors electrode metal and surface properties of $LiTaO_3$.

Bao H. *et al*.[19] (2010): *Optical properties of ordered vertical arrays of multi-walled carbon nanotubes from FDTD simulations*

- FDTD method was used to calculate the reflection, transmission and absorption properties of VA-MWCNTs, with variations in parameters such as intertube distance nanotube length and diameter, polarizations and incident wavelength. Results were compared to MGT theory.

- Absorbance at any wavelength can be fitted to $A(L) = 1e^{(-\alpha L)}$; where α is the absorption coefficient and L tube length. Also noted that good surface alignment can produce darker material.

The scientific contributions have demonstrated that the bulk of research has focused mainly on theoretical modeling of these 2D VA-nanotube arrays. The experimental research momentum has confirmed in some instances the concepts of these theoretical models, and has focused on development of practical applications utilizing this material.

The conventional approach to growth of nanotubes is the CVD method. Though the growth process is not yet fully understood, (more specifically, control of tube chirality, height and density), we are able to tune certain properties of films, i.e. tube diameter, height and density. Nessim *et al.*[20] demonstrated this tuning by controlling the timing and duration of hydrogen exposure during CVD annealing and growth. Using this scheme, we focused growing of VA- MWCNTs at GSFC as a replacement for Z306 paint, the standard blackening surface treatment for spacecraft parts, in order to reduce the inherent random photon scattering. Our goal is to be able to reproduce our film growth, with minute differences in the reflectivity/absorption, en route to growing these films on the components of telescopes thereby reducing stray photons. In our early experimental endeavors, we had a wide dispersion of the reflectance data with respect to the hydrogen exposures, as we sought optimal growth parameters. The fabrication of homogeneous films requires several key factors, as described in the literature and this chapter, which must be addressed; these factors include

the density/volume fill fraction (*v.f.f.*), tube length, intertube distance, surface roughness and incident angle.

3.2. Methods

Sample Preparation

Substrates of silicon (Si) and titanium (Ti) were cleaved and machined respectively to a dimension of 130 ± 2 square millimeters (mm^2) and cleaned via sonication in acetone followed by sonication in isopropyl alcohol and then blow dried with an air stream. After the cleaning procedure, all samples were weighed using a microbalance with an instrument error of ± 2 E-6 micrograms (μg). The weighing procedure was additionally performed after physical vapor deposition (PVD) process and CVD growth process to obtain the bulk mass of nanotubes. This method is preferred rather than scraping or etching the film from the substrate due to the negative implications of the latter procedures.

Physical Vapor Deposition

In order to fabricate thin films, a PVD 75 deposition system (Kurt J. Lesker Co. USA) was used for deposition of the alumina layer (Al_2O_3) and iron catalyst (Fe). 99.99% purity Al_2O_3 1.5 - 4 mm pieces and 99.95% purity Fe pellets with 1/8” in diameter X 1/8” in length and were purchased from Kurt J. Lesker Co. Both materials were resistively heated, permitting thermal evaporation and deposition onto silicon Si and Ti substrates. An initial Al_2O_3 layer of 60

nanometers (nm) was deposited followed by the deposition of the Fe layer with various thicknesses of 2, 4, 6, 8, and 10 nm.

Chemical Vapor Deposition

Growth runs of our vertically aligned films were performed via the CVD technique. Samples were placed into a three zone atmospheric-pressure furnace operating at a maximum temperature of 750 ^{o}C, with a fused silica tube with an internal diameter of 1 inch. The flow rates of the reactant gases used were; for Argon (Ar), 980 standard cubic centimeters (sccm), which was reduced to 410 sccm with the inclusion of water (H_2O) vapor; hydrogen (H_2) 580 sccm; and ethylene (C_2H_4) 990 sccm. During this phase of experimentation, we varied the H_2 gas flow time which consequently varied the exposure time of the heated catalyst layer. The growth time (as determined by the duration of C_2H_4 feedstock gas) remained constant at 15 minutes for multi-walled nanotube growth.

Scanning Electron Microscopy

Nanotube heights were obtained using the SEM at NASA GSFC operated at 5kV and a Raith eLine Tool operated at 10kV at Vanderbilt University. The film morphology and topography were characterized using high magnification SEM.

Raman Spectroscopy

Raman spectra of our MWCNTs were obtained with a Horiba JOBIN-YVON LabRam HR800 Raman spectrometer measured in the range of 100 cm^{-1} to 3000 cm^{-1} with the excitation of a He-Ne laser. Wavelengths of 632.8 (633) nm and 784 nm were used for sample excitation.

Hemispherical Reflectance

Optical reflectance/absorption measurements were collected with a Perkin Elmer Lambda 950 UV/VIS/NIR Spectrophotometer with an integrating sphere operated with a monochromatic light source. The standard procedure consisted of irradiating our samples with un-polarized light at an incident angle of 8^o from the surface normal over the spectral range of 200 – 2500 nm. Detection occurs through a photomultiplier tube for the UV/VIS range and a Peltier-cooled lead sulfide (PbS) detector for the NIR range. For angular dependence measurements, incident angles of 0^o and 8^o were used with a polarized and un-polarized source. Baseline corrections were performed using a barium sulfate reference sample with a calibration to a NIST standard prior to experimentation.

3.3. Growth of Vertically Aligned MWCNTs

We investigated the effects of H_2 exposure time on the structure of the nanotubes, including effects on the tube diameter, intertube distance/spacing, density and tube length. MWCNTs, which are metallic, were more desirable for experimentation due to their larger size and uniform optical properties. SWCNTs

contain an array of numerous chiralities with random distributions. Their strong chiral dependence affects its optical properties as a result of the variations in nanotubes types and diameter. Theoretical descriptions [11, 19] of the optical properties of CNTs, depends on the *v. f. f.* which is a the ratio of our calculated sample densities to the density of graphite, 2.2 g cm^{-3}. The aperiodic intertube distances and variations in tube diameters allow us to treat our films as a porous homogeneous medium. To realize low reflectance and high absorbance from our nanotubes, a low *v .f. f., i.e., a* successively lower density and longer tubes are favorable.

The CVD technique is a widely accepted method for nanotube growth, which includes two phases of growth during CVD;

i. the formation and reduction of the Fe catalyst

ii. the nucleation and growth of the CNTs on the catalyst particles. Important growth parameters include catalyst thickness, reactant temperature, reactant time, gas flow rates and growth time.

Figure 3.2 shows the CVD furnace and sample positions in (a) and in (b) the growth steps of the MWCNTs. Figure 3.3 shows the thermal profile used for our CVD growth treatment. Initially the furnace temperature is ramped at a heating rate of 37.5 ^{o}C/minute followed by an annealing step. Once our annealing step has been completed, the growth is initiated for a set time period, and then terminated as the furnace is cooled.

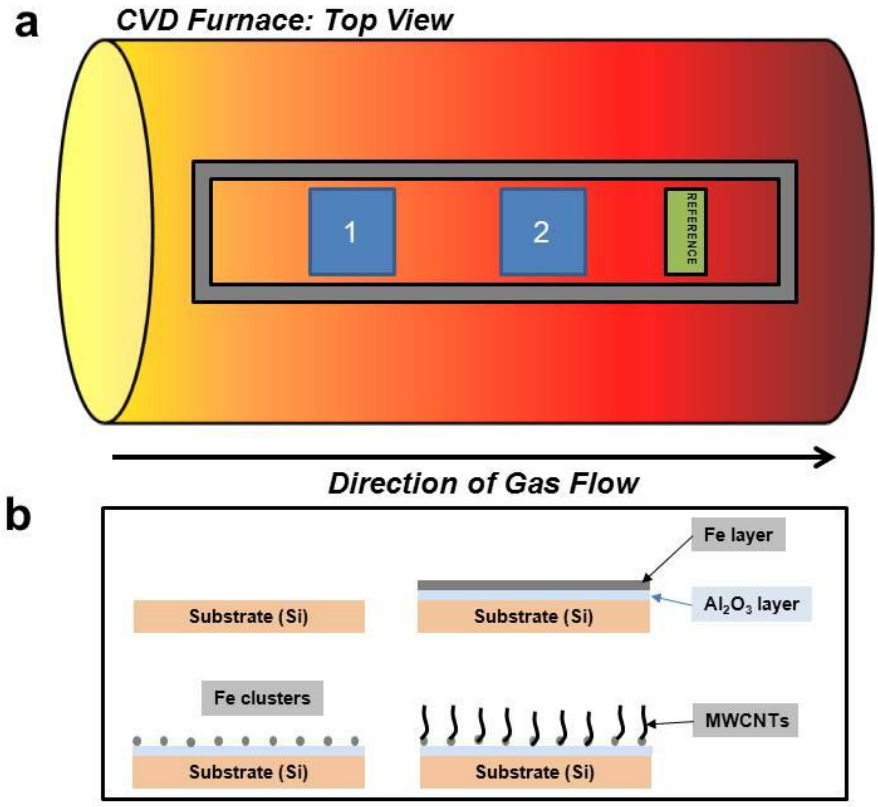

Figure 3.2. Sketch of (a) CVD furnace at zone 2 (center of furnace) and the location of samples with respect to the directional flow of gases (Ar, Ar/H_2O, H_2 and C_2H_4). The green colored sample is a reference (with only a 5 nm Fe layer) sample present in all growth runs (b) Growth steps of MWCNTs by the CVD method.

During the initial temperature ramp, the Fe layer melts and forms clusters which act as seeds for nanotube growth and contribute to nanotube diameters. In the annealing phase we varied the H_2 exposure time of the Fe catalyst with the H_2 acting as a vapor etchant which reduces the oxidation of the Fe catalyst prior to nucleation and growth. Further, H_2 reduces gas phase pyrolysis of the hydrocarbons causing desorption of amorphous carbon (*a*-C) fragments from the catalyst surface [20]. This step is critical in maintaining the balance between the

formation of *a*-C and crystalline CNTs. The introduction of the carbon precursor, C_2H_4, enables crystalline tube orientation during the growth phase. The introduction of H_2O vapor increases the catalyst lifetime and thereby extends the lifetime of the growth process. Recent studies [21-23] showed that the diameters and wall count can be controlled by varying the metal catalyst thickness. To maintain experimental control, we included a witness sample in all CVD growth runs, with a 5 nm layer of Fe deposited onto a Si substrate. It was anticipated that a smaller Fe layer thickness will produce longer vertically aligned nanotubes.

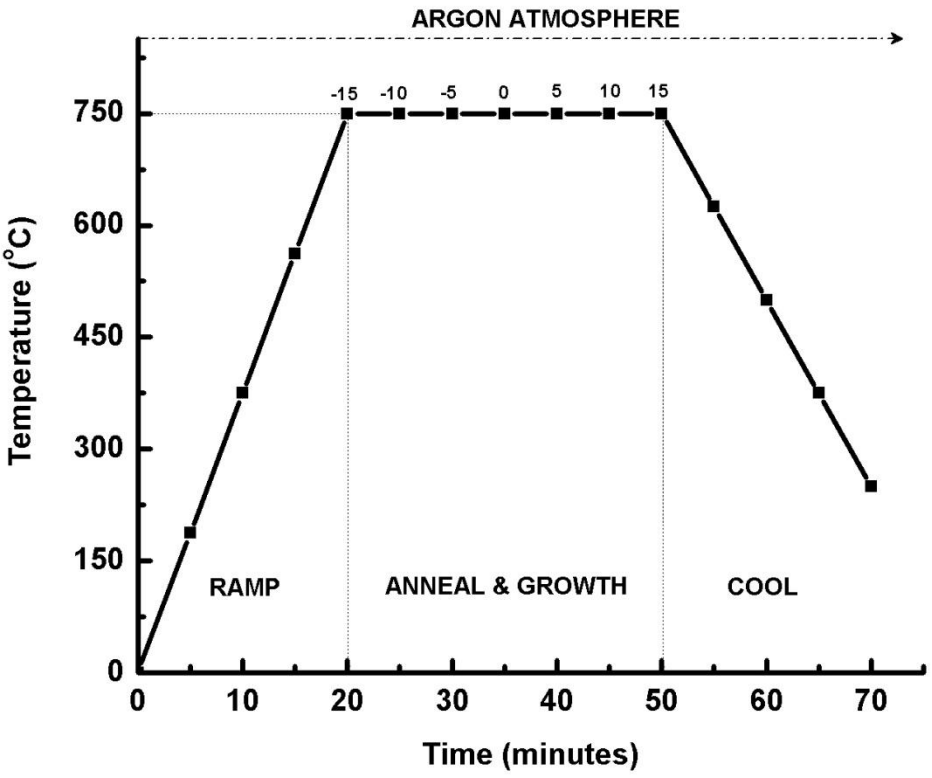

Figure 3.3. Thermal profile used for CVD growth of multi-walled carbon nanotubes where the variable is the H_2 exposure time (flow rate of 580 sccm) relative to the introduction of C_2H_4 with a flow rate of 990 sccm. The carrier gas is dry Ar with a flow rate of 980 sccm (without H_2O vapor) and wet Ar at 410 sccm (with H_2O vapor).

Table 3.1. H_2 exposure times and growth results. The H_2 exposure times are explained as followed; (*i*) t-15 – H_2 introduced 15 minutes prior to introduction of C_2H_4 (*ii*) t=0 – simultaneous introduction of H_2 and C_2H_4 (*iii*) t+10 – H_2 introduced 10 minutes after introduction of C_2H_4. The introduction of C_2H_4 is the start of the growth phase.

H_2 Exposure Times (min)	**t-15**	**t-10**	**t-5**	**t=0**	**t+5**	**t+10**
Results of Growth Trials	Growth	Growth	Growth	Growth*	1. Growth 2. No growth	No Growth

*Initial trials on the Si substrate yielded a large height variation as shown in Appendix B.

Table 3.1 shows the H_2 exposures we attempted for the deposited Fe catalyst and the results of whether those investigations yielded growth of CNTs. With an increased H_2 exposure time, we were able to grow homogeneous vertically aligned CNTs. Nessim *et. al.* and references therein [20], demonstrated that an increase of exposure time leads to catalyst coarsening. The coarsening results in the transport of Fe via vapor phase or diffusion of Fe adatoms on the Al_2O_3 surface. Thus the masses of initial small clusters are redistributed to larger clusters, resulting in increased cluster size and spacing. When the H_2 exposure was performed after C_2H_4 was introduced, growth of nanotubes gave poor results. Knowing that the thermal decomposition of C_2H_4 forms H_2 and various hydrocarbons (CH_4, C_2H_6) [20], slower Fe reduction and coarsening occurs. Accordingly the limit shown for the times *t +5* min and *t +10* min, is expected as the growth of crystalline MWCNTs has been impeded. The *t = 0* exposure time which included the simultaneous introduction of H_2, H_2O and C_2H_4 reactant gases yielded growth, however the heights and growth rates of the CNTs were less than those grown with the *t -5* H_2 exposure time [Appendix B discusses our

results and how we arrived at this conclusion]. Additionally it was reasoned [20] that the CNT diameters increase with increased H_2 exposure time, hence the importance of the H_2 exposures for our investigation.

Based on our results in Appendix B, we selected the *t -5* H_2 exposure times to conduct nanotube growths on Si substrates due to its steady growth profile and previous reflectance performance [4]. To ensure that the t -5 exposure time was optimal, we increased the H_2 exposure times to *t -10* and *t -15*. For these additional exposure times, we explored the effect of catalyst thickness on our films reflection.

Figure 3.4 shows the bulk mass in micrograms (μg) of the carbon content (nanotubes, amorphous carbon, and graphitic carbon) for our respective catalyst thicknesses as a function of the H_2 exposure times. The Al_2O_3 and Fe layers were deposited successively under the same vacuum conditions, ensuring the accuracy of our carbon mass measurements by microbalance, less that of the Fe and Al_2O_3 layers. The masses of the *t -15* and *t -10* exposure times show no trend as a function of Fe layer thickness as compared to the *t -5* exposure time, which shows a linear trend for the mass as the catalyst layer increases. As previously discussed, increased exposure time leads to coarsening and a slower growth rate [20]. Larger Fe clusters, accumulating more C atoms, form larger diameter MWCNT with an increased count of inner tubes. As such, the increase in mass of the *t -10* and *t -15* samples are expected. In the case of the *t -10* 2 nm samples, the high mass count may be the result of;

i. submergence of Fe clusters into the Al_2O_3 underlayer thereby causing the agglomeration of C atoms into a-C and CNTs.

ii. agglomeration of C atoms in addition to non-uniformity of surface coverage.

iii. an effect of prolonged oxidation of the catalyst. However, comparisons of CVD growths were performed on new and old catalysts layers and showed no effects.

iv. position of the samples, as the 2_3 nm (74 μg) and 2_4 nm (9091 μg) samples were in positions 1 and 2 (Figure. 3.2) respectively.

Figure 3.5 shows SEM images of both *t -10* 2 nm (2_3 and 2_4) samples, which demonstrate point *i* above.

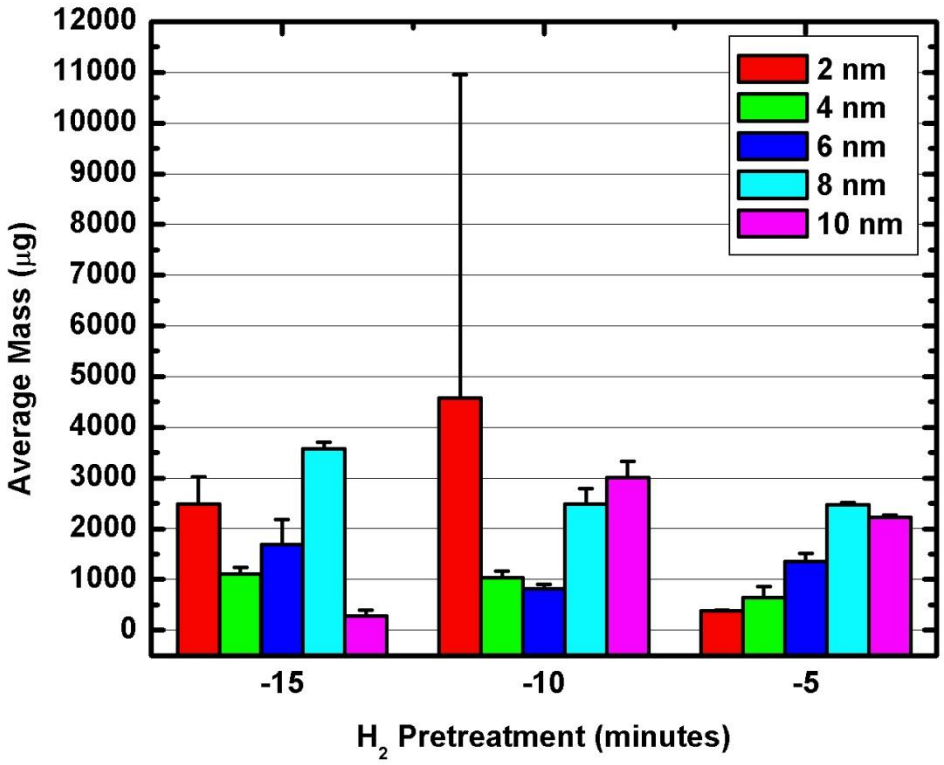

Figure 3.4. Mass of carbon for respective Fe catalyst layers for the *t -15*, *t -10* and *t -5* H_2 exposure times. The masses of the *t -15* and *t -10* exposure times are relatively inconsistent. The *t -5* H_2 exposure time shows a linear trend for the mass as the catalyst layer increases.

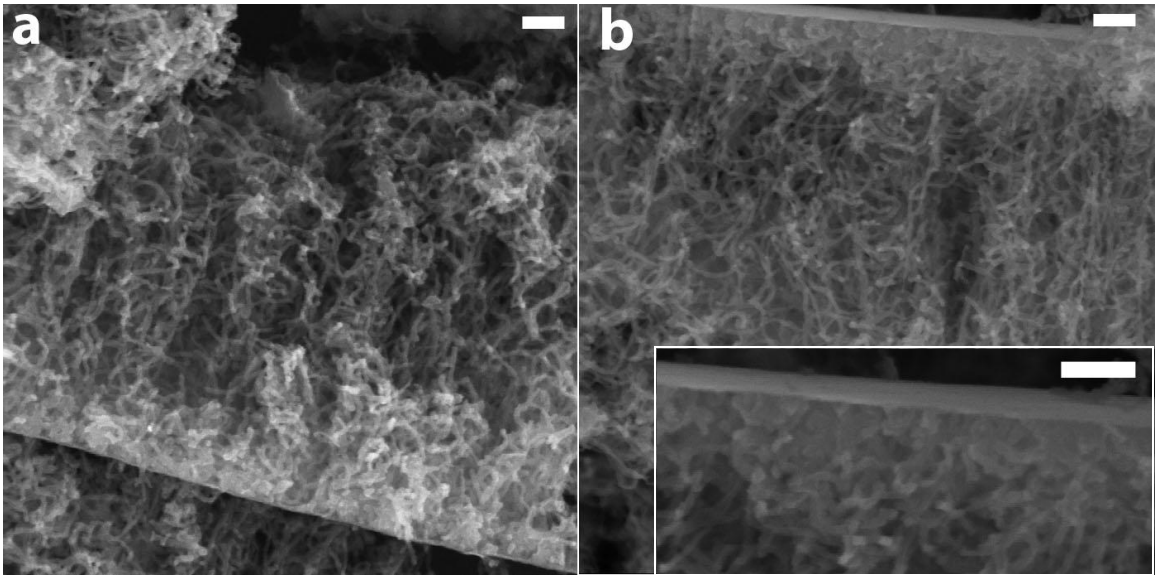

Figure 3.5. SEM images of 2_3 nm (a) and 2_4 nm (b) samples displaying growth of nanotubes with the agglomeration of C atoms at the Al_2O_3 surface. The inset in (b) shows a higher magnification of this occurrence. The scale bars in the images are 200 nm.

The heights of our nanotubes were measured using scanning electron microscopy (SEM). Figure 3.6 displays the averaged heights of nanotubes as a function of the H_2 exposure times. For the *t -5* exposure, the nanotube heights are approximately similar in value within error. The *t -10* exposures show a linear trend in height. The *t -15* 2 nm samples yielded nanotubes with the longest lengths measured in our experiments, though this phenomenon did not translate over other Fe layer thicknesses of the same exposure. The growth rates of the nanotubes are initially rapid, with the presence of the H_2O vapor, a weak oxidizer, they are etched during the growth process. This may explain the relative similarity in heights for our *t -5* samples. Accounting for the effects of prolonged H_2 exposure on the Fe catalyst [20], the inconsistency of growth may explain our *t -10* and *t -15* samples. Further we postulate that due to the effect of

CNT length on absorption, for which longer tubes have a higher absorbance [11, 19], the performance of the *t -15* exposures over *t -5* and *t -10* exposures ought to improve. We will discuss a method of accomplishing this below.

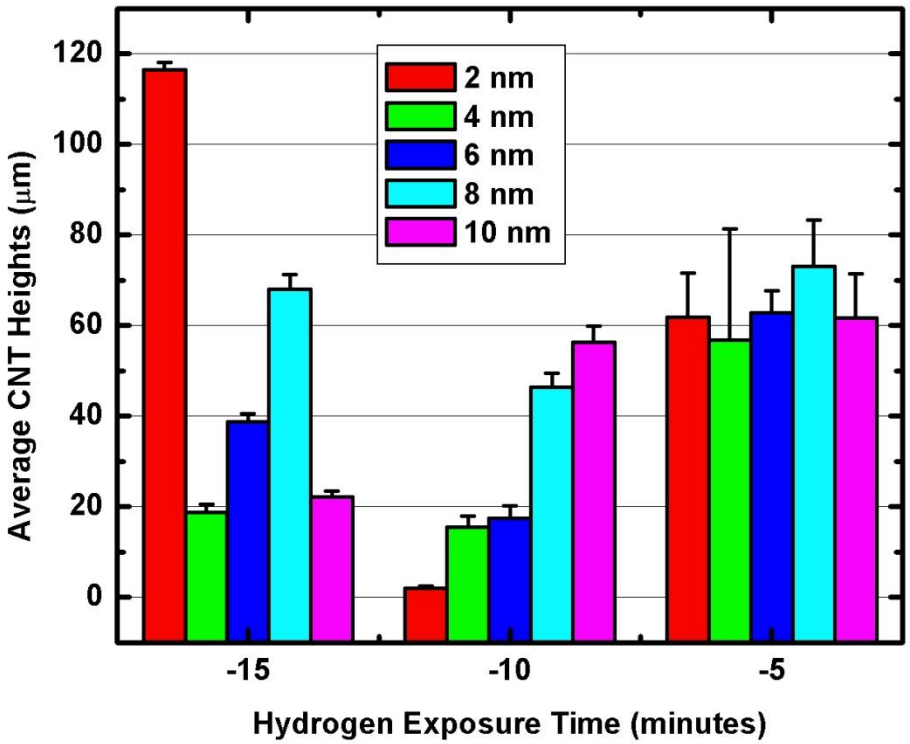

Figure 3.6. Heights of nanotubes (averaged) as measured by SEM for *t -5*, *t -10* and *t -15* H_2 exposure times. *t -5* heights are approximately the same within error, *t -10* heights have a linear trend and *t -15* show no trend.

From our bulk mass and height measurements, we calculated the bulk density of our nanotubes with respect to the catalyst thickness based on the following equation;

$$\rho_B = \frac{M}{(A * h)} \qquad 3.3$$

where ρ_B is the bulk density in units of grams per cubic centimeters (g cm^{-3}), *M* the mass of the carbon nanotubes in units of micrograms (μg), *A* the cross-sectional area in units of square millimeters (mm^2) and *h* the height in units of micrometers (μm). Figure 3.7 shows our bulk density calculations. Our samples are porous in nature; the ρ_B takes into account the mass of the material which includes the volume of the pores or void spaces (intertube spacing or periodicity). The void spaces are crucial for improving the absorptive properties of nanotubes [1, 2, 11, 13, 19]. The H_2 exposures we employed in our experimentation was a method for controlling the diameters [20]. Now that we have a representation of the density we sought to correlate it to measured reflectance. A plot of the reflectance (%R) as a function of bulk density would be expected to yield a linear relationship based on equation 3.2. Figure 3.8 shows the %R density relationship for our samples. The linear relationship is absent due to the 4nm outlier for the *t -5* exposure time. We found that our 4nm samples were contaminated as shown in Figure 3.9, which resulted in higher %R values. The striations shown in the figure appear as regions of less growth.

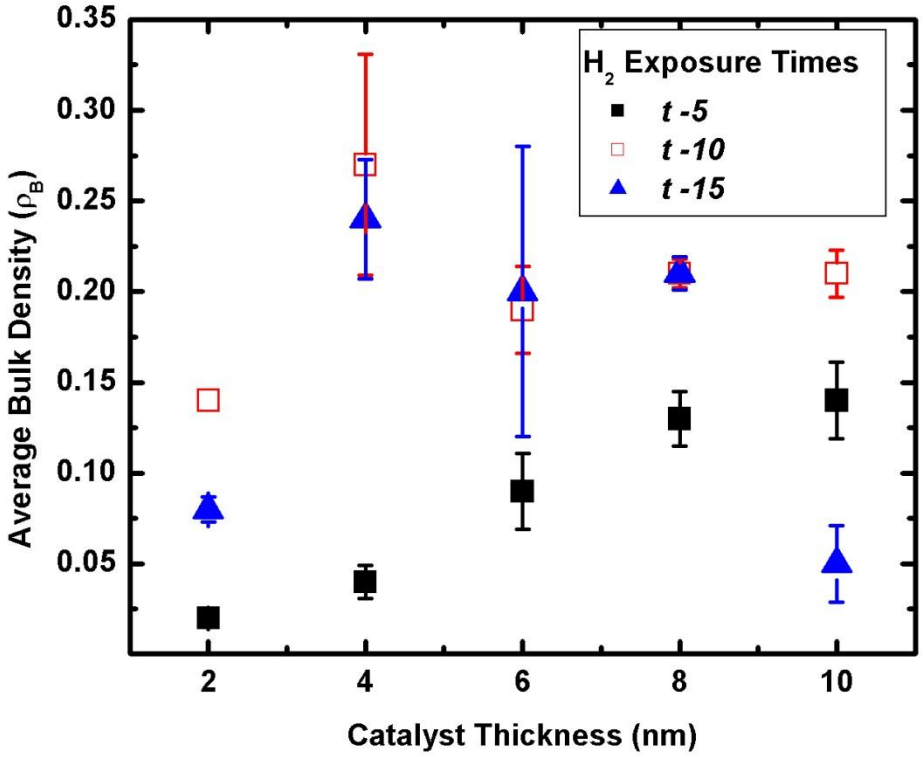

Figure 3.7. Average bulk density (ρ_B) of nanotubes as a function of the catalyst thicknesses for *t -5*, *t -10* and *t -15* H_2 exposure times. The bulk density of the *t -5* exposure time is relatively linear with an R^2 value of 0.98.

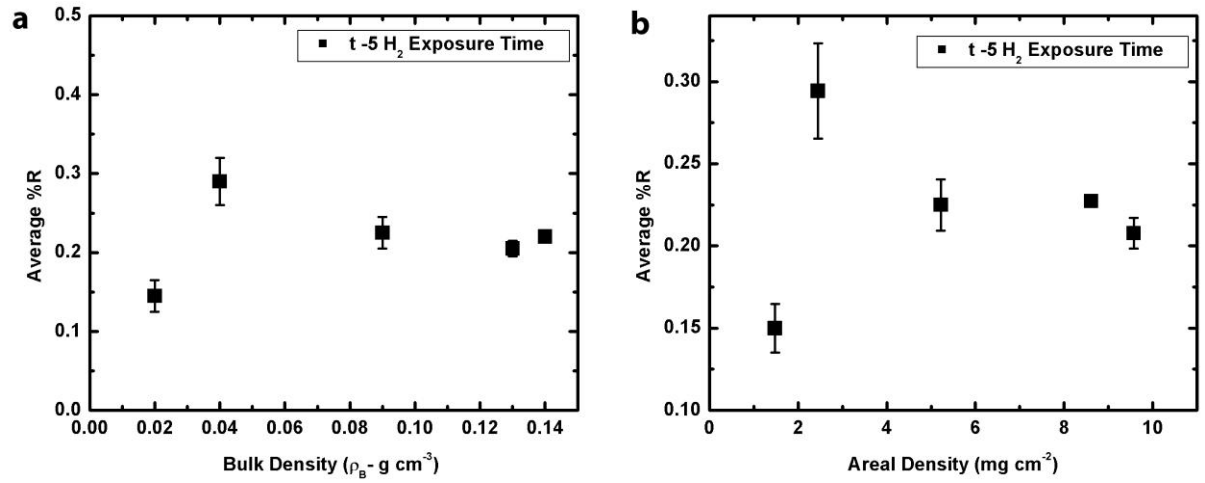

Figure 3.8. Relationship between reflectance (%R) and (a) bulk density and (b) areal density for our samples.

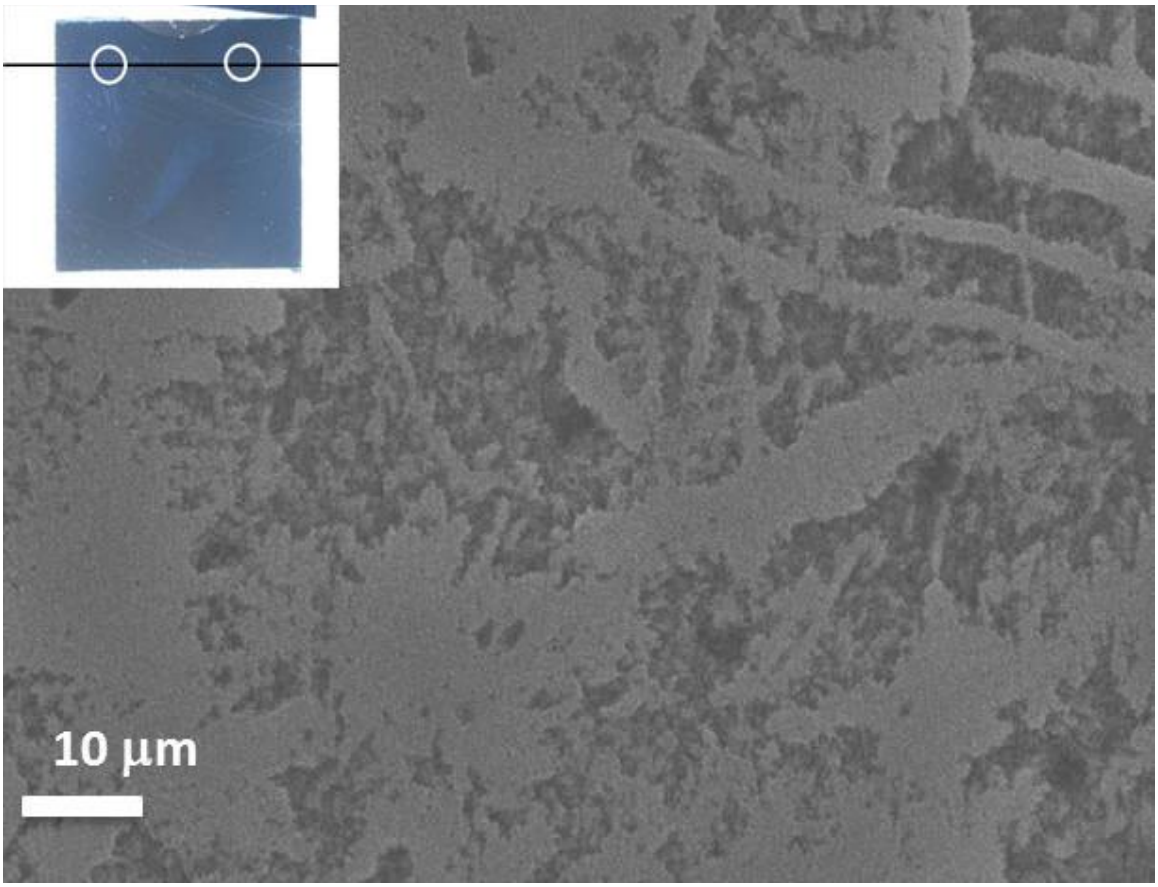

Figure 3.9. SEM image of contaminated 4nm sample. The striations shown in the inset caused regions of non-uniform growth, resulting in higher %R values.

Table 3.2 is a summary of the sample identifications (ID), iron (Fe) layer thickness, hydrogen exposure times, bulk mass, measured nanotube heights, calculated bulk densities and Average %R values. The %R values were averaged over the wavelength range of 750 nm – 2500 nm, with an average of 1625 nm. Discussion and significance of these values are in the following section.

Table 3.2. Sample identifications (ID), iron (Fe) layer thickness, hydrogen exposure times, bulk mass, measured nanotube heights, calculated bulk densities and Average %R values.

Sample ID	Fe Layer (nm)	H_2 Exposure	M (μg)	height (μm)	ρ_B (g cm^{-3})	Average % R
Silicon 2_1	2	*t -5*	395	70.57	0.02	0.1604 ± 0.0500
Silicon 2_2	2	*t -5*	365	53.04	0.03	0.1395 ± 0.0501
Silicon 4_1	4	*t -5*	478	51.3	0.04	0.3147 ± 0.0598
Silicon 4_2	4	*t -5*	790	62.3	0.05	0.2738 ± 0.0496
Silicon 6_1	6	*t -5*	1243	47.36	0.10	0.2360 ± 0.0699
Silicon 6_2	6	*t -5*	1460	78.02	0.07	0.2139 ± 0.0720
Silicon 8_1	8	*t -5*	2502	67.96	0.14	0.2011 ± 0.0445
Silicon 8_2	8	*t -5*	2456	78.02	0.12	0.2144 ± 0.0576
Silicon 10_1	10	*t -5*	2202	54.45	0.16	0.2273 ± 0.0642
Silicon 10_2	10	*t -5*	2257	68.96	0.13	0.7507 ± 0.0836

Sample ID	Fe Layer (nm)	H_2 Exposure	M (μg)	height (μm)	ρ_B (g cm^{-3})	Average % R
Silicon 2_3	2	*t -10*	74	2.07	0.14	0.7379 ± 0.0779
Silicon 2_4	2	*t -10*	9091	2.02	17.65	0.5510 ± 0.0993
Silicon 4_7	4	*t -10*	1128	19.59	0.23	0.4045 ± 0.1002
Silicon 4_8	4	*t -10*	926	11.45	0.31	0.4500 ± 0.1231
Silicon 6_6	6	*t -10*	878	20.11	0.17	0.4496 ± 0.0985
Silicon 6_7	6	*t -10*	758	14.67	0.20	0.3958 ± 0.1157
Silicon 8_3	8	*t -10*	2262	43.48	0.20	0.3943 ± 0.0791
Silicon 8_4	8	*t -10*	2699	49.43	0.21	0.3816 ± 0.0651
Silicon 10_4	10	*t -10*	2788	54.1	0.20	0.4290 ± 0.1100
Silicon 10_5	10	*t -10*	3235	58.5	0.22	0.3904 ± 0.0762

Sample ID	Fe Layer (nm)	H_2 Exposure	M (μg)	height (μm)	ρ_B (g cm^{-3})	Average % R
Silicon 2_5	2	*t -15*	2118	105.2	0.08	0.2749 ± 0.0770
Silicon 2_6	2	*t -15*	2870	127.7	0.09	0.3036 ± 0.0879
Silicon 4_5	4	*t -15*	1202	22	0.21	0.3756 ± 0.0879
Silicon 4_6	4	*t -15*	1020	15.4	0.26	0.4053 ± 0.1084
Silicon 6_4	6	*t -15*	2037	56.7	0.14	0.4106 ± 0.0796
Silicon 6_5	6	*t -15*	1348	20.67	0.25	0.4671 ± 0.1070
Silicon 8_6	8	*t -15*	3490	67.8	0.20	0.4472 ± 0.0806
Silicon 8_7	8	*t -15*	3668	68.24	0.21	0.3816 ± 0.0738
Silicon 10_5	10	*t -15*	360	21.4	0.06	0.3656 ± 0.0639
Silicon 10_7	10	*t -15*	208	22.96	0.04	0.3510 ± 0.0706

3.4. Raman Spectroscopy

The evaluation of our nanotube purity, tube alignment and defect density is crucial in the ability to have reproducibility of obtaining vertically aligned nanotubes. The Raman measurements were performed at Fisk University by Yulong Cui PhD. in Professor Arnold Burger's group.

The Raman shift spectra for the *t -5* samples are shown in Figure 3.10 for varying catalyst thicknesses. We observe for our samples the presence of the radial breathing mode (RBM), D -band, G -band and G' -bands. The RBM for MWCNTs has been related to the narrow innermost tubes [24] as well as the presence of defects and the presence of iron catalyst[25, 26]. The D -band (1318 - 1321 cm^{-1}) is assigned to the presence of disorder in graphitic materials. The G -band (1577 – 1585 cm-1) corresponds to the tangential vibrations of the hexagonally bonded carbon atoms. The G'- band (D* or 2D) is a second – order harmonic of the D mode and is indicative of long range order in samples due to two-phonon, second-order scattering process that results in the creation of inelastic phonons [18]. The G'-band can be utilized to assess the purity of MWCNTs due to the unreliability of I_D/I_G interpretation which stems from the effects of carbon impurities on these intensities. The G' –band peak has been shown to be a more accurate alternative for measuring quality and purity[27].

Additionally, disorder can be examined using the G –band peak dispersion over multiple wavelengths. The G peak dispersion is given by the following equation[28];

$$G_d\left(\frac{cm^{-1}}{nm}\right)=\frac{I(G)_{633}-I(G)_{784}}{(784-633)} \qquad 3.4$$

where I_G is the intensity of the G –band peaks for the 633 and 784 nm wavelengths. The G –band peak has high dispersions in more disordered carbons where the dispersion is proportional to the degree of disorder. Figure 3.11 shows the linear relationship of the G_d (*G* dispersion) as a function of the catalyst thickness. Since the G_d increases with more disorder we anticipate that our 2 nm *t -5* samples will have improved absorption capabilities over the other Fe catalyst layer thicknesses. This finding is confirmed below in the following section. We also note the I_D/I_G ratio, which exhibits a negative slope and supports the hypothesis that the 2 nm samples will give high performance. These examinations based on Raman data confirm the effects of impurities on our samples. Defects such as amorphous carbon (*a*-C), surface defects (adatoms, vacancies) and the influence of pentagon and heptagon structural defects which cause helical nanotube formation on the sp^2 hexagonal lattice[18] affect sample homogeneity and thus the absorbance properties. The theoretical models are based on solid and hollow cylinders [11, 14, 16, 19]; as shown in Figure 3.11 the nanotubes grown confirms their helical structure. Examination of the helical angles result in angles of 28^o, 33^o, 44^o and 45^o, which is consistent with the finding in the literature [18]. Due to the anisotropic nature of nanotubes, the polarization dependence will be altered for helical tubes.

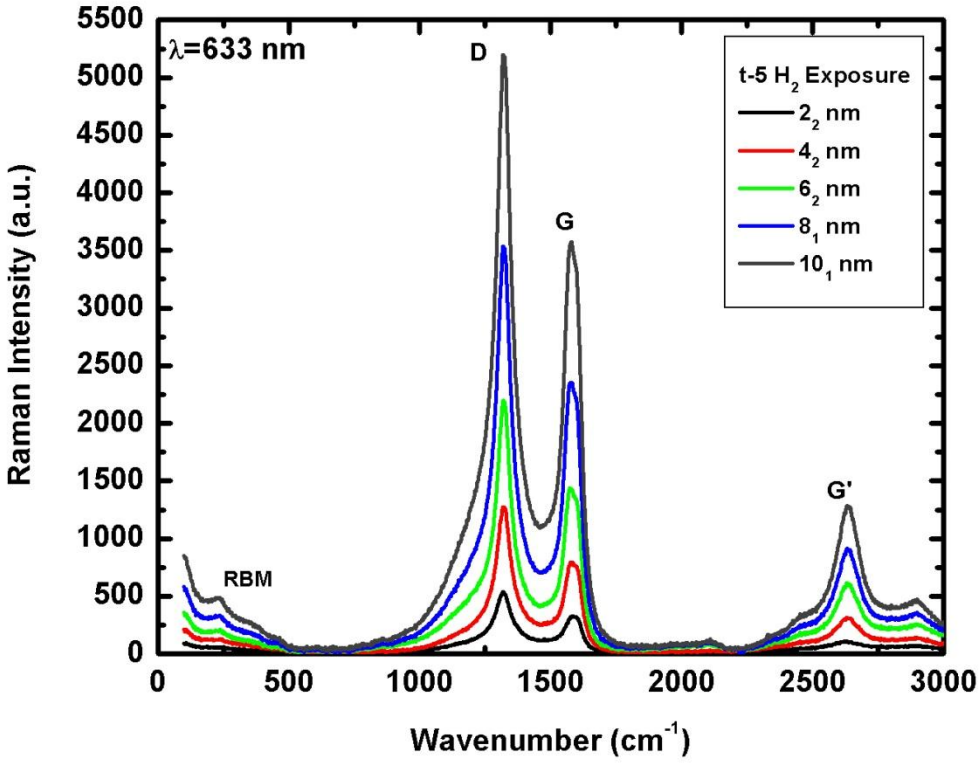

Figure 3.10. Raman shift spectra for *t -5* H_2 exposure time. The radial breathing mode (RBM) is present for some of our samples and is located in the range of 230 – 235 $cm^{-1}$and is typically used to calculate the diameter of single-walled CNTs. In addition we observe the presence of the D, G and G' –band peaks with intensities in the range of ~1318-1321 cm^{-1}, 1577-1585 cm^{-1} and 2600 cm^{-1} , respectively. Laser beam diameter and power were 2 μm and 13 mW respectively.

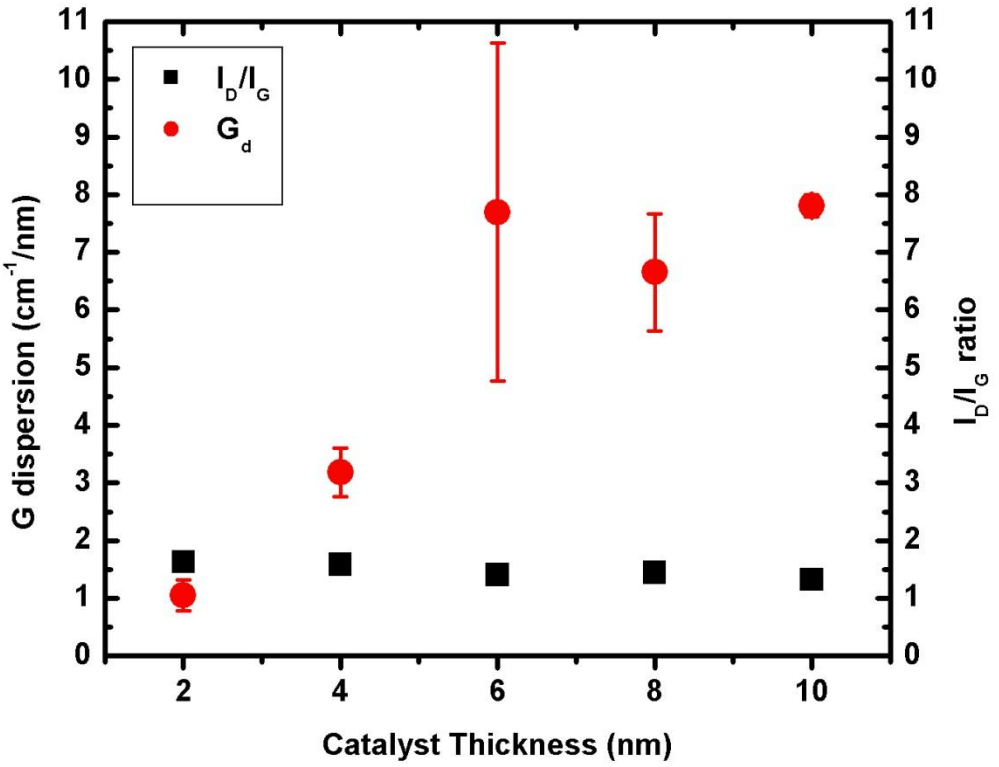

Figure 3.11. The *G* dispersion (G_d) and I_D/I_G ratio for the *t -5* H_2 exposure time. The 2 nm sample exhibits lower impurity defects.

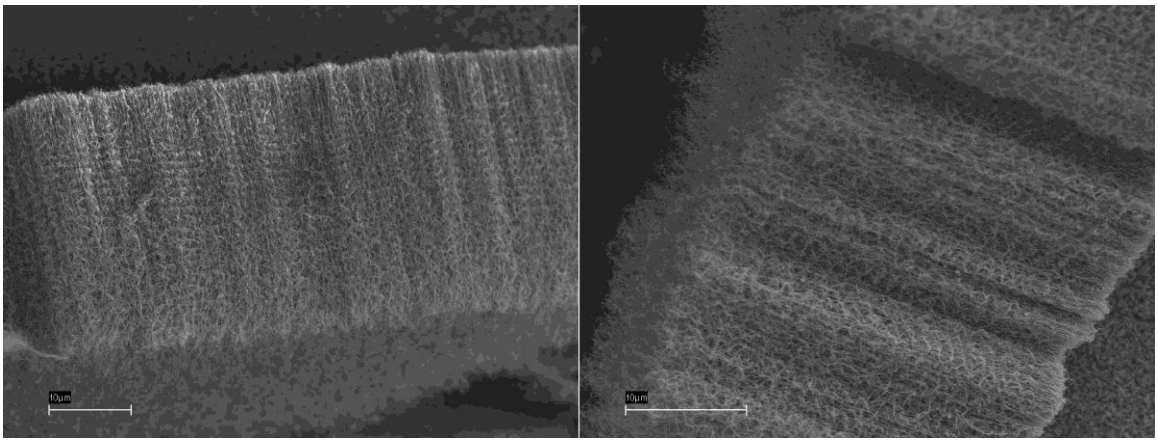

Figure 3.12. SEM images showing the helical nature of our nanotubes.

3.5. Optical Absorption and Reflectance as Indicators of Performance

We used hemispherical reflectance (HR) to quantify the absorption performance of our nanotubes grown with *t -5*, *t -10* and *t -15* H_2 exposure times as shown in Figures 3.13, 3.14 and 3.15, respectively. The *t -5* exposure samples, overall have the best performing percent reflectance (%R) and thus the best absorptive properties. For the sample set, the %R values remains below 0.25% (R = 0.0025) from λ = 1250 nm. The 4_2 and 8_1 nm samples exhibit a linear increase of %R, wavelength (λ)-dependence, as λ increases. We will investigate this observance further below. Our %R for the 2_2 nm sample is the lowest acquired for our data shown in Figure 3.13.b as well as in Table 3.2. We sought to compare our 2 nm samples as they gave the best performance, with the exception of the *t -10* samples. Comparison of the 2 nm %R values for the *t -5*, *t -10* and *t -15* exposure times yielded values of 0.1395 ± 0.0501, 0.5510 ± 0.0993 and 0.2749 ± 0.0770, respectively. While the 2_5 nm sample has considerably longer CNTs, its HR performance is 2 times poorer than the 2_2 nm sample. Considering its height and density, the nanotubes are 2 times longer, while the density is ~3.4 times greater than our best performers. We suggest that these factors affects the surface roughness, longer tubes exhibit increased irregularity at the air-nanotube interface and intertube spacing which is critical for effective photon trapping.

Examination of the 2_4 nm sample by SEM (Figure 3.9), which has the shortest CNTs measured, explains its poor performance. Further, the extremely high density is a result of a-C present in our samples which increased the

reflectance and caused λ-dependence. As a final point, the nanotube heights and alignment are important factors that contribute to higher absorbance[1] allowing reflection from the bottom surface to become weaker [19].

From our averaged %R data we calculated the emissivity of our samples. Ideally, the emissivity should be wavelength (λ)-independent and unity across a large spectral range. For our case we are observing the near IR spectrum from 750 to 2500 nm (1625 nm - averaged value). As photons interact with the nanotubes, several mechanisms such as reflection (*R*), transmission (*T*) and absorption (*A*) transpires simultaneously. The sum of these three optical mechanism components is given by,

$$R + T + A = 1 \qquad 3.5.$$

As shown, our material is highly absorptive which means we can assume that the transmission component is accordingly minor, effectively negligible (0). Furthermore from Kirchhoff's radiation law we find that;

$$e_\lambda = \alpha_\lambda \qquad 3.6$$

where e_λ is the emission coefficient or emissivity and α_λ is the absorption coefficient or absorptivity. It states that the emissivity of an object is equal to the absorptivity and thus the absorptivity is equal to one in thermal equilibrium. Setting $T = 0$ and substituting $e_\lambda = A$, from equations 3.5 and 3.6 respectively, we obtain the equation to calculate our emissivity;

$$e_\lambda = 1 - R \qquad 3.7.$$

We calculated the emissivity of our *t -5* and *t -15* 2 nm samples as they had the lowest %R values in our experimentation. We obtained values of 0.9984,

0.9986, 0.9973 and 0.9970 for 2_1, 2_2, 2_5 and 2_6, respectively which are fairly close to 1 and demonstrate the relative closeness of nanotubes to being a blackbody.

UV Peak at 275 nm

Our analysis thus far has focused on the near IR spectrum. We now focus on the UV spectrum (200 – 400 nm), more specifically, the UV peaks located at ~275 nm (~4.5 eV). These peaks originate from the optical properties of graphite. As previously stated, graphite is birefringent, thus its dielectric function consists of two components, the ε_o and ε_e, which correspond to ordinary and extraordinary rays in that order (hence CNTs are birefringent and anisotropic). .As a nanotube forms the 1D structure from 2D graphene by the rolling vector, the nanoscale diameter causes quantization of the circumferential wave vectors, creating strong divergences in the electronic density of states (Van Hove singularities) which formulate discrete energy levels or sub-bands [29]. The presence of this peak has been shown to be polarization dependent [11] and consistent with reports for both random and aligned SWCNTs and MWCNTs [16]. The peak is attributed to several factors that include π plasmon (4.2-4.5 eV) surface and bulk π plasmon excitations (5.2 eV), π plasmon along tube axis, and pristine samples containing a-C (5.2 eV).

Additional information, such as a quantitative index for nanotube alignment, intertube spacing and *v.f.f.* (both relate to density), relating our samples to ε_o and ε_e of graphite, can be extracted for a range of λ. Two theoretical approaches have been widely used to translate the properties of

graphite onto nanotubes, the Maxwell-Garnett (MG) approximation [11] and effective medium theory (EMT) [14], to calculate the effective dielectric constants of nanotubes (ε_{eff}). However, the EMT was found to more closely fit experimental data. In order to comprehend ε_{eff}, we first acknowledge that our material is homogeneous and electromagnetic radiation affects its permittivity. From Maxwell's equations, we have

$$D = \varepsilon_{fp} E + P \qquad 3.8$$

where *D* is the electric displacement, ε_{fp} the permittivity of free space, *E* the electric field and *P* the polarization field. The polarization field, P, is given by;

$$P = \varepsilon_{fp} \chi E \qquad 3.9$$

where χ is the electric susceptibility. Then by combining equations 3.8 and 3.9, we obtain the expression;

$$D = \varepsilon_{fp} E + \varepsilon_{fp} \chi E = \varepsilon_{fp}(1+\chi)E = \varepsilon_r \varepsilon_{fp} = \varepsilon \qquad 3.10$$

where ε_r is the relative permittivity.

For nanotubes the ε_{eff} is given by the following equations for p- and s-polarizations respectively;

$$\varepsilon_{eff} = \varepsilon_2 + \frac{f\varepsilon_2(\varepsilon_1 - \varepsilon_2)}{\varepsilon_2 + L(\varepsilon_1 - \varepsilon_2) - fL(\varepsilon_1 - \varepsilon_2)} \text{ (MG)} \qquad 3.11$$

$$f\frac{(\varepsilon_1 - \varepsilon_{eff})}{\varepsilon_{eff} + L(\varepsilon_1 - \varepsilon_{eff})} + (1-f)\frac{(\varepsilon_2 - \varepsilon_{eff})}{\varepsilon_{eff} + L(\varepsilon_2 - \varepsilon_{eff})} = 0 \text{ (EMT)} \qquad 3.12$$

$$\varepsilon^{s}_{eff} = f\varepsilon_{\perp} + (1-f) \text{ (MG \& EMT, s- polarization)} \qquad 3.13$$

where ε_1 is $\sqrt{\varepsilon_o \varepsilon_e}$ for p- polarization, ε_o for s- polarization, ε_2 the dielectric constant of air, *L* is the depolarization factor (for p=1/2, and for s= 0) and *f* the *v.f.f.*

Thus far, for our UV peaks, we can conclude that the reflectance values of our best performers (Figures 3.13.a and 3.15.a **–** 2 nm samples) correspond to a lower density and lower reflectance. In Figure 3.14.a**,** the 2 nm sample peak is also low this is why further analysis is necessary. In order to fully obtain quantitative information we chose to perform the Kramers-Kronig relation analysis on our %R data for select samples (Chapter 4).

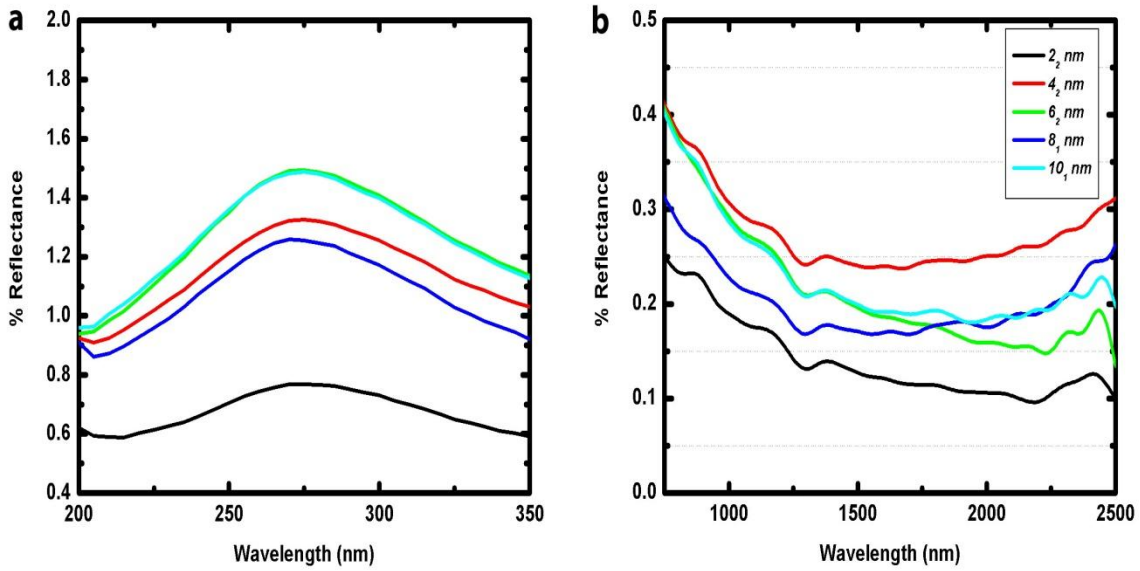

Figure 3.13. (a) Shows the peak located at 275 nm (4.5 eV) in the ultraviolet spectrum (UV). (b) Measured hemispherical reflectance of *t -5* exposure time (lowest averaged reflectance showed these as our best samples) for the near infrared (IR) spectrum.

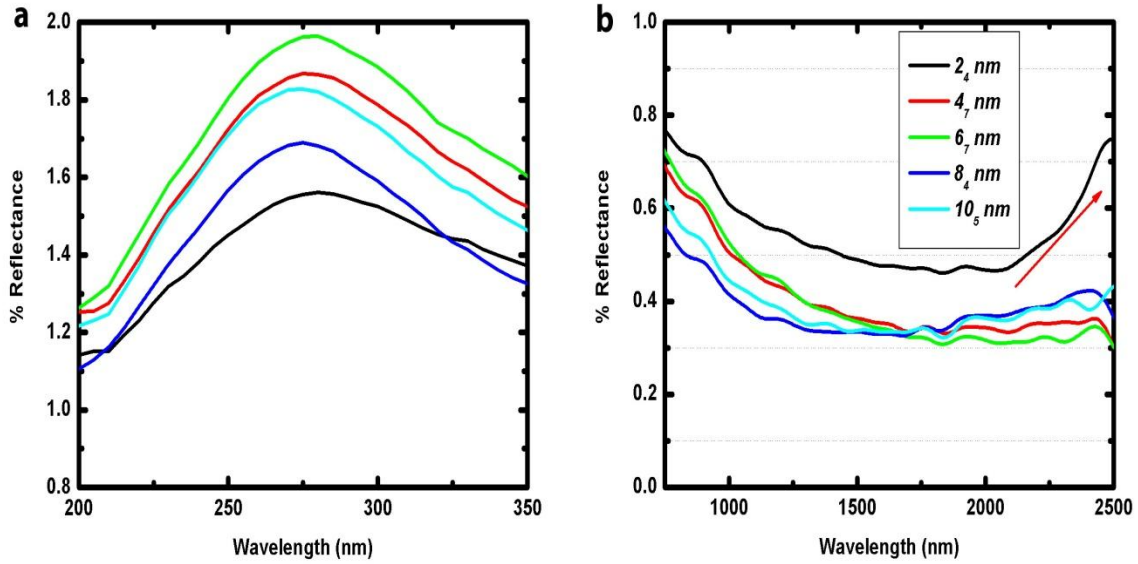

Figure 3.14. (a) Shows the peak located at 275 nm (4.5 eV) in the ultraviolet spectrum (UV). (b) Measured hemispherical reflectance of *t -10* exposure time (best performing samples) for the near infrared (IR) spectrum. The 2_4 nm sample shows the onset of λ -dependence.

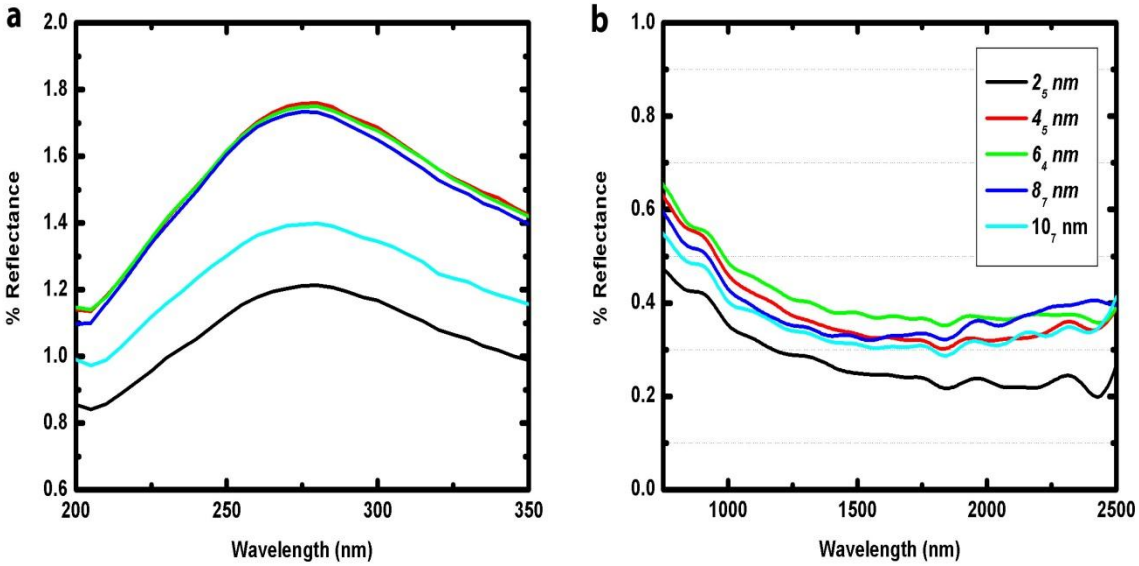

Figure 3.15. Measured hemispherical reflectance of *t -15* exposure time (best performing samples) for the near infrared (IR) spectrum. Inset shows the peak located at 275 nm (4.5 eV) in the ultraviolet spectrum (UV).

3.6. Conclusion

In summary, we have investigated the growth of MWCNTs under varying H_2 exposure times, *t -5*, *t -10* and *t -15*. For our CVD growth we found that the *t -5* H_2 exposure time yielded consistent growth results in addition to having the lowest %R (<0.25%). Measurements of our sample masses and nanotube heights allowed for calculation of the respective bulk densities of our samples; the associated effects on the film properties such as absorption were investigated. Raman spectroscopy was utilized to examine our film purity and defect content. The G_d showed that our *t -5* 2 nm samples had fewer impurities. Our %R data showed that the *t -5* H_2 exposures yield the most desirable absorbance for both of our 2 nm films. We calculated that our best sample absorbs 99.86% of light. We were able to calculate $\theta(\omega)$ from our reflectance data using the Kramers-Kronig relations. Furthermore, the K-K relations allowed us to calculate the optical properties of our material. Added research is necessary for this aspect of the research as the extrapolation points must be selected carefully. The Im ε and Re ε values, confirmed observations made by SEM and Garcia-Vidal [11]. Finally, we were able to show the effect of angular dependence on specular and diffuse reflectance.

Works Cited

1. Mizuno, K., et al., *A black body absorber from vertically aligned single-walled carbon nanotubes.* Proceedings of the National Academy of Sciences, 2009. **106**(15): p. 6044.
2. Yang, Z.P., et al., *Experimental observation of an extremely dark material made by a low-density nanotube array.* Nano Letters, 2008. **8**(2): p. 446-451.
3. Kirchhoff, G., *Uber den Zusammenhang zwischen Emission und Absorption von Licht und. WÃ¤rme.* Monatsberichte der Akademie der Wissenschaften zu Berlin, 1859: p. 783-787.
4. Hagopian, J.G., et al. *Multiwalled carbon nanotubes for stray light suppression in space flight instruments*. in *Proceedings of SPIE*. 2010: SPIE.
5. Dang, X., et al., *Virus-templated self-assembled single-walled carbon nanotubes for highly efficient electron collection in photovoltaic devices.* Nature Nanotechnology. **6**(6): p. 377-384.
6. Camacho, R., et al., *Carbon nanotube arrays for photovoltaic applications.* JOM Journal of the Minerals, Metals and Materials Society, 2007. **59**(3): p. 39-42.
7. Wang, Y., et al., *Investigation of the structure and the physical properties of nickel-phosphorus ultra-black surfaces.* Applied Physics A: Materials Science & Processing, 2008. **90**(3): p. 549-553.
8. Maloney, P.G., et al., *Emissivity of microstructured silicon.* Applied Optics. **49**(7): p. 1065-1068.
9. Huang, Y.F., et al., *Improved broadband and quasi-omnidirectional anti-reflection properties with biomimetic silicon nanostructures.* Nature Nanotechnology, 2007. **2**(12): p. 770-774.
10. Zhao, W., et al., *Fabrication, characterization and application of gold nano-structured film.* Electrochemistry communications, 2006. **8**(5): p. 773-778.
11. Garcia-Vidal, F., J. Pitarke, and J. Pendry, *Effective medium theory of the optical properties of aligned carbon nanotubes.* Physical Review Letters, 1997. **78**(22): p. 4289-4292.
12. Taft, E.A. and H. Philipp, *Optical properties of graphite.* Physical Review, 1965. **138**(1A): p. A197.
13. deHeer, W.A., et al., *Aligned carbon nanotube films: production and optical and electronic properties.* Science, 1995. **268**(5212): p. 845.
14. LÃ¼, W., J. Dong, and Z.Y. Li, *Optical properties of aligned carbon nanotube systems studied by the effective-medium approximation method.* Physical Review B, 2000. **63**(3): p. 033401.
15. Marinopoulos, A., et al., *Optical and loss spectra of carbon nanotubes: depolarization effects and intertube interactions.* Physical Review Letters, 2003. **91**(4): p. 46402.
16. Murakami, Y., et al., *Polarization dependence of the optical absorption of single-walled carbon nanotubes.* Physical Review Letters, 2005. **94**(8): p. 87402.
17. Lidorikis, E. and A.C. Ferrari, *Photonics with multiwall carbon nanotube arrays.* ACS Nano, 2009. **3**(5): p. 1238-1248.
18. Lehman, J.H., et al., *Evaluating the characteristics of multiwall carbon nanotubes.* Carbon, 2011. **49**: p. 2581-2602.
19. Bao, H., X. Ruan, and T. Fisher, *Optical properties of ordered vertical arrays of multi-walled carbon nanotubes from FDTD simulations.* Optics Express, 2010. **18**(6): p. 6347-6359.

20. Nessim, G.D., et al., *Tuning of vertically-aligned carbon nanotube diameter and areal density through catalyst pre-treatment.* Nano Letters, 2008. **8**(11): p. 3587-3593.
21. Chakrabarti, S., et al., *Number of walls controlled synthesis of millimeter-long vertically aligned brushlike carbon nanotubes.* The Journal of Physical Chemistry C, 2007. **111**(5): p. 1929-1934.
22. Hofmann, S., et al., *Effects of catalyst film thickness on plasma-enhanced carbon nanotube growth.* Journal of Applied Physics, 2005. **98**: p. 034308.
23. Yamada, T., et al., *Size-selective growth of double-walled carbon nanotube forests from engineered iron catalysts.* Nature Nanotechnology, 2006. **1**(2): p. 131-136.
24. Jantoljak, H., et al., *Low-energy Raman-active phonons of multiwalled carbon nanotubes.* Applied Physics A: Materials Science & Processing, 1998. **67**(1): p. 113-116.
25. Donato, M., et al. *Aid of Raman spectroscopy in diagnostics of MWCNT synthesised by Fe-catalysed CVD*. 2007: IOP Publishing.
26. Santangelo, S., et al., *Low-frequency Raman study of hollow multiwalled nanotubes grown by Fe-catalyzed chemical vapor deposition.* Journal of Applied Physics, 2006. **100**: p. 104311.
27. DiLeo, R.A., B.J. Landi, and R.P. Raffaelle, *Purity assessment of multiwalled carbon nanotubes by Raman spectroscopy.* Journal of Applied Physics, 2007. **101**: p. 064307.
28. Ferrari, A.C. and J. Robertson, *Raman spectroscopy of amorphous, nanostructured, diamondâ€“like carbon, and nanodiamond.* Philosophical Transactions of the Royal Society of London. Series A: Mathematical, Physical and Engineering Sciences, 2004. **362**(1824): p. 2477-2512.
29. Saito, R., G. Dresselhaus, and M.S. Dresselhaus, *Physical Properties of Carbon Nanotubes.* Imperial College Press, 1998.
30. Lucarini, V., *Kramers-Kronig relations in optical materials research*. Vol. 110. 2005: Springer Verlag.

CHAPTER 4

DETERMINATION OF OPTICAL PROPERTIES AND EFFECTS ON FILM PERFORMANCE

4.1. Experimental Improvement of Reflectance

In this experiment, samples were plasma etched with oxygen (O_2) for 10 seconds at 100 Watts, removing approximately 10-15 nm from the top layer. We choose samples from an earlier group that demonstrated a profound linear λ-dependence in addition to λ-independence. The *t =0* and *t -5* exposure samples have a Fe catalyst layer of 8 nm. The removal of the top layer of randomly oriented bridge-like nanotubes ought to increase the absorption of the films. This increase in absorption would be a result of an increase in the available void spaces and reduction in surface scattering which would encourage light trapping within the material. Further, it will provide an improvement at the air-nanotube interface, reducing the refractive index. Figure 4.1 a and b displays our %R data for two measured samples before and after O_2 plasma etching. The results indicate for the *t =0* sample, that the process did not improved the overall reflectance; rather it degraded the film performance. At the longer wavelengths (>2100 nm) %R seems unchanged though this may be due to experimental error. In the 950 to 1750 nm range, the %R degraded by an average of 50%. In the UV range we notice a shift in the peak and a reduced magnitude. However, despite these results, the λ-independence is unchanged.

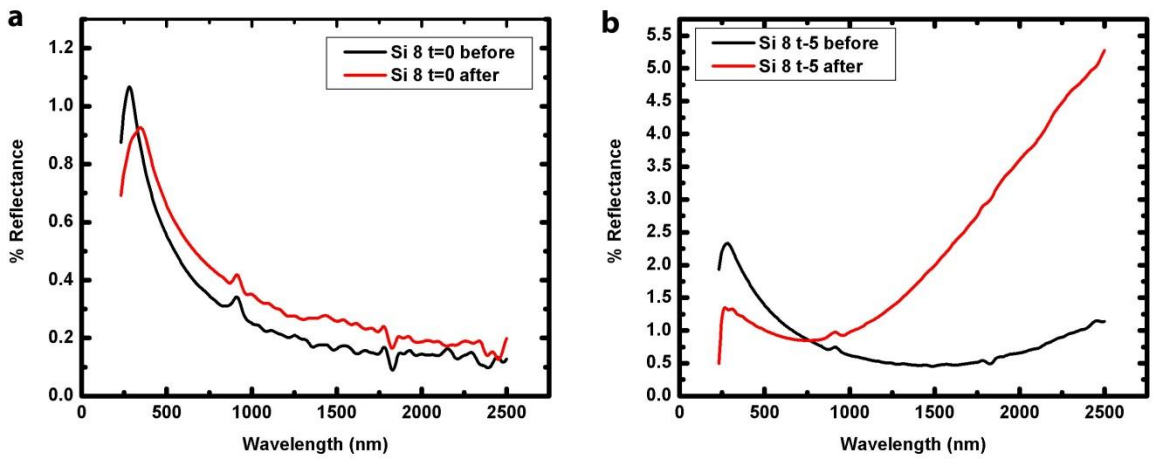

Figure 4.1. Measured hemispherical reflectance of (a) *t =0* and (b) *t -5* exposure times before and after O_2 plasma etch for an 8 nm Fe catalyst layer growth on silicon. The UV-VIS-NIR spectrum is plotted. The UV peaks are located at 275 nm (4.5 eV), though there is a shift to higher wavelength (lower energy/frequency) for t =0. The reflectance increases linearly after plasma etching for the t -5 sample, an approximate five-fold increase.

In Figure 4.2 we observe the SEM image showing the associated regions of nanotube structures from the substrate to the surface. Due to the difference in nanotube structure and alignment, these regions contain varying indexes of refraction.

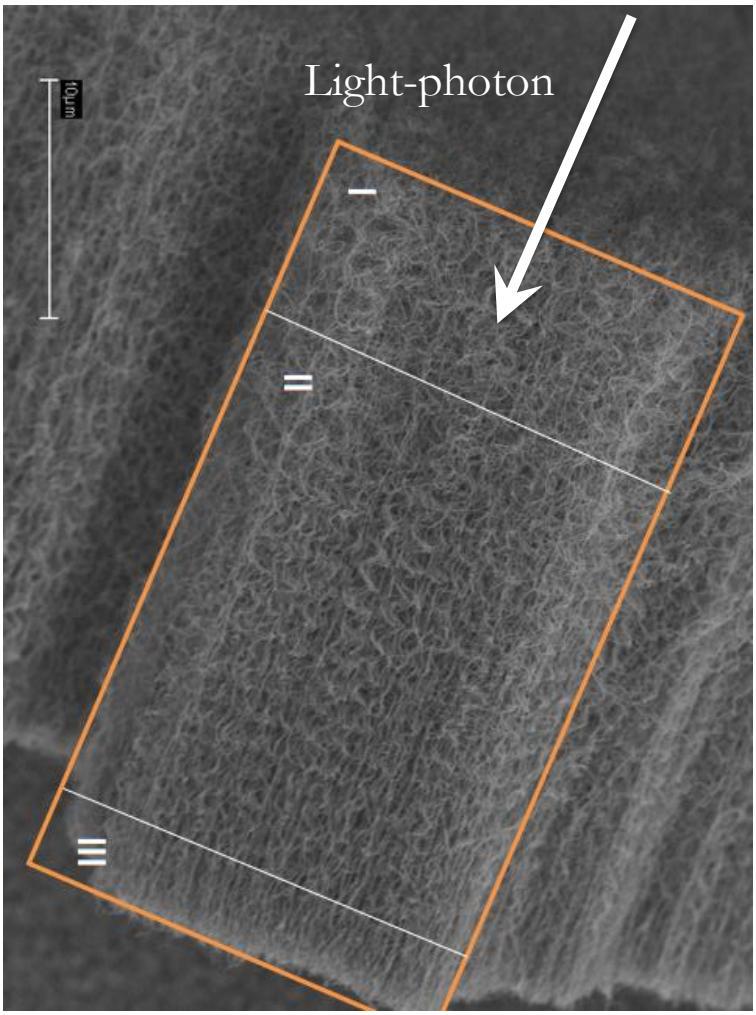

Figure 4.2. SEM image of CNTs with a height of ~ 35 μm. Region I is the surface of the aligned nanotubes which exhibit bridge-like interconnections. Region II shows highly aligned nanotubes with helical growth and Region III is the base where growth begins.

Region I is the first region and is located at the air-CNT interface and consists of randomly aligned nanotubes with bridge-like CNT connections. The random surface encourages increased diffuse scattering events along the tubule axes [1]. Additionally, these surface structures decrease the void spaces of the aligned helical nanotubes.

Region II contains vertically-aligned helical nanotubes. The helical nature is due to pentagon and heptagon defects [2] along the sp^2 structures. These tubes due to their angular nature and length allow for the reflectance, transmission and absorption of light in the film. For our purpose, removal of the region I layer and exposure of region II should further improve our films absorbance by lowering the refractive index.

Region III, the final region, contains more aligned nanotubes. However, the nanotubes are considerably short and are close to the substrate. At this height the effects of absorption are reduced due to the limited path for photons to travel. The length effect is also reduced such that we expect the reflectance to increase. This increased reflection from the substrate is a direct result of a glossy surface. Based on these observations we attempted to remove or reduce the thickness of region I, and expose region II.

Figure 4.3 (a, b, c and d) show the SEM images of samples before and after the O_2 etch for *t =0* and *t -5* sample respectively. For the *t =0* sample, we observe the removal of the surface (region I), mentioned earlier and an improvement in the void spaces (Figure 4.3.c). We also notice graphitic remnants from the etch process. It is possible that these graphitic remnants are the cause for the observed increase in %R (Figure 4.2.a).

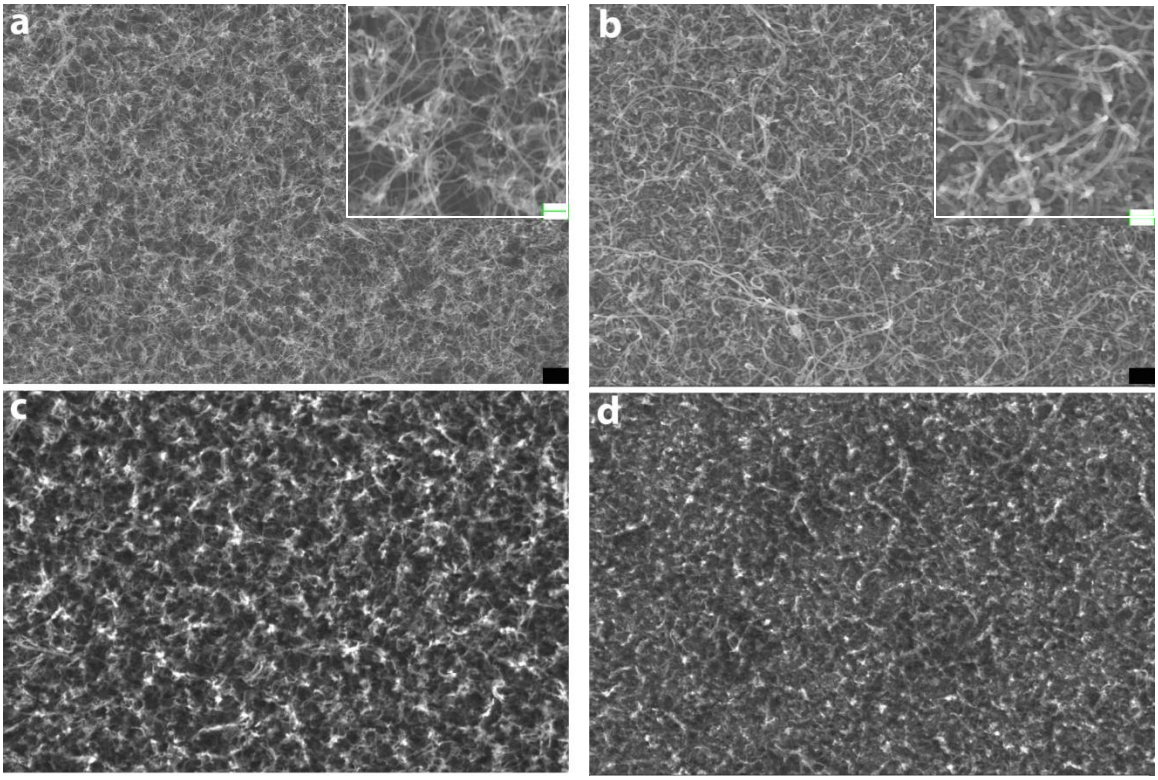

Figure 4.3. SEM images of (a) *t =0* before O_2 plasma etch (b) *t -5* before O_2 plasma etch (c) *t =0* after O_2 plasma etch and (d) *t -5* after O_2 plasma etch. Insets in (a) and (b) are higher magnifications of film. Scale bars are 200 nm, for regular and insets.

For the *t -5* sample, the plasma etch removed the surface diffusive scattering of the bridge-like surface exposing the nanotubes below. Figure 4.3 (b and d) show the SEM images for this sample. In Figure 4.3.d the surface appears as a uniform film with relatively low void spaces. It should be noted that even though the contrast of the SEM shows topologically where the voids are located, it cannot ascertain the depth. The effect of the linear λ-dependence is worsened as depicted in Figure 4.2.b due to the lack of void spaces in the nanotube film. Additionally, since the nanotubes are more closely packed without the random layer, the density of the material should increase.

4.2. Wavelength-Dependence Mechanisms of Reflection

We conducted additional experiments to comprehend why we observed the linear increase in the reflectance (λ -dependence) of our samples in the infrared region. Our HR set-up consisted of two sample mounts at an angle of incidence of 8^o from the normal and 0^o to examine any changes in our reflectance data. We selected two samples from an earlier growth group which exhibited this phenomena (as the optimization improved this phenomena decreased). Figure 4.4.a and 4.4.b shows the graphs of a *t =0* and *t -5* 8 nm Fe catalyst layer sample. In Figure 4.4.a shows that for both incident angles, the reflectance spectrum is unchanged. Figure 4.4.b, we observed that the reflectance increased linearly at ~1700 nm for the 8^o angle of incidence. However, at the normal, 0^o we immediately observed the absence of this linear increase. In order to confirm whether this was indeed due to λ-dependence we measured a sample with λ-independence.

We explain this phenomenon as follows: our data recorded the total reflectance (R_T) from our sample, which is all of the reflected light from the films surface. R_T is composed of two components, specular (R_S) and diffuse (R_D) reflectance. The surfaces of the nanotube are rough on the nanometer scale, where photons are scattered in both forward and backward directions. As a result they are an excellent diffuse surface. At an incidence of 0^o the beam is reflected 180^o off the nanotube surface, expunging the R_S component, leaving solely the R_D. We hypothesize that at 8^o, the R_S component is responsible for the λ-dependence. Hence, the optical reflectance mechanism fluctuates from R_D

to R_S as λ increases. R_S may be caused by the dense electron clouds below the diffuse layer as the nanotubes act as a bulk material with little intertube spacing.

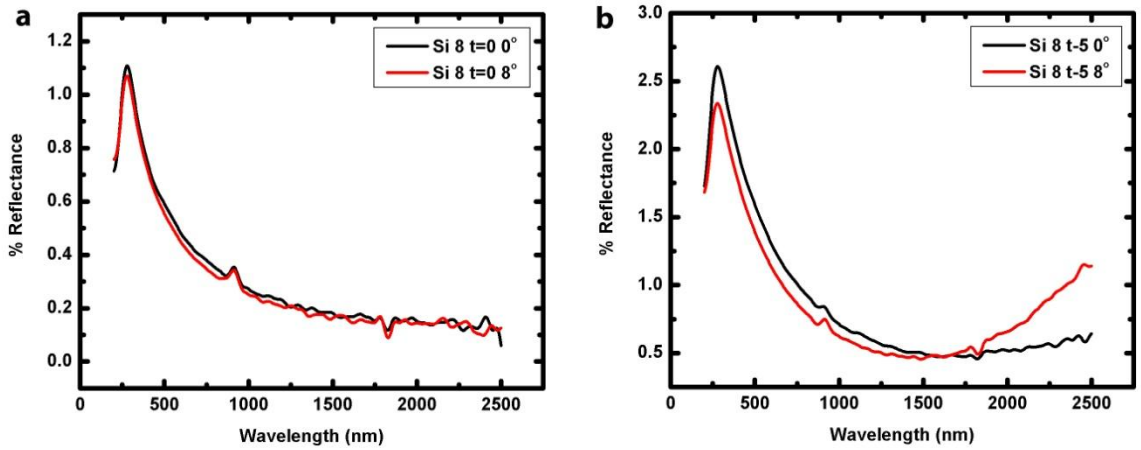

Figure 4.4. Measured hemispherical reflectance for (a) *t =0* Si 8 nm catalyst thickness at 0^o and 8^o angles of incidence (b) *t -5* Si 8 nm catalyst thickness at 0^o and 8^o angles of incidence. In (b) we observe the absence of the specular component, suggesting that the linear wavelength-dependence is a component of specular reflection.

4.3. Kramers-Kronig Relations

The K-K relations describe the fundamental connection between the real (Re) and imaginary (Im) parts of linear complex optical functions that exhibit light-matter interaction phenomena [3]. In reflectance spectroscopy, K-K couples the measured reflectance and phase of the reflectivity allowing retrieval of the phase and the ability to extract quantitative information, such as the refractive index, N (ω) and complex dielectric function, ε_{eff} (ω). To obtain the optical constants, reflectance is commonly measured at normal incidence and then followed by dispersion relations to retrieve the phase, θ (ω). For our measurements we utilized angle of incidence of 8^o, which is near normal, thus considering it to be 0^o.

From Fresnel's law, the complex reflectivity, *r* (ω), at the boundary between sample and vacuum is given by,

$$r(\omega) = \frac{N(\omega) - 1}{N(\omega) + 1} = \frac{\eta(\omega) - 1 + i\kappa(\omega)}{\eta(\omega) + 1 + i\kappa(\omega)} \qquad 4.1$$

where ω is the frequency in eV, η (ω) the index of refraction (Re), i a complex variable and κ (ω) is the extinction coefficient (Im). We obtain,

$$R(\omega) = \left|r(\omega)\right|^2 = r(\omega)[r(\omega)]^* \qquad 4.2$$

In polar coordinates the complex reflectivity is expressed as,

$$r(\omega) = R(\omega)e^{i\theta(\omega)} \qquad 4.3$$

Such that,

$$\ln r(\omega) = \ln\left|R(\omega)\right| + i\theta(\omega) \qquad 4.4$$

If we perform of a Hilbert transform to equation 4.4, we can relate the real and imaginary parts as,

$$\theta(\omega) = -\frac{2\omega}{\pi} P \int_0^\infty \frac{\ln\left|R(\omega')\right|}{\omega^{2'} - \omega^2} d\omega' \qquad 4.5$$

In this equation for the phase of complex reflectivity, *P* is the principle value integral.

In order to perform the principle value integration in equation 4.5, we first needed to smooth our reflectance data. We must also extrapolate the data down to ω = 0 and out to ω = ∞. The principle value requires that the function and its derivative be continuous. In order to extrapolate to zero we use the simple function,

$$|r(\omega)| = |r(\omega_o)|\left(1 + a\left(1 - \frac{\omega^2}{\omega_o^2}\right)\right) \qquad 4.6$$

where ω_o is the lowest frequency point at which data was taken, f (ω_o) in the reflectance at that point and a is the chosen to give a continuous derivative. To extrapolate to infinity, we use

$$|r(\omega)| = \frac{|r(\omega_o)|}{(1 + a(\omega^2 - \omega_0^2) + b(\omega^2 + \omega_0^2)^2)} \qquad 4.7$$

where ω_o is the highest frequency at which there is data, f (ω_o) the reflectance at that frequency, a is determined by requiring a continuous slope. The additional term is added to yield a more convergent integral and to allow us to examine the sensitivity to how rapidly we continue f (ω) to zero.

In Figure 4.5 (a and b) we show the smoothed data and the extrapolations for two cases. We examine the *t -5* Si8 sample before and after the O_2 plasma etch. Note, we perform two extrapolations in Figure 4.5.a. We use these in the K-K relations to generate the phase of r (ω), θ (ω), shown in Figure 4.6. We observe that the extrapolation of ω to ∞ does not have a great effect on the data which is continued downward toward zero.

The phase, θ (ω) is not something for which there is any great intuition. Given r (ω) we can use equation 4.1 to obtain the index of refraction, N (ω), both its real and imaginary components. Further the susceptibility ε (ω) can be found from

$$\frac{\varepsilon(\omega)}{\varepsilon_o} = \sqrt{N(\omega)} \qquad 4.8$$

In Figure 4.6 we observe the plots of $\varepsilon(\omega)$ as calculated from the dispersion relation. We can compare our value for Im $\varepsilon(\omega)$ to that calculated by Garcia-Vidal et al[1]. We observe similar ω-dependence and similar magnitudes. For our sample, we observe the shift of the UV peak from high to low energy. At the higher energy the nanotubes have more intertube spacing, however at the lower energies the nanotubes are in very close contact. Further we can surmise that out nanotube diameters are much larger than those in Garcia-Vidal. Thus we believe this approach is reasonable and yields $\varepsilon(\omega)$. The imaginary components of $\varepsilon(\omega)$ are a clear measure of a materials absorbance. Thus using the K-K dispersion relations could help assess influence of a material at suppressing scattered light.

Unfortunately, the application of equation 4.5 to our other measured reflectance data has proven problematic. The same calculation as used for the above two cases yields N (ω) and $\varepsilon(\omega)$ with unphysical imaginary components. This would imply an exponentially increasing wave on the light entering the medium. Others [4-7] have found similar difficulty and have traced the problem to the utilization of a long $|r|$ in the dispersion integral. The dispersion relation is not valid if r (ω) has a zero in the upper half plane. Several suggestions have been made to circumvent this problem. Whether their modified approach can be used to handle the data taken here warrants further investigation.

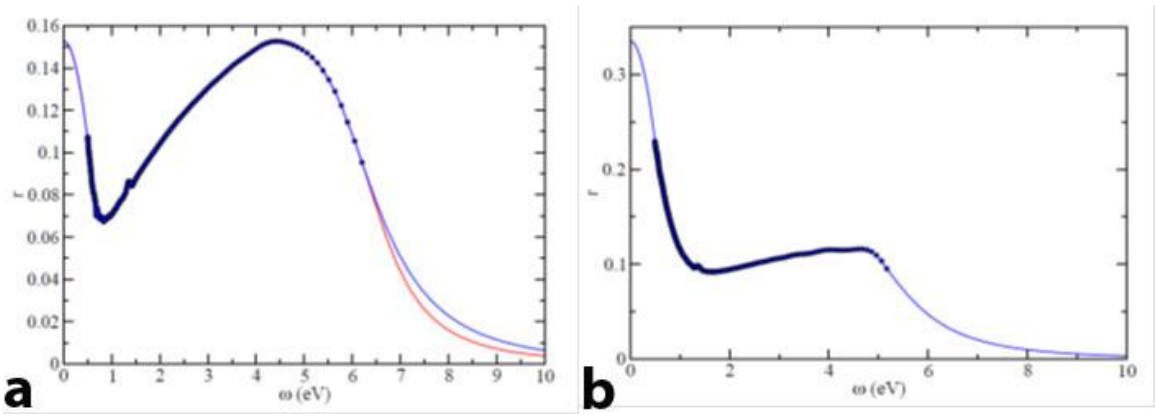

Figure 4.5. Smoothed reflectance data for a *t -5* Si 8 nm catalyst thickness and the extrapolations used (a) before plasma etch and (b) after plasma etch.

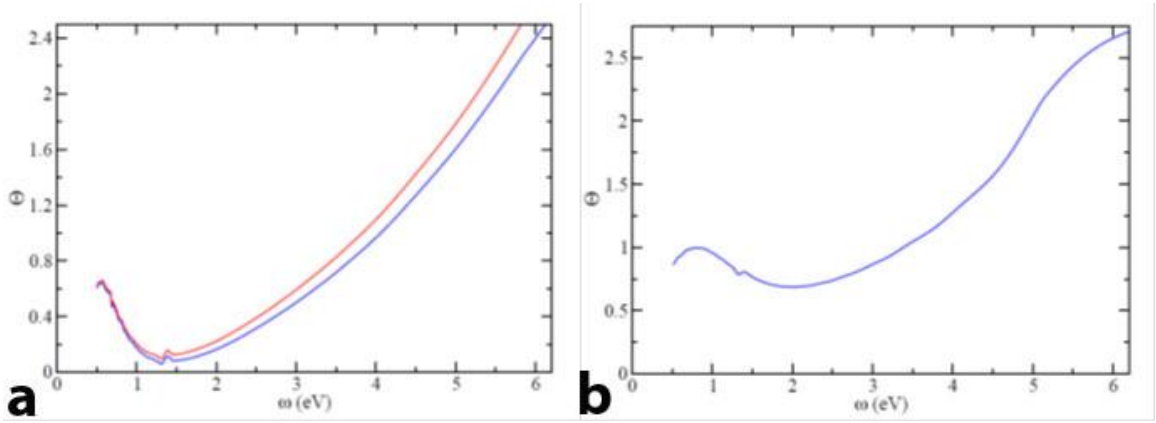

Figure 4.6. Phase data for a *t -5* Si 8 nm catalyst thickness (a) before plasma etch and (b) after plasma etch.

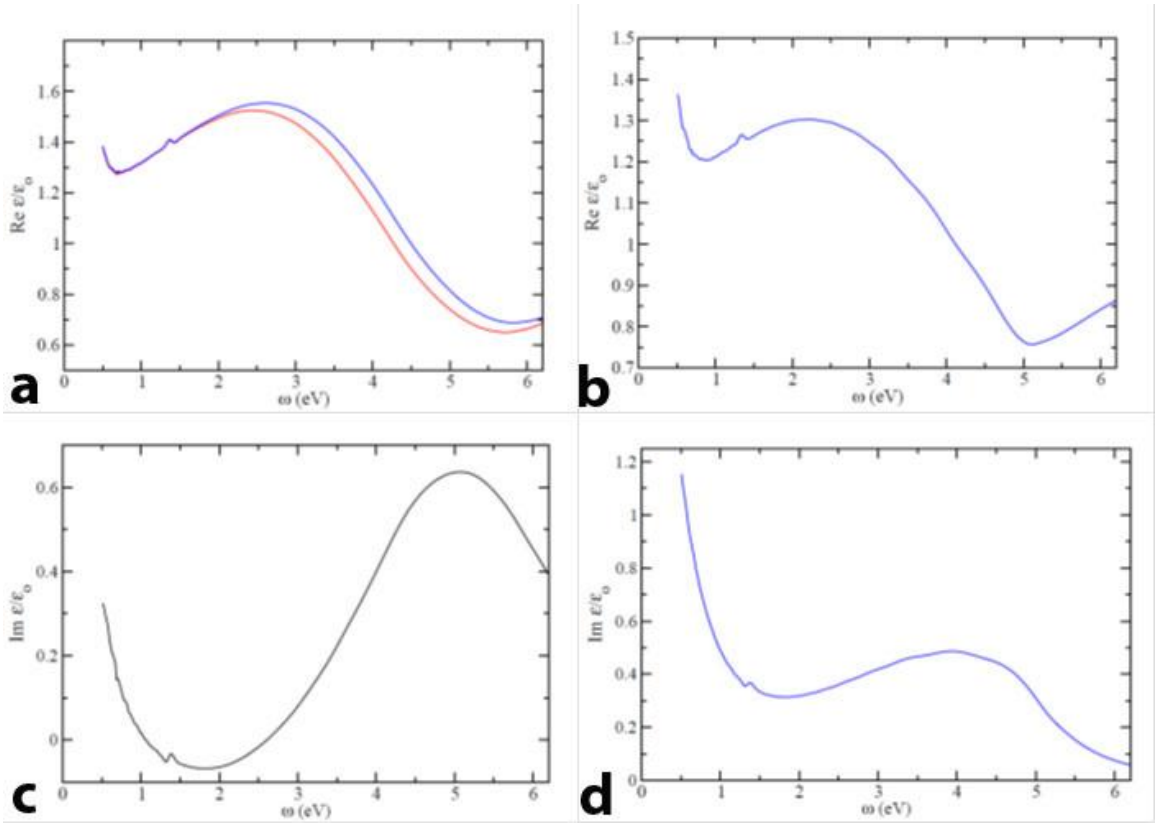

Figure 4.7. Calculated ε (ω), with real and imaginary components for *t -5* Si 8 nm catalyst thickness. (a)Re ε (ω) before plasma etch (b) Re ε (ω) after plasma etch (c) Im ε (ω) before plasma etch (d) Re ε (ω) after plasma etch.

4.5. Conclusion

We calculated that our best sample absorbs 99.86% of light. We were able to calculate θ (ω) from our reflectance data using the Kramers-Kronig relations. Furthermore, the K-K relations allowed us to calculate the optical properties of our material. Additional research is necessary for this aspect of the projrect as the extrapolation points must be selected carefully. The Im ε and Re ε values, confirmed observations made by SEM and Garcia-Vidal [1]. Finally, we were able to show the effect of angular dependence on specular and diffuse reflectance for our samples.

Works Cited

1. Garcia-Vidal, F., J. Pitarke, and J. Pendry, *Effective medium theory of the optical properties of aligned carbon nanotubes.* Physical Review Letters, 1997. **78**(22): p. 4289-4292.
2. Lehman, J.H., et al., *Evaluating the characteristics of multiwall carbon nanotubes.* Carbon, 2011. **49**: p. 2581-2602.
3. Lucarini, V., *Kramers-Kronig relations in optical materials research*. Vol. 110. 2005: Springer Verlag.
4. Smith, D.Y., *Dispersion relations for complex reflectivities.* JOSA, 1977. **67**(4): p. 570-571.
5. Smith, D. and C.A. Manogue, *Superconvergence relations and sum rules for reflection spectroscopy.* JOSA, 1981. **71**(8): p. 935-947.
6. King, F.W., *Dispersion relations and sum rules for the normal reflectance of conductors and insulators.* The Journal of Chemical Physics, 1979. **71**: p. 4726.
7. Plaskett, J. and P. Schatz, *On the Robinson and Price (Kramersâ€"Kronig) Method of Interpreting Reflection Data Taken through a Transparent Window.* The Journal of Chemical Physics, 1963. **38**: p. 612.

CHAPTER 5

CONCLUSIONS & FUTURE WORK

In this dissertation we have demonstrated the applicability of the electrophoretic deposition (EPD) technique to assemble thin films of carbon nanotubes (buckypapers). We suspended the MWCNTs in an aqueous media in order to facilitate deposition onto a stainless steel substrate. We demonstrated and effective method to remove the film once deposited and termed this the "mechanical cleavage" technique. The random porous networks of nanotubes were comparable to other BPs fabricated by alternate techniques in both its Young's modulus and Tensile strength.

Furthermore we have addressed a direct technological application using MWCNTs for NASA grown via the chemical vapor deposition (CVD) method. Due to their vertical alignment, films of nanotubes have come extremely close to the theoretical emissivity of a blackbody. We investigated various H_2 exposure times to find consistent growth parameters for optimal absorption performance. By varying the exposure times we were able to control, within experimental reason, the factors important to nanotube absorption such as height, density, *v.f.f.*, intertube spacing and incident angle. We developed a technique to measure the bulk density of our samples. The optical properties of a few samples were analyzed using the Kramers-Kronig relations and yielded quantitative and qualitative information on our samples.

To this end, the research discussed in this dissertation should be explored further. En route to achieving uniform films via CVD, several exciting research questions remain. For instance, understanding the effects of Ostwald ripening and utilizing this phenomenon may open a new understanding of growth termination and catalyst-underlayer adhesion. Another idea follows from the O_2 plasma etch trial. If researchers are able to effectively remove the randomly oriented nanotube surface then achieving a near perfect blackbody is in sight, as well as solar and thermal conversion efficiencies. We began an analysis using the K-K relations and found that they accurately retrieve intrinsic material constants. Further investigation of our samples is necessary, especially in the mid- to far-infrared spectrum. I believe this would aid in NASA's goal to replace its existing coating material with nanotubes.

APPENDIX A

ELECTROPHORETIC DEPOSITION THEORY

DLVO Theory

Derjaguin, Landau, Verwey and Overbeek (DLVO) theory, combines the effects of attractive and repulsive interactions between two particles in a system. The overall stability of the system depends on the interaction between the individual particles in the suspension [1]. Descriptions of these interactions in the suspension are in terms of the van der Waals attraction (U_{VdW}) and electrostatic repulsion (U_{elect}). From these mechanisms acting in a dispersed system, we can postulate whether the particles will agglomerate or coagulate. To avoid particle agglomeration, a high electrostatic repulsion due to high particle charge is required. For instance, during the formation of the deposit, the particles come closer to each other with increasing attractive force. If the charge on the particle is low, the particles will coagulate regardless of inter-particle spacing. This leads to deposits that are more porous in nature. In contrast, if the particles have a higher surface charge during deposition, they will repel each other, occupying positions that lead to a higher packing density [2].

If we examine a negatively charged MWNT in its colloidal medium surrounded by both positive and negative ions and water, as depicted in Figure A.1, there will be a fixed layer of positive ions at the surface. This layer is the stern layer. Outside this stern layer is a diffuse layer of counter ions, in which a reduction of positive ions decreases with increasing distance from the MWNT.

Formation of the diffuse layer occurs from free ions in the medium/system under the influence of electric attraction and thermal motion [1]. The diffuse layer electrically screens the stern layer. Both the stern and diffuse layers make up the double layer. The boundary at the interface of the diffuse layer and bulk medium (suspension) is the slipping plane. Within this region, the MWNT acts as a single entity when a force is applied, inducing the motion of MWNT and the double layer. The potential at this boundary is the zeta potential (refer to section A for the value). This potential determines the particles velocity *v* by which they move under the influence of the applied electric field E and the electrophoretic mobility μ given by

$$\mu = \frac{v}{E}. \qquad (1)$$

The relationship of the zeta potential ζ and the electrophoretic mobility is given by the Smoluchowski equation [1]

$$\mu = \frac{\varepsilon_0 \varepsilon_r \zeta}{\eta} \qquad (2)$$

where ε_0 is the permittivity of vacuum, ε_r is the relative permittivity of solvent, and η the solvent viscosity. Thus, the mobility of the particle depends linearly on the dielectric constant of the fluid, the zeta potential and the potential gradient and is inversely proportional to the fluid viscosity.

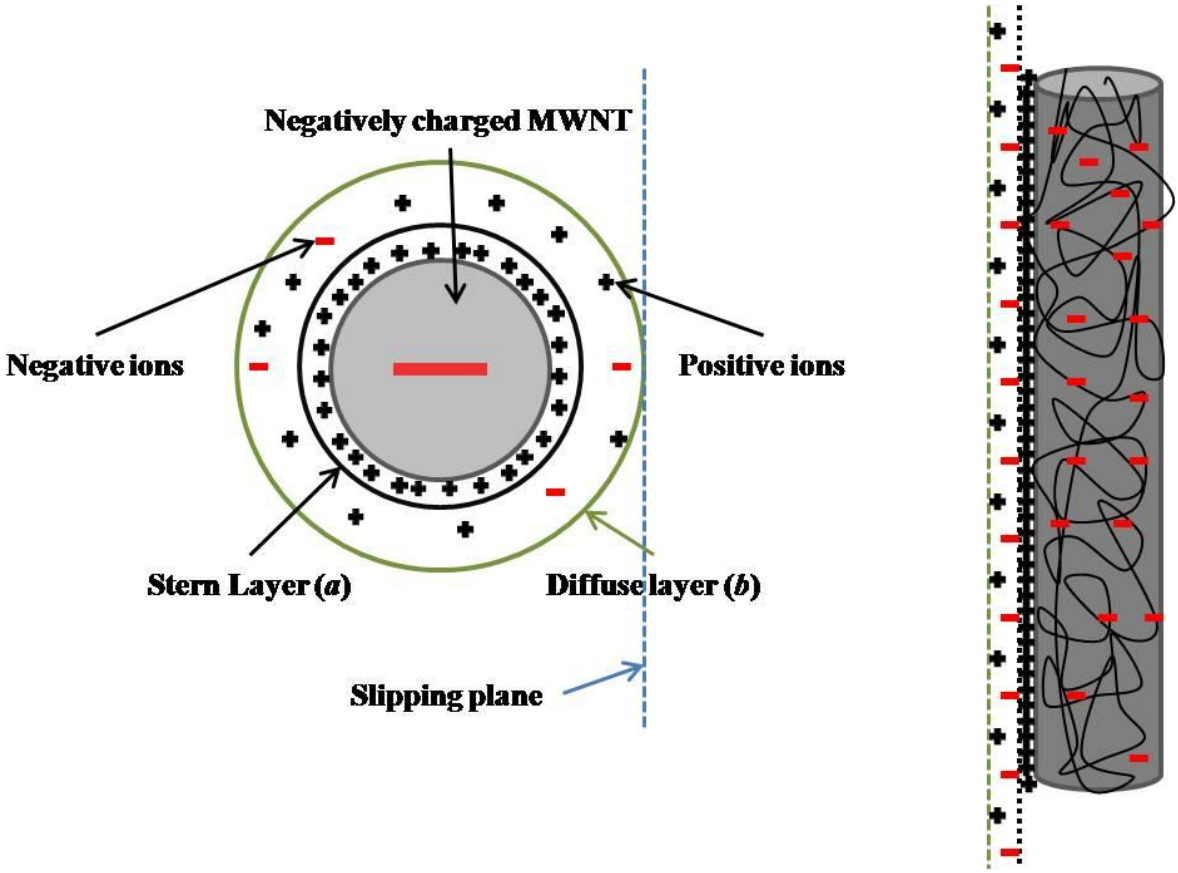

Figure A.1. Schematic of double layer surrounding MWNT as two parts; the inner region where ions are strongly bound is the stern layer (*a*), the outer region where ions are less firmly associated is the diffuse layer **(*b*)** both regions comprise the double layer (*a* and *b*). The diffuse layer contains a boundary known as the slipping plane, where the particle (MWNT) acts as a single entity. The potential at this boundary is the zeta potential.

In the colloidal suspension, we assume Na^+ is one of the free ions in the system due to the proprietary surfactant present on our nanotubes. This assumption is based on the EDS scans. Neglecting all but the electrostatic and the van der Waals forces and treating them as separable entities, DLVO theory allows for a description of colloidal suspensions [3].

The combination of U_{VdW} and U_{elect} describes the total interaction energy (U_T) of the suspension. At nanometer distances, the attractive force is due primarily to the van der Waals interaction, which is a result of fluctuating electric dipole effects present in the suspension. Van der Waals attraction follows the power law whose strength varies with the Hamaker constant (A_H) and a geometrical factor. Typically, spherical bodies represent the geometry for particles in colloidal suspensions. For our MWNTs, rigid cylindrical bodies are used for the approximation of the van der Waals potential. We express their interactions as a function of their separation distance and orientation. The two orientations of focus are parallel and perpendicular. In the case of two infinitely long thin cylinders far apart where L **>>** z, the equation is given by [3]:

$$U_{vdW} = \left(\frac{-3A_H}{8\pi}\right)\left(\frac{A_1 A_2}{z^5}\right) \tag{3}$$

$$U_{vdW} = \left(\frac{-A_H}{2\pi}\right)\left(\frac{A_1 A_2}{z^4}\right) \tag{4}$$

where A_H is the Hamaker constant, A_1, A_2 the fixed cross-sectional areas and z is the center-to-center separation as shown in Figure A.2. In addition, we can express them as two infinitely long cylinders near contact, given by [3]:

$$U_{vdW} = \left(\frac{-A_H}{24 l^{3/2}} \right) R^{1/2} \tag{5}$$

$$U_{vdW} = \left(\frac{-A_H}{6} \right) \frac{R}{l} \tag{6}$$

where R is the fixed radii of the MWNTs and *l* is the variable surface separation where *l* << R, as demonstrated in Figure A.3.

The Hamaker constant relates to the dielectric properties of the MWNTs and the intervening space. Theoretical estimates have been reported in the literature for the Hamaker constant of CNTs, which is approximated as A_H = 6 x 10^{-19} J (3.744 eV) [4].

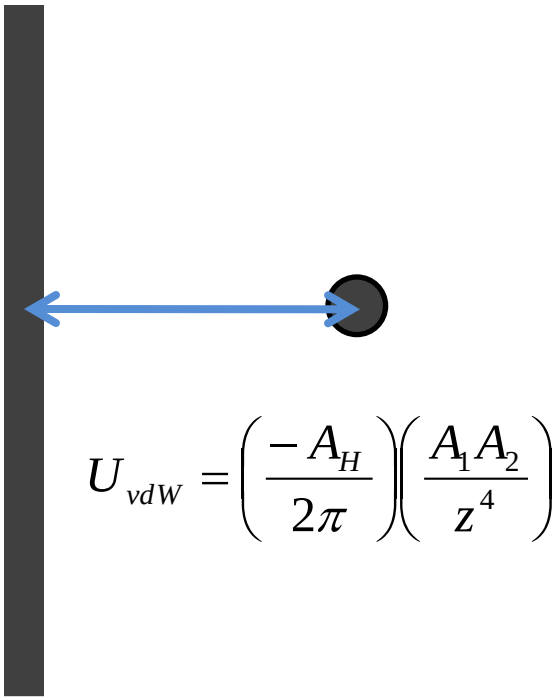

$$U_{vdW} = \left(\frac{-A_H}{2\pi}\right)\left(\frac{A_1 A_2}{z^4}\right)$$

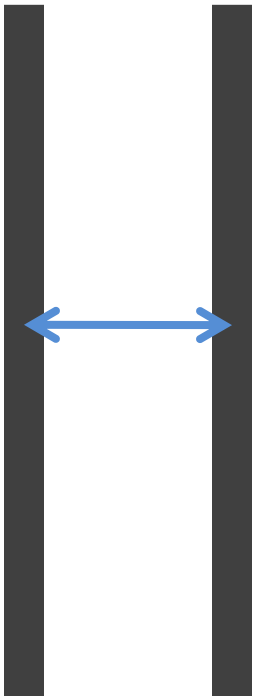

$$U_{vdW} = \left(\frac{-3A_H}{8\pi}\right)\left(\frac{A_1 A_2}{z^5}\right)$$

Figure A.2. (*Top)*. Infinitely long cylinders whose orientation is perpendicular and separation distance far apart, z coressponds to the minimal center-to-center separtion, A_1 and A_2 are the fixed cross-sectional areas per unit length. (*Below)*. Infinitely long thin parallel cylinders.

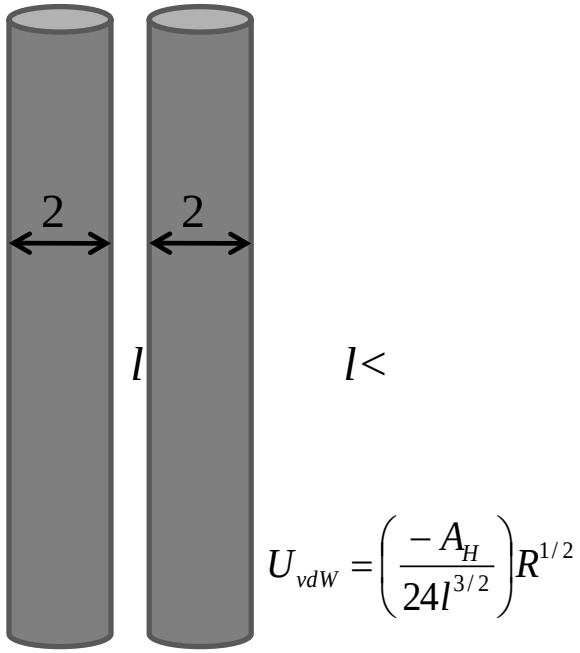

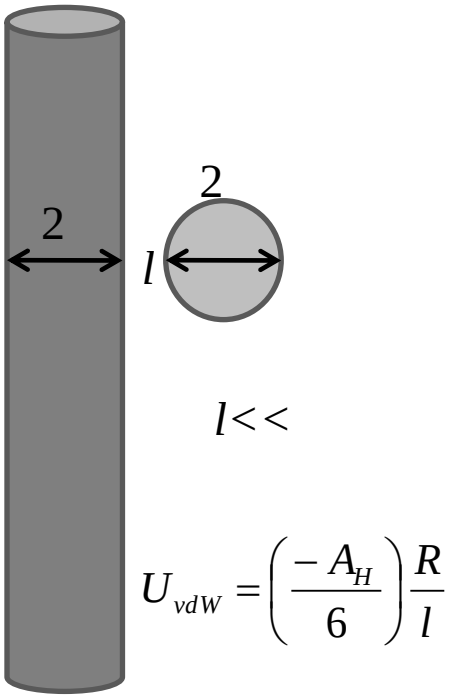

Figure A.3. (*Top)*. Infinitely long, parallel circular cylinders with fixed radii R and near contact where the variable surface separation *l* << R. (*Below)*. Infinitely long perpendicular cylinders near contact.

A graph of the van der Waals energy vs. center-to-center separation for these rigid fixed bodies of parallel and perpendicular pairs of CNTs is shown in figure A.4. The van der Waals energy was calculated using the Hamaker constant (~ 3.744 eV) value. For the length of the MWNTs 250 nm was taken as a rough approximation. As the center-to-center, separation approaches zero, the magnitude of the van der Waals forces increases. These calculations suggest stronger inter-particle binding for CNTs that are parallel.

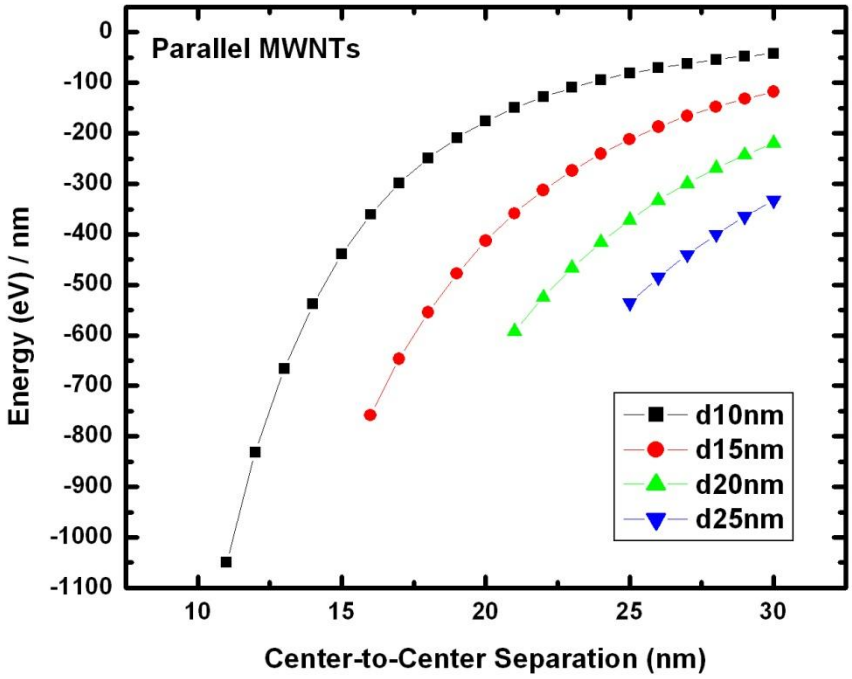

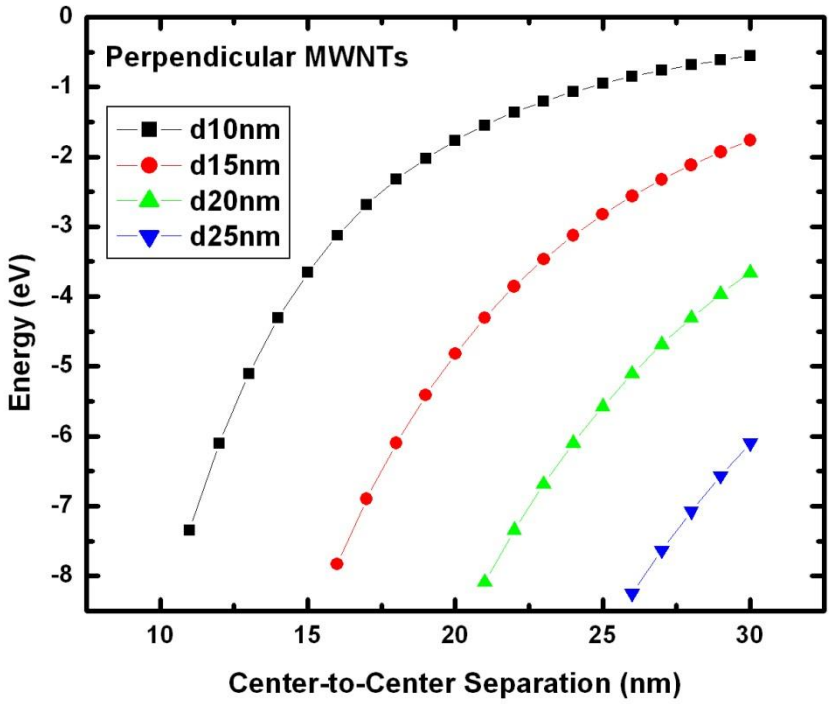

Figure A.4. Plot of the van der Waals potential energy vs. center-to-center separation between rigid CNTs of varying diameters for equations (3) and (4). Nanotubes aligned in a parallel orientation (top) and nanotubes aligned perpendicularly (bottom).

Equation (7) is the representation of the coulomb interaction of the aqueous dispersed MWNTs:

$$U_C = \left(\frac{4\pi R \sigma^2 e^{-\kappa D}}{\kappa^2 \varepsilon_0 \varepsilon} \right) \tag{7}$$

where R is the radius, κ^{-1} the Debye screening length, ε_0 the permittivity of free space and ε the relative permittivity and D is the inter-tube spacing. In colloidal suspensions, the Debye length controls the range of the double layer interaction with other particles. In order to derive this expression, there are a few assumptions one makes. First, we must approximate the charge on the surface of the MWNTs. To determine this value, we solve the mobility equation for the charge number (Z):

$$\mu = \left(\frac{Ze}{6\pi\eta R_h} \right) \tag{8}$$

where R_h is the hydrodynamic radius of the MWNT and η the viscosity of the suspension at room temperature. From earlier experiments, we determined the value of the mobility for our MWNT solution, as measured by dynamic light scattering, to be -3.2 10^{-4} cm^2 V^{-1} s^{-1}. Before we proceed with the solution of equation (2), we must find a solution for the existing unknown value of R_h. The expression for the hydrodynamic radius is equation (3); [5]

$$R_h = \left(\frac{\beta D_c}{3\left(\ln 2\beta - 1/2\right)} \right) \tag{9}$$

where $\beta$is the nanotube length (60) and D_c (25 nm) the outer diameter of the nanotube. Solving this equation for a fixed rigid MWCNT, we arrive at a value of

116 nm for R_h. Plugging this value into equation (8), we obtain a value of 438 for the charge number (Z) on the surface on the nanotubes.

Now that we have a value for surface charge on a MWCNT, we proceed to derive the force F (F = - dU/dr) between two MWCNTs surfaces. The force between two spheres in terms of the energy per unit area of two flat surfaces at the same separation *l* is known as the Derjaguin approximation. It is applicable so long as the range of the interaction and the separation *l* is much less than the radii of the spheres [5]. The approximation is useful since it is beneficial to derive the interaction energy for two planar surfaces rather than for curved surfaces. If we assume two nanotubes with radii of R_1 and R_2 are oriented perpendicular to one another, θ=90^o the Dejaguin approximation is [5]

$$F(D) = 2\pi(W)\frac{\sqrt{R_1 R_2}}{\sin\theta} \qquad \text{for } l << R_1, R_2. \qquad (10)$$

for cylinders of equal radii, R = R_1 = R_2 which reduces the equation further. Now that it has been shown that the distance between the two nanotubes act as two planar surfaces, we express the interaction energy as **[5]**,

$$W = \left(\frac{2\sigma^2 e^{-\kappa D}}{\varepsilon\varepsilon_o}\right) \qquad (11)$$

where the term σ is defined as:

$$\sigma = \left(\frac{Ze}{2\pi Rl} \right) \tag{12}$$

where Z is the charge number, *l* the tube length, R the radius, e the quantized electric charge.

The term κ^{l} represents the Debye screening length, which defines the thickness of the double layer encapsulating a particle. It is expressed as:

$$\kappa^{-1} = \left(8\pi\lambda_B c\right)^{-1/2} \tag{13}$$

with c (units of m^{-3}) being the number density of monovalent ions (counter-ions), and λ_B the Bjerrum length. The Bjerrum length is the separation at which the electrostaitic interaction between charges (*e*) is comparable in magnitude to the thermal energy $k_B T$. It is represented as;

$$\lambda_B = \frac{e}{4\pi\varepsilon\varepsilon_o k_B T} . \tag{14}$$

Finally, we derive equation (7) to obtain the expression for nanotubes. In order to accomplish this we need to integrate the force F (F = - dU/dr), where the expression for U equation (7) is denoted below,

$$U = -A\int W dD . \tag{15}$$

Figure A.5 shows the graphs of the Coulomb potential as a function of the Debye screening length. The MWNTs have a radius R of 12.5 nm and a surface charge Z of 438. In pure water, the Debye length is 960nm where the concentration of ions is at equilibrium. For the MWNT suspension, we will look at two cases where the Debye length is 25 to 100 nm and 200 to 960 nm. The plots show that the larger the screening on the tubes, the more repulsive their interactions which translates into a stable suspension.

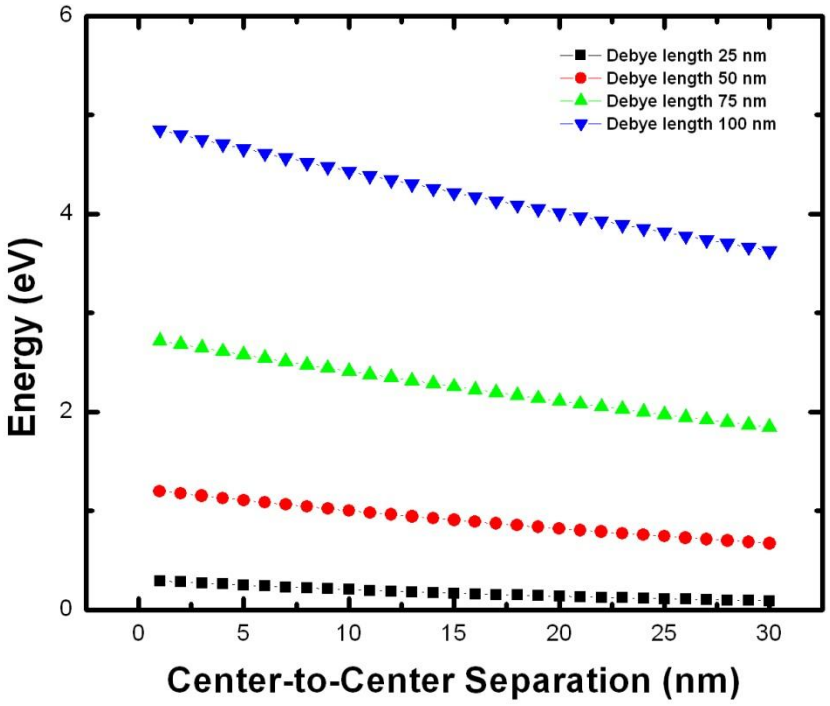

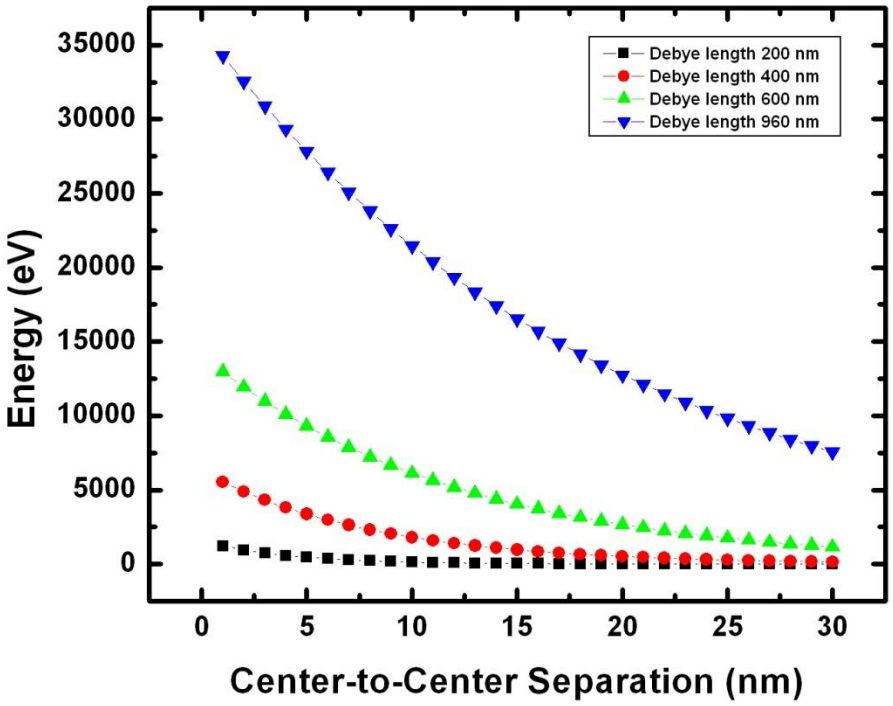

Figure A.5. Plots of the Coulomb potential energy vs. center-to-center separation between two parallel CNTs of varying Debye screening lengths.

An alternate description of the MWNT colloidal system can be described as nanotube bundles with rotational motion occupying a spherical space. Figure A.6 shows the MWNT bundle occupying spherical while in motion. Values for the size distribution of these bundles were obtained using the Malvern Zetasizer Nano series. Three samples were prepared for these measurements by varying the pH value from a dilution of the standard suspension (CNT1). Increasing the hydronium ion concentration lowered the pH values of CNT2 and CNT3 where visible aggregation occurred. This lowering of the pH effectively reduces the

double layer. Figure A.7 shows the size distribution for the three samples. This geometry may provide a more accurate description of the MWNT suspension than that of the fixed rigid bodies.

Figure A.6. MWNT bundle with rotational symmetry occupying spherical space.

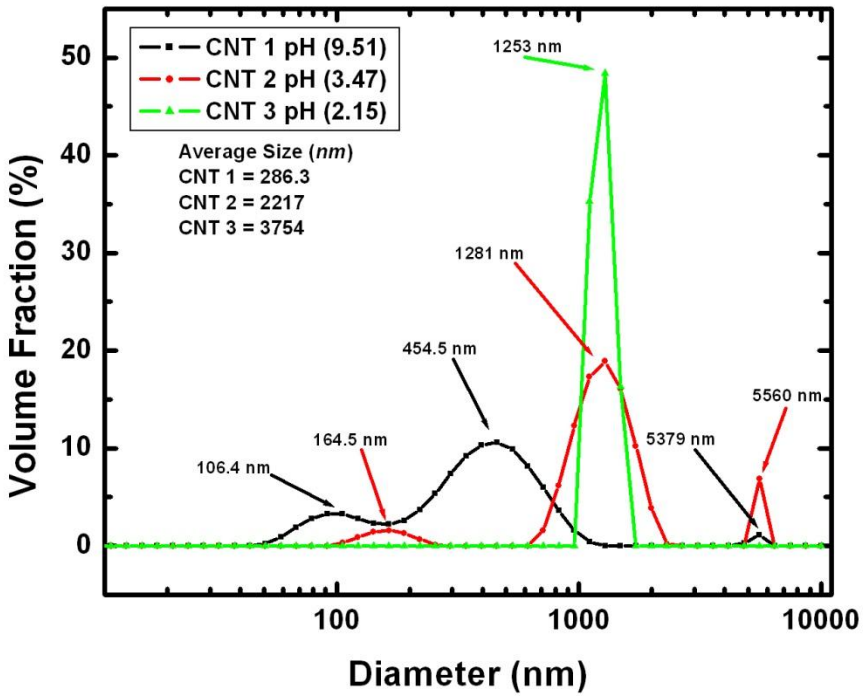

Figure A.7. Size distribution of MWNTs in aqueous media with varying pH values. pH values go from basic (typical suspension) to acidic.

Works Cited

[1] L. Besra and M. Liu, Prog. in Mater. Sci. 52 (2006) 1-61.

[2] H.G. Krueger,A. Knote, U. Schinder, H. Kern and A. R. Boccaccini J. Mater. Sci. 39 (2004) 839.

[3] Parsegian V.A. "*Van der Waals Forces,*" Chapter 1; (2005).

[4] T. Kuzumaki, Y. Mitsuda, *Diamond and Related Materials* **2008**, *17*, 615-619.

[5] Israelachvili J., "*Intermolecular & Surface Forces,*" Chapters 11 and 12; (1985).

APPENDIX B

PRELIMINARY EXPERIMENTS

H_2 Exposure Investigation

Our initial investigation of the effects of H_2 exposure times were conducted with exposure times of *t-5*, *t=0* and *t+5,* each performed twice on silicon (Si) and titanium (Ti) substrates with an Fe layer thicknesses of 6nm and 8nm (i.e. 6 nm layer). **Table B.1** further clarifies this nomenclature. The samples were loaded into the three zone furnace according to **Figure B.1** where the directional flow of gases is shown. Initially we assumed that the position of the samples were a contributing factor to the erratic growth of the samples on the Si substrates. Li *et al*.[1] reported that longer CNTs were grown downstream in the furnace and becomes more prominent with increasing growth time. They concluded that factors such as the temperature of the gas mixture and it flow velocity are responsible though they did not have an effect on the quality of CNTs.

Table B.1: CVD runs (numbers) for samples with respective H_2 exposure times.

CVD Run Number	*H_2 Exposure*	*Set Number**	*Results*
1	t -5	1	Growth
2	t =0	1	Growth
3	t +5	1	Growth
4	t -5	2	Growth
5	t =0	2	Growth
6	t +5	2	Growth

*The set numbers refer to samples that were coated with the Al_2O_3 under layer and Fe catalyst concurrently in the physical vapor deposition system.

Figures B.2 and B.3 shows the results of the average height measurements for the nanotubes grown as a function of varying H_2 exposure times. We note that the larger error bars for the Ti samples are due to the inherent substrate roughness which affects the deposition of the Al_2O_3 under-layer and the catalyst layer during PVD deposition. For the t-5 exposure times, the 6 nm Fe catalyst on the Si substrate has heights of 47.2 ± 1.6 μm and 42.0 ± 1.7 μm for CVD runs 1 and 4 respectively. **Figure B.4** shows the average nanotube height as a function of sample position for CVD runs 1 and 4. The 6 nm Fe catalyst on the Ti heights at position 2 are 92.7 ± 9.4 μm and 98.9 ± 2.7 μm for the identical runs. This increase in height is approximately a two-fold increase over the Si samples at position 1. For the 8 nm Fe catalyst samples at positions 3 and 4, the heights of Si samples are 42.9 ± 1.6 μm and 53.5 ± 0.7 μm and the heights of the Ti samples are 66.5 ± 5.2 μm and 83.1 ± 2.6 μm respectively. We observe that the heights of the 8 nm verses the 6 nm Fe catalysts on the Si substrates are relatively similar. While the heights of the CNTs decrease for the 6 nm verses the 8 nm Fe catalyst for the Ti samples.

Next, the t=0 exposure time shows inconsistent growth (**Fig. B.5**) for the Si substrates while the Ti substrates has a consistent yield. The Si substrates with the 6 nm and 8 nm catalyst layers have heights of 5.8 ± 0.3 μm, 9.39 ± 2.1 μm and 83.4 ± 2.7 μm and 58.6 ± 3.4 μm for CVD runs 2 and 5 respectively. The 6 nm and 8 nm catalyst layers for the Ti substrates has heights of 52.4 ± 9.9 μm, 35.6 ± 5.2 μm and 95.8 ± 5.7 μm and 79.1 ± 3.4 μm. Finally, for the t +5 exposure times the Si substrates with the 6 nm and 8 nm catalyst layers have

heights of 62.1 ± 1.8 μm, 44.7 ± 1.4 μm and 67.0 ± 1.4 μm and 42 ± 2.8 μm for CVD runs 3 and 6 respectively. The 6 nm and 8 nm catalyst layers for the Ti substrates has heights of 35.6 ± 12.2 μm, 31.2 ± 2.9 μm and 71.6 ± 4.2 μm and 25.1 ± 2.1 μm.

In conclusion, based on our height measurements and despite the fact that the t =0 exposures had a similar growth rate as the t -5, we determined that the t -5 H_2 exposures, due to its consistent growth profile were best for hydrogen pretreatment. The t +5 samples proved to be inconsistent in growth when we reduce the deposited catalyst layer to 4 nm. The trends of the average CNT heights as a function of H_2 exposure have been determined. Our Si samples for the t =0 exposure time had a large variation of tube heights. It is proposed that factors such as passivation of Fe catalyst on Si substrates (the Ti substrates were also affected though the surface irregularities foster CNT growth) and irregular gas flow rates resulted in the shorten heights of tubes grown during CVD run 2. The Ti samples displayed a consistent trend for tube heights where the t -5 exposure times yielded the tallest nanotubes and the t +5 exposure times yielded the shortest tubes. The surface roughness of the Ti substrate may have facilitated oxidation of the Fe catalyst which would explain the decrease in tube heights of t -5 exposure, which allows for an increased reactant time prior to the introduction C_2H_4 and H_2O vapor gases. Whereas the combination of H_2 and H_2O vapor gases does not improve on the effects oxidation on the catalyst as C_2H_4 is introduced. Simultaneous competing reactions of reduction and nucleation will be occurring during the growth phase.

Figures (**B.4 – B.6**) show that the average heights of the CNTs decreases from position 2 to position 3 for all H_2 exposure times. The heights then increase for both t -5 and t =0, though not t +5 which would suggest that our results are not consistent with the findings of Li *et al.* though this can be attributed to the differences in experimental set-up, such as the diameter of the quartz tube, 2 inches for Li *et al.* and 1 inch for our furnace, flow rates of gases and sample size. A further investigation of these phenomena warrants clarification on the effects of the temperature gradient and gas velocity in the furnace.

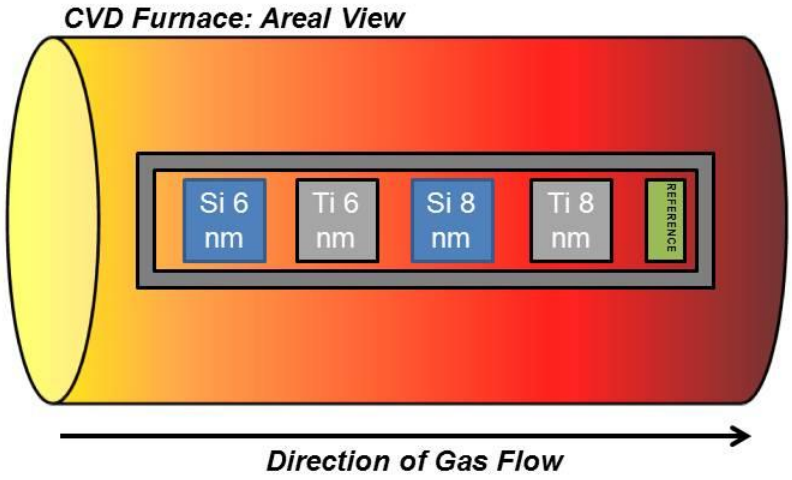

Figure B.1. Image of CVD furnace at zone 2 (center of furnace) and how the samples were mounted with respect to the directional flow of gases (Ar, Ar/H_2O, H_2 and C_2H_4). Three hydrogen exposure times of t -5, t =0 and t +5 were used with the same sample mounting scheme above. The green colored sample is a reference sample present in all growth runs. *Position numbers*: ***1. Si 6 nm 2. Ti 6 nm 3. Si 8 nm and 4. Ti 8 nm***.

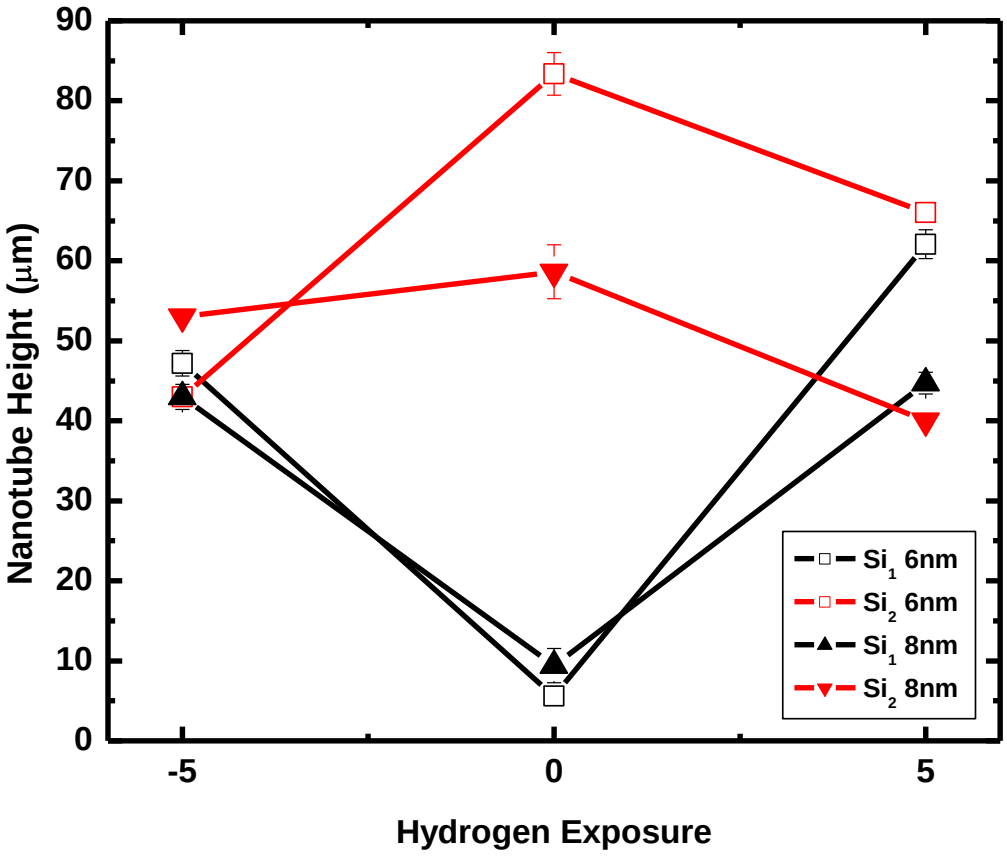

Figure B.2. The effects of hydrogen exposure time on the heights of nanotube for the Si substrate. Substrates with equivalent set numbers (subscript) were grown at the same time in the CVD furnace. In this group of samples the t -5 exposures had consistent growth of CNTs with heights that were virtually equivalent irrespective of catalyst thickness. The t =0 exposure demonstrates the large variation of CNT heights during this growth process. And the t +5 exposures shows both a decrease in the height for set number 2 and a rapid increase in height for set number 1.

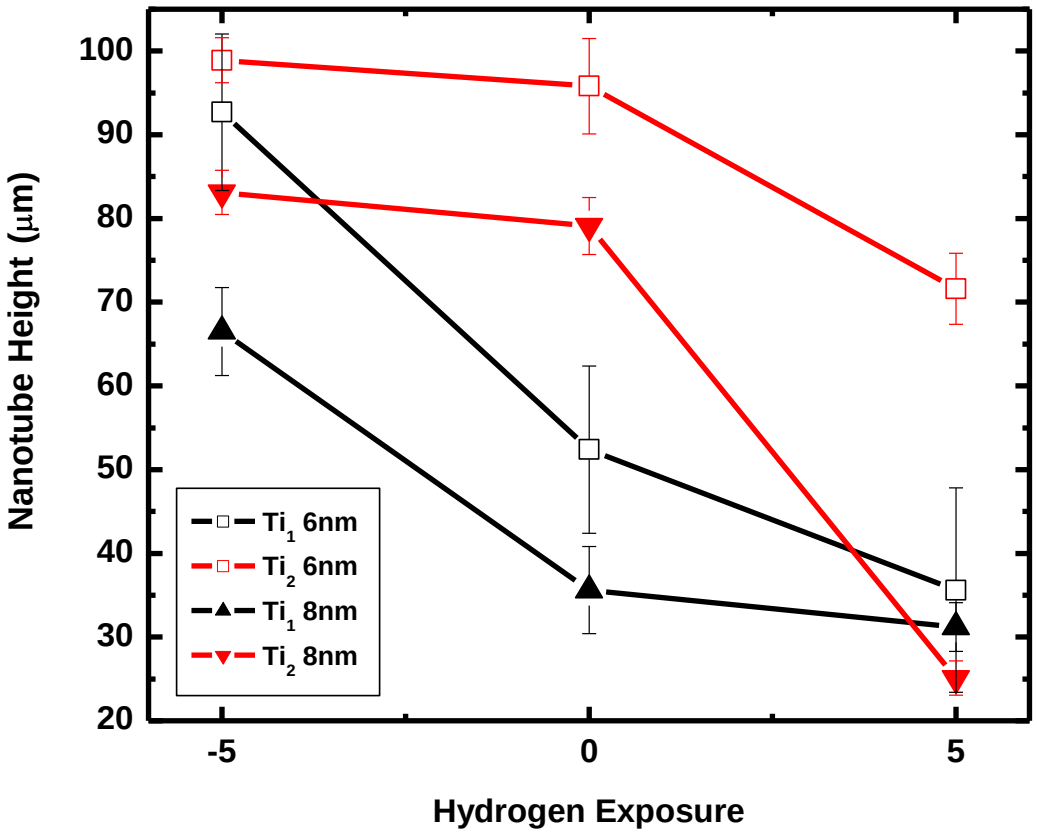

Figure B.3. The effects of hydrogen exposure time on the heights of nanotube for the Ti substrate. Substrates with equivalent set numbers (subscript) were grown at the same time in the CVD furnace. The height of the CNTs on the Ti substrate shows a decrease in height as a function of hydrogen exposure time. The large variation of heights is additionally present for t =0.

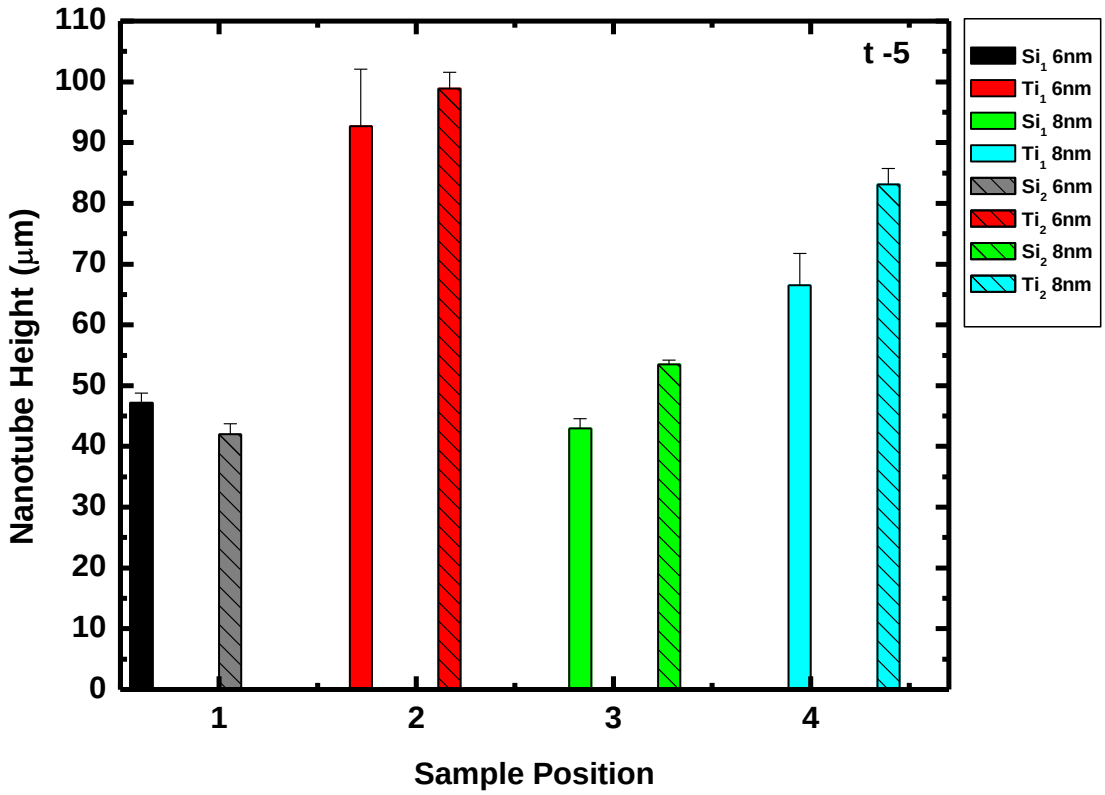

Figure B.4. The average nanotube heights as a function of sample position in CVD furnace for t -5 hydrogen exposure.

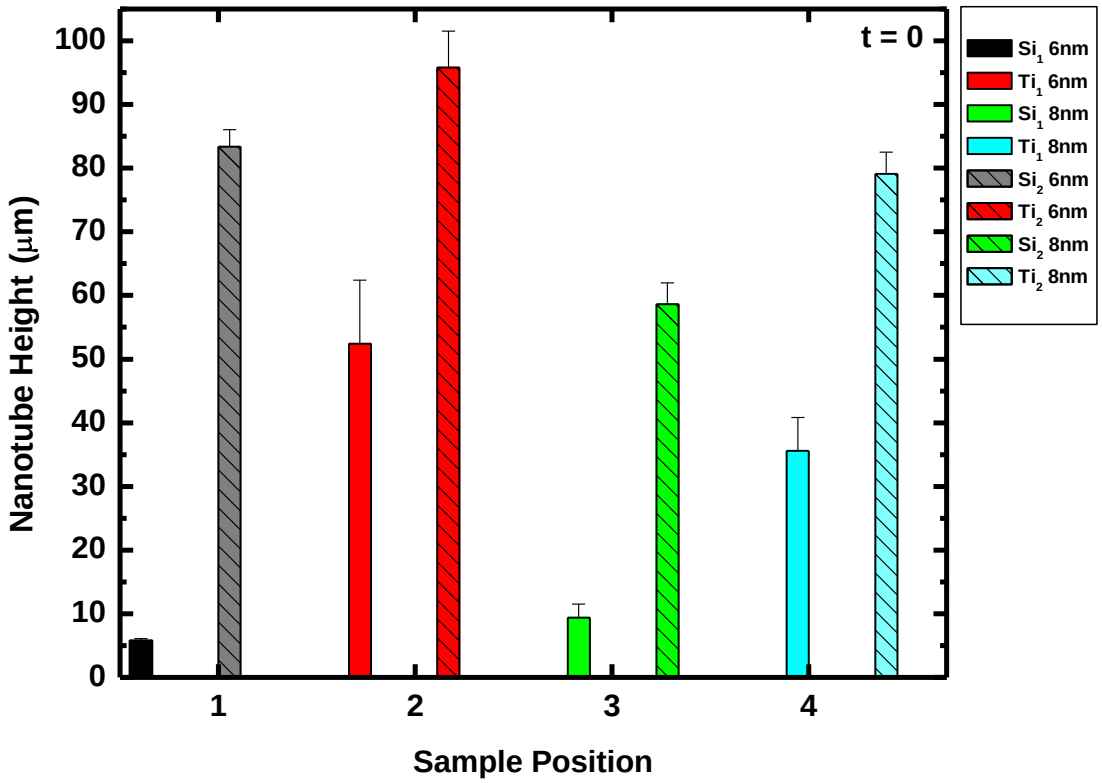

Figure B.5. The average nanotube heights as a function of sample position in CVD furnace for t =0 hydrogen exposure.

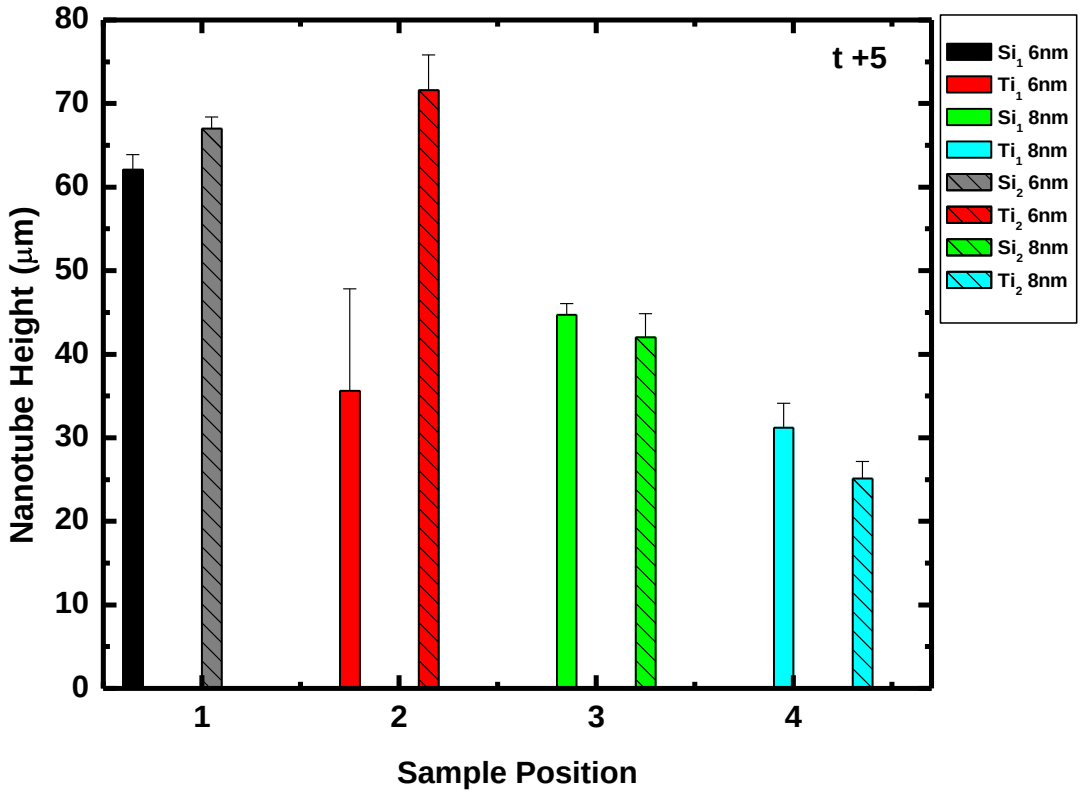

Figure B.6. The average nanotube heights as a function of sample position in CVD furnace for t +5 hydrogen exposure.

Works Cited

1. **Li, G., et al., *The effect of substrate positions in chemical vapor deposition reactor on the growth of carbon nanotube arrays.* Carbon. 48(7): p. 2111-2115.**